Factors Affecting Cation Site Disorder in the $Al_{1-x}Ga_xFeO_3$ System

A thesis submitted to the College of Graduate Studies and Research

in partial fulfillment of the requirements for the Degree of Master of Science

in the Department of Chemistry, University of Saskatchewan, SK

By

JAMES D. S. WALKER

Permission to Use

In presenting this thesis in partial fulfillment of the requirements for a Postgraduate Degree from the University of Saskatchewan, I agree that the Libraries of this University may make it freely available for inspection. I further agree that permission for copying of this thesis in any manner, in whole or in part, for scholarly purposes may be granted by the professor or professors who supervised my thesis work or, in their absence, by the Head of the Department or the Dean of the College in which my thesis work was done. It is understood that any copying or publication or use of this thesis or parts thereof for financial gain shall not be allowed without my written permission. It is also understood that due recognition shall be given to me and to the University of Saskatchewan in any scholarly use which may be made of any material in my thesis.

Requests for permission to copy or to make other uses of materials in this thesis in whole or part should be addressed to:

Head of the Department of Chemistry
University of Saskatchewan
110 Science Place
Saskatoon, SK S7N 5C9

OR

Dean of the College of Graduate Studies and Research
University of Saskatchewan
107 Administration Place
Saskatoon, SK S7N 5A2

Acknowledgements

I would like to acknowledge the University of Saskatchewan for supporting me financially. This project has been funded through a Discovery Grant awarded to Dr. Grosvenor from the Natural Sciences and Engineering Research Council (NSERC) of Canada. The Canadian Foundation for Innovation is thanked for funding the purchase of the PANalytical Empyrean powder X-ray diffractometer used to help characterized the materials in this thesis. The Canadian Light Source is funded by Canadian Foundation for Innovation, NSERC, the National Research Council Canada, the Canadian Institutes of Health Research, the Government of Saskatchewan, Western Economic Diversification Canada, and the University of Saskatchewan. PNC/XSD facilities at the Advanced Photon Source, and research at these facilities, are supported by the US Department of Energy - Basic Energy Sciences, a Major Resources Support grant from NSERC, the University of Washington, the Canadian Light Source, and the Advanced Photon Source. Use of the Advanced Photon Source, an Office of Science User Facility operated for the U.S. Department of Energy (DOE) Office of Science by Argonne National Laboratory, was supported by the U.S. DOE under Contract No. DE-AC02-06CH11357.

Except where noted otherwise, I have carried out the synthesis, characterization, interpretation, and writing presented in this thesis has been carried out by me. Dr. Andrew P. Grosvenor has provided direction and advice over the course of the research presented in Chapters Two and Three, in addition to providing many helpful and beneficial revisions to the written material. I would like to acknowledge the beamline following beamline scientists for their help ensuring my synchrotron experiments were a success: Dr. Lucia Zuin and Ms. Isabelle Gauthier (PGM, 11ID-2, CLS), Dr. Ning Chen (HXMA, 06ID-1, CLS), and Dr. Robert Gordon (PNC/CAT, Sector 20, APS). Additionally, the X-ray absorption spectra in this work were collected with help of Dr. Grosvenor and my fellow group members; J. R. Hayes, M. N. Revoy, and E. R. Aluri. For all of the support I have received in other ways, I would like thank Dr. Grosvenor, my advisory committee, fellow group members (past and present), my friends, and my family.

Abstract

Metal oxide materials are a broad class of materials found in many current technologies due to their interesting properties such as magnetism and ferroelectricity. Material properties can be tuned and heavily influenced by disorder at the atomic level, as has been shown in the ferrimagnetic and ferroelectric $Al_{2-x-y}Ga_xFe_yO_3$ materials, which adopt the non-centrosymmetric, orthorhombic $GaFeO_3$ crystal structure-type (*Pna2₁*). The significant cation disorder and non-centrosymmetric nature of the crystal structure underlie the multiferroic properties in these materials and make them one of the few chemical systems to possess multiferroic ordering near room temperature. Unfortunately, while cation site disorder is responsible for the multiferroic properties observed in these compounds, their complex crystal structure has led to inconsistent reports in the ternary $Al_{2-x}Fe_xO_3$ and $Ga_{2-x}Fe_xO_3$ compounds. X-ray absorption near-edge spectroscopy (XANES) is an element specific technique, which can be used to examine cation site disorder as a function of changes in the average coordination environment around the metal, providing a means of studying these complex materials.

In this thesis, XANES was used to investigate factors affecting cation site disorder in a series of $Al_{1-x}Ga_xFeO_3$ materials ($0 \leq x \leq 1$) adopting the $GaFeO_3$ crystal structure-type. The $GaFeO_3$ crystal structure has four cation sites, of which, the distorted octahedral Fe_1 and Fe_2 sites are primarily occupied by Fe^{3+}, and the less distorted tetrahedral A_1 and octahedral A_2 sites are primarily occupied by Al^{3+} or Ga^{3+}. These materials were initially synthesized using a high temperature ceramic method, and it was found that with increasing Ga^{3+} content (x) these materials show a decrease in the amount of cation site disorder between the tetrahedral site and the three octahedral sites. This decrease is attributed to the tetrahedral site preference of Ga^{3+}, which inhibits cation site disorder at the A_1 site, as opposed to the octahedral site preference

observed for Al^{3+}. Additionally, Fe^{3+} was found to predominantly occupy the three octahedral sites over the tetrahedral site in these materials, likely because of its large ionic size and the strong magnetic coupling between those three sites.

The quaternary $Al_{1-x}Ga_xFeO_3$ materials ($0 \leq x \leq 1$) were synthesized again via two other techniques: a citrate sol-gel method and a co-precipitation method. The oxide network binding the binary metal oxide precursors limits ion mobility in the high temperature ceramic method. The citrate sol-gel and co-precipitation methods were used to generate mixed-metal precursors with a more homogeneous distribution of the metal cations than the binary metal oxide precursors commonly used by the high temperature ceramic method. Mixed-metal precursors reduce the distance the ions have to diffuse, while the nature of the amorphous matrix was found to affect disorder in the resulting material. From analysis of the XANES spectra, the ceramic method showed the least amount of cation site disorder, followed by the citrate sol-gel method and co-precipitation method, respectively. Greater annealing temperatures resulted in an increase in cation site disorder, with the average coordination number of Al^{3+} and Ga^{3+} increasing while the average coordination number of Fe^{3+} decreased. $Al_{1-x}Ga_xFeO_3$ materials synthesized via the co-precipitation method showed the greatest amount of cation disorder, followed by the citrate sol-gel and high temperature ceramic techniques, respectively.

The research presented in this thesis is among the first to examine a large number of materials from the relatively unexplored $Al_{1-x}Ga_xFeO_3$ system, and has contributed to the growing body of knowledge on the factors affecting cation site disorder in these materials and potentially other systems. Further, despite a simple rationale for understanding the features present in Al $L_{2,3}$- and Ga K-edge spectra, these studies have shown how effectively XANES can be used to understand subtle changes in the atomic structure of solid-state materials.

Table of Contents

Chapter Three

Chapter Four

References

Appendix 1

Appendix 2

List of Figures

Chapter One

Chapter Two

Chapter Three

Chapter Three

Appendix 1

Appendix 2

List of Tables

Chapter Two

Appendix 2

List of Symbols and Abbreviations

AFM	Antiferromagnetic
APS	Advanced photon source
c	Speed of light in a vacuum
CLS	Canadian light source
eV	Electron volt
E	Energy of the photon
EXAFS	Extended X-ray absorption fine structure
FLY	Fluorescence yield
FM	Ferromagnetic
h	Plank constant
HXMA	Hard X-ray microanalysis
I_o	Intensity of light incident on the material
I	Intensity of light transmitted through the material
I_F	Fluorescent intensity
j	Spin-orbit coupled angular momentum
l	Orbital angular momentum
λ	Wavelength of photon
μ	Photon absorption coefficient
μ^{-1}	Absorption path length of the photon
MS	Mossbauer Spectroscopy
n	Principle quantum number
ND	Neutron diffraction
s	Spin angular momentum
θ	Incident angle of the photons (fluorescence yield)
VLS-PGM	Variable line spacing plane grating monochromator
x	Path length of the photon
XANES	X-ray absorption near-edge spectroscopy
XAS	X-ray absorption spectroscopy
XRD	X-ray diffraction
Z	Atomic number defining an element

Chapter One

1. Introduction

Metal oxide chemistry is an inorganic sub-discipline of solid state chemistry aiming to relate the synthesis of a material with its elemental composition, atomic structure, and or observable properties.[1,2] Previous studies have found significant cation site disorder in ternary $Al_{2-x}Fe_xO_3$ and $Ga_{2-x}Fe_xO_3$ materials adopting the non-centrosymmetric, orthorhombic $GaFeO_3$ crystal structure-type (*Pna2₁*).[3-5] Intriguingly, this cation disorder is responsible for the observed ferrimagnetic, ferroelectric, and ferrotoroidic properties in these materials.[6-13] While properties of the ternary $Al_{2-x}Fe_xO_3$ ($0.6 \leq x < 2.0$) and $Ga_{2-x}Fe_xO_3$ ($0.7 \leq x < 2.0$) systems have been studied considerably, there are structure-property relationships that merit further study if these materials are to be optimized as multifunctional materials in next generation devices.[5,12,14-16] In contrast to the ternary materials, reports on materials from the quaternary $Al_{2-x-y}Ga_xFe_yO_3$ system are rare. As such, these materials provide a means to expand on the understanding of metal site preference and cation site disorder in the quaternary system, as well as the constituent ternary systems.[6,7,17]

In this thesis, X-ray absorption spectroscopy (XAS) is used to systematically probe how cation disorder can be affected in the quaternary $Al_{1-x}Ga_xFeO_3$ ($0 \leq x \leq 1$) metal oxide system as a function of composition, synthetic technique, and annealing temperature. These materials were found to adopt an isomorphic crystal structure across the full compositional range (x) studied, and can be synthesized by a variety of techniques. As such, these materials offer an excellent means towards systematically studying factors that affect cation site disorder in metal oxides.

1.1. The $GaFeO_3$ Crystal Structure-type

In 1960, a series of $Ga_{2-x}Fe_xO_3$ materials were reported with stoichiometries ranging between x = 0.7 and x = 1.4, and were found to be ferrimagnetic and piezoelectric.[18] The crystal structure was solved five years later, and was found to be a layered structure with a non-centrosymmetric, orthorhombic unit cell (Figure 1.1.a).[3,5,19] In the same time period, $Al_{2-x}Fe_xO_3$ ($0.60 \leq x \leq 1.35$) materials were synthesized and found to possess similar properties to those observed in $Ga_{2-x}Fe_xO_3$ materials as a result of their isomorphic crystal structures.[4,14,20] The $GaFeO_3$ crystal structure-type has four cation sites, and a pseudo-hexagonal ABAC layering of oxygen anions along the *c*-axis (Figure 1.1.b).[3,5,19] The octahedral Fe_1 and Fe_2 cation sites are significantly distorted and primarily occupied by Fe^{3+}, while the tetrahedral A_1 and octahedral A_2 cation sites are mildly distorted and primarily occupied by Al^{3+} or Ga^{3+} (Figure 1.1.c).[3-5,19]

Recent studies have conclusively shown that $AlFeO_3$ and $GaFeO_3$ materials possess multiferroic ordering below their magnetic transition temperature.[7,10,11] Multiferroic materials simultaneously possess two or more types of 'ferroic' ordering (including ferri- and antiferroic ordering): ferromagnetism, ferroelectricity, ferroelasticity, and ferrotoroidism.[21-24] In particular, magnetoelectric multiferroic materials have received attention due to the potential to control the magnetic polarization in a material via an externally applied electric field, and control of the electric polarization in a material via an externally applied magnetic field.[21-26]

While not yet realized, proposed applications for multiferroic materials include electron spin-valves in spintronic devices, optical diodes, 4-state computer memory, optical modulators, and sensor devices.[25-27] Unfortunately, multiferroic ordering is rarely observed in materials since magnetism and ferroelectricity (usually) result from mutually exclusive mechanisms.[21,25] Magnetic ordering arises from long range electron spin ordering of the partially occupied

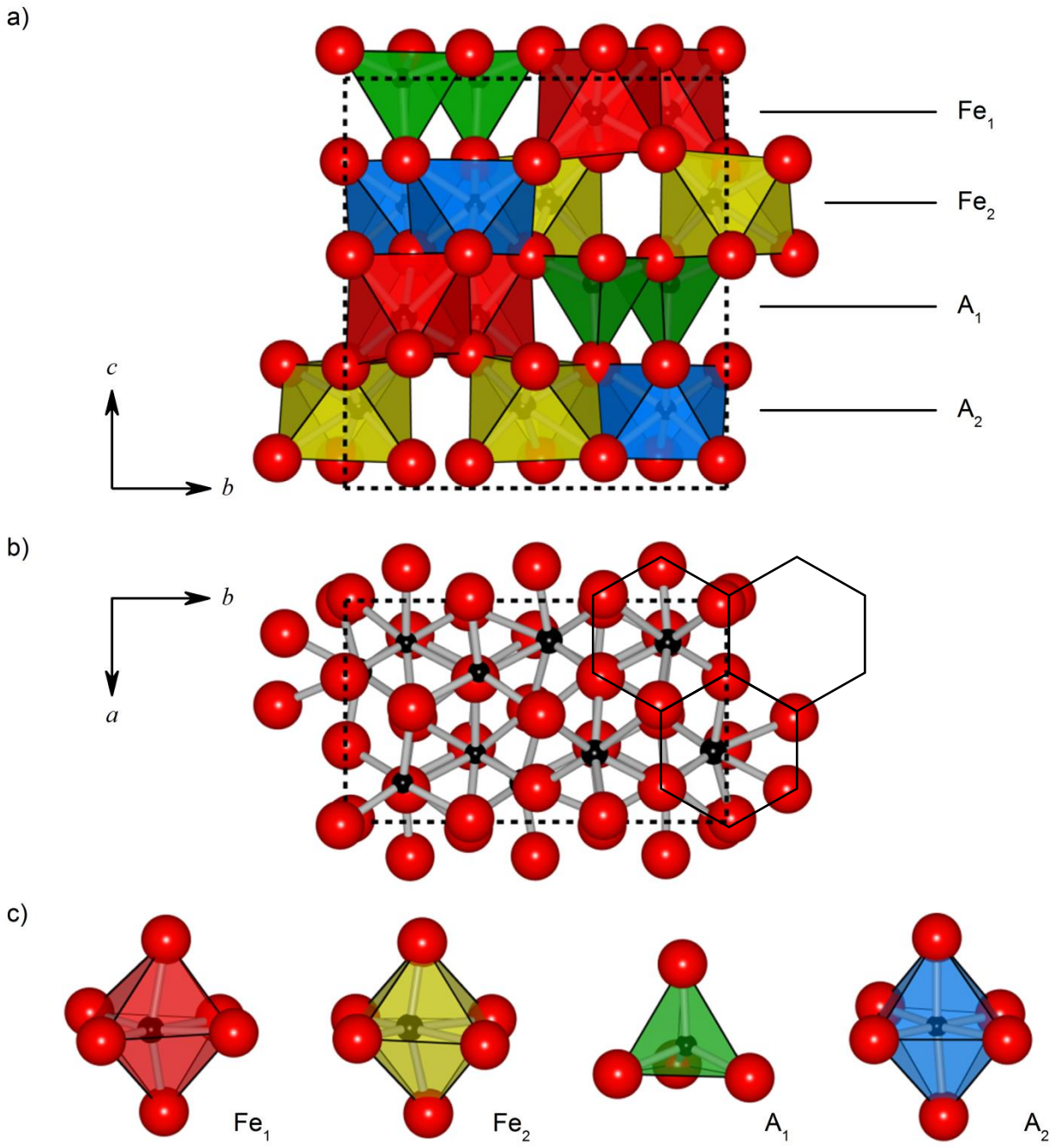

Figure 1.1. The orthorhombic $GaFeO_3$ crystal structure-type (*Pna2₁*): **a)** dashes outline a representation of the unit cell for $GaFeO_3$, and show layers of Fe_1 and A_1 polyhedra alternating with layers of Fe_2 and A_2 polyhedra; **b)** the oxygen anions (red spheres) show pseudo-hexagonal packing down the *c*-axis from the ABAC type layering in this crystal structure; **c)** The four cation sites in the $GaFeO_3$ crystal structure-type, with the distorted octahedral Fe_1 and Fe_2 cation sites primarily occupied by Fe^{3+}, and the less distorted tetrahedral A_1 and octahedral A_2 cation sites primarily occupied by Al^{3+} or Ga^{3+}.

electronic states.[21,25] In contrast, ferroelectricity generally requires unoccupied states to stabilize the periodic, off-centre displacements of the ions that polarize the material.[21,25]

Computational studies have predicted that $GaFeO_3$ and $AlFeO_3$ should display antiferromagnetic ordering in the absence of cation site disorder.[7,8,28,29] The unpaired electrons in the Fe^{3+} 3d-states spin align parallel to the *a*-axis, ferromagnetically couple in the *ab*-plane, and stack antiferromagnetically along the *c*-axis. The ferrimagnetic ordering in the $Al_{2-x}Fe_xO_3$ and $Ga_{2-x}Fe_xO_3$ systems results from strong antiferromagnetic super-exchange interactions that occur between the Fe^{3+} present at the Fe_1 sites, and Fe^{3+} present at the Fe_2 and A_2 sites (Figure 1.2.).[4-8,11,12,30] The small size of the tetrahedral A_1 site appears to significantly limit its occupation by Fe^{3+} relative to the three octahedral sites. As a result, the magnetic moment from Fe^{3+} present at the Fe_2 and A_2 sites cannot be fully compensated by the smaller amount of Fe^{3+} present at the Fe_1 and A_1 sites and a ferrimagnetic moment is observed along the *c*-axis.[6,7,11,15,16,29-32] While the magnetic relationships in this material have been elucidated,

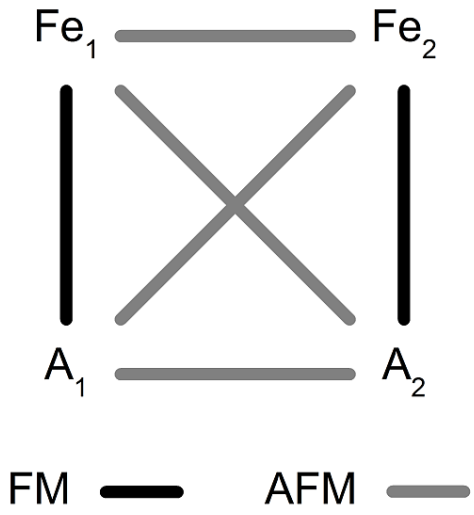

Figure 1.2. Ferromagnetic (FM) and antiferromagnetic (AFM) interactions between Fe^{3+} present at the four, non-equivalent cation sites in the $GaFeO_3$ crystal structure-type.

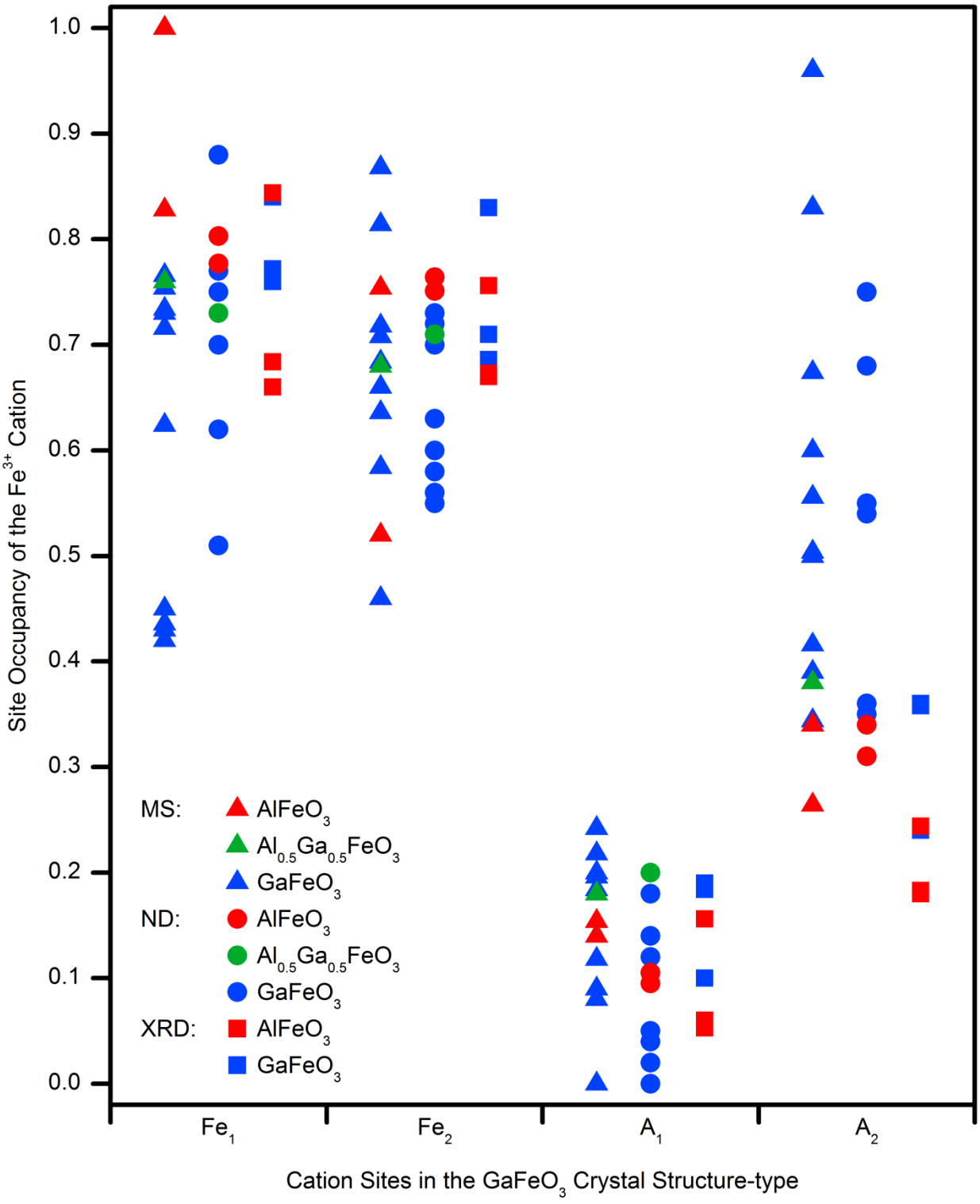

Figure 1.3. Fe^{3+} cation site occupancies reported for $AFeO_3$ materials (A = Al^{3+}, Ga^{3+}) determined by ^{57}Fe Mössbauer spectroscopy (MS), neutron diffraction (ND), or X-ray diffraction (XRD), compiled from references 4-6, 14, 31, and 33-41.

there are still significant discrepancies in the Fe^{3+} site occupancies reported for the ternary $Al_{2-x}Fe_xO_3$ and $Ga_{2-x}Fe_xO_3$ materials (Figure 1.3.).[4-6,14,31,33-41] Although the Fe^{3+} occupancies are found within distinct ranges for each of the cation sites, the significant variability in the reported values has limited the ability to compare and rationalize the experimentally observed properties in these materials.

Ferroelectricity has been observed in the thin-films of these materials, while the bulk material is piezoelectric.[7,10,18,42] The electronic polarization observed in these materials is suggested to be from the large anisotropic displacements of the Fe^{3+} cations, as large as 0.26 Å, resulting in significant distortion of the polyhedral oxygen cage.[7,9,12] While magnetic transition temperatures have been for $AlFeO_3$ or $GaFeO_3$ materials reported numerous times, no ferroelectric transition temperature has been observed or reported to date, even at high temperature.[40] That said, much of the research on these materials has solely focused on their magnetic properties, possibly explaining why the non-magnetic isomorphs (i.e., κ-Al_2O_3 and κ-Ga_2O_3) have received less attention than the metastable, high temperature multiferroic ε-Fe_2O_3 phase.[43-48]

1.2. Synthesis of Metal Oxide Materials

The $Al_{1-x}Ga_xFeO_3$ materials presented in this thesis were synthesized via high temperature ceramic, citrate sol-gel, and co-precipitation methods, which are among the most commonly techniques used in solid state materials synthesis.[49-51] That said, different synthetic techniques do not necessarily produce identical materials, as was found during the comparison of the $Al_{1-x}Ga_xFeO_3$ materials presented in Chapter Three. Given the relevance of these synthetic techniques to the results presented in this thesis, these three techniques will be reviewed briefly before discussing synthetic aspects specific to $Al_{1-x}Ga_xFeO_3$ and related oxide materials.

1.2.1. *The High Temperature Ceramic Method*

The high temperature ceramic method is one of the most commonly used routes for synthesizing metal oxide materials as a result of its simple methodology and generally cheap precursors.[50] The high temperatures used by this method generally favour thermodynamically stable crystal phases and often produce dense, highly crystalline materials.[50,51] This technique involves mixing and heating binary metal oxides to high temperatures where significant diffusion of the metal ions can occur in the solid state.[51] Unfortunately, long ion diffusion paths through crystal grains can result in very slow formation of the final material.[50] This can be mitigated by grinding the precursors into a fine homogeneous powder and mechanically pressing it into a dense pellet; this reduces ion diffusion path lengths, and thereby reduces the time required to obtain a well crystallized final product. Additionally, certain materials like wüstite (Fe_xO; $0.88 \leq x \leq 0.95$) are only stable at high temperatures, but can be stabilized at room temperature by forming the material at high temperature, and rapidly cooling the material in air to quench the solid state reaction.[52] The rapid temperature drop immobilizes the ions, preventing structural rearrangement to a more stable crystal structure or decomposition into a mixture of crystal phases.[52]

1.2.2. *The Citrate Sol-Gel Method*

The citrate sol-gel method, sometimes referred to as the Pechini method, is often used to synthesize ceramics at much lower temperatures than can be obtained by the ceramic method.[49,50,53] In this method, metal nitrates and chlorides are dissociated into an aqueous solution with a polyprotic acid and polyalcohol, such as citric acid and ethylene glycol.[49,50,53] The citrate anion chelates the metals, and via condensation reactions with the ethylene glycol, forms an ester-linked polymer network.[53] Removal of the solvent through gentle heating results in an

amorphous metal citrate precursor, in which the different metal ions are uniformly distributed throughout the polymer network.[49,53] The precursor is then heated to decompose and burn off the organic matter to form the desired metal oxide.[49,50,53] The mixing in solution results in short ion diffusion lengths to form the final crystal structure; allowing the material to form faster, and at lower temperatures, than materials synthesized via the ceramic method.[49,50,53] In addition, these methods can allow for the synthesis of thermodynamically metastable phases, such as ε-Fe_2O_3, which cannot be obtained directly via the ceramic method (as a single phase product).[48]

1.2.3. *The Co-precipitation Method*

Similar to the citrate sol-gel method, the co-precipitation method initially mixes the metal cations in solution.[50,53] Following this, additional reagents are added to significantly reduce the solubility of the metal ions (e.g., altering the pH of the solution), leading to the precipitation of an amorphous mixture of metal cations and counter anions.[50,51] This mixture is then filtered, washed, and dried before thermally decomposing the precipitate to remove the organic matter and form the metal oxide.[50,51,53] Thus, like the citrate sol-gel technique, the co-precipitation method provides superior mixing of the metal ions over the ceramic method. That said, the ceramic method can result in materials with higher purity than solution-based methods since the precursors do not contain organic matter that must be removed.[50,53]

1.2.4. *Synthetic Aspects of $Al_{1-x}Ga_xFeO_3$ and Related Materials*

Half a century ago, it was noted that the final annealing temperature during synthesis can significantly impact the magnetic transition temperature observed in $GaFeO_3$.[54] Since then, it has been shown that the synthetic method can significantly affect the magnetic transition temperature observed in $GaFeO_3$ and related materials, as shown in Figure 1.4.[4-7,10,14,17,18,31-35,37,39,41,42,54-63]

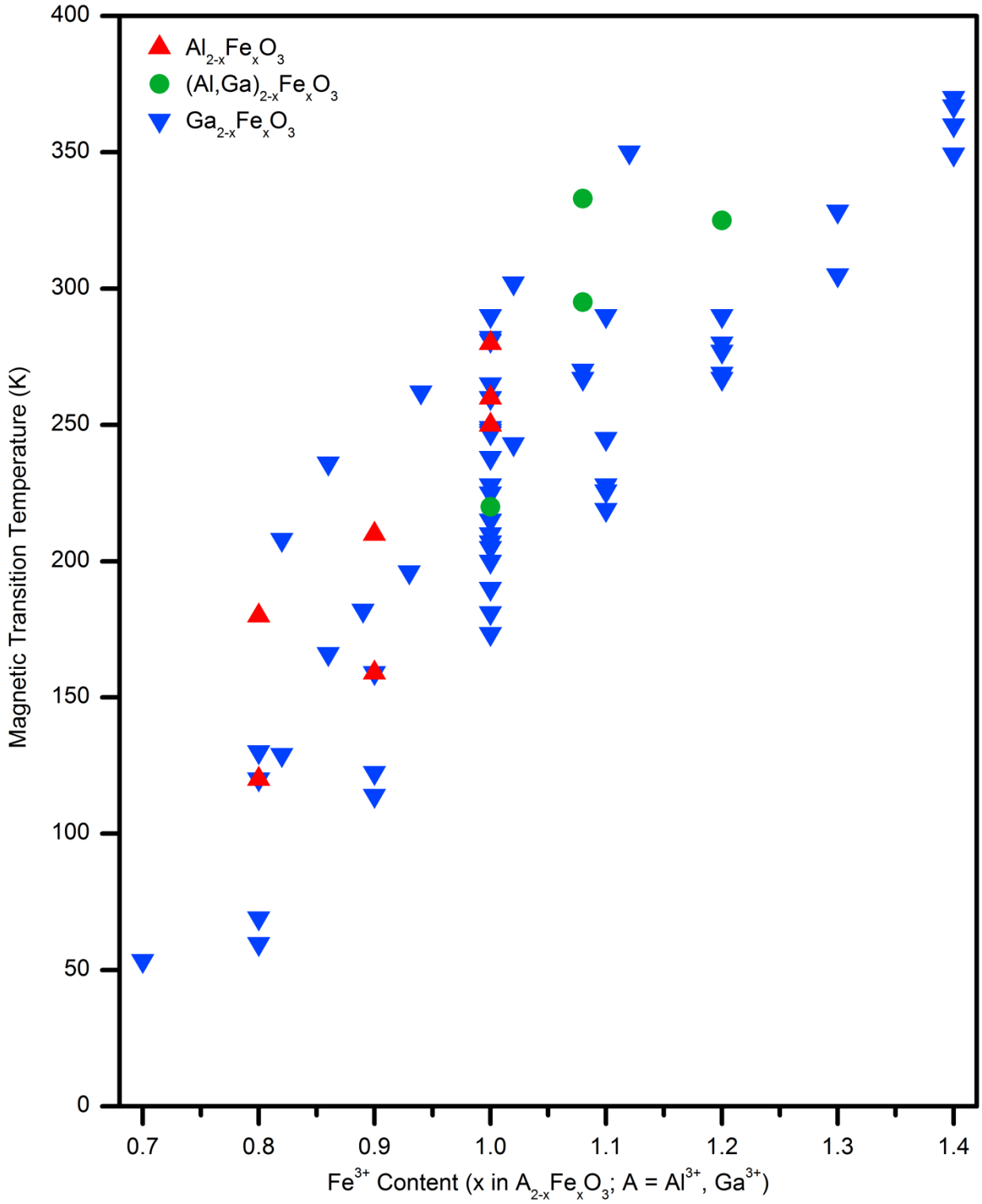

Figure 1.4. Magnetic transition temperatures reported for the ternary $Al_{2-x}Fe_xO_3$ and $Ga_{2-x}Fe_xO_3$ materials, and the quaternary $(Al,Ga)_{2-x}Fe_xO_3$ materials, compiled from references 4-7, 10, 14, 17, 18, 31-35, 37, 39, 41, 42, and 54-63.

Interestingly, while different synthetic effects are often noted in studies on the $Al_{2-x}Fe_xO_3$ and $Ga_{2-x}Fe_xO_3$ systems, there are relatively few reports that directly compare synthetic techniques or the effect of annealing temperature during synthesis.[6,31,33,35,36,40,64] While $Ga_{2-x}Fe_xO_3$ materials have been synthesized by a number of high and low temperature techniques, most $Al_{2-x}Fe_xO_3$ materials have only been synthesized in pure form by heating the precursors in a narrow temperature range between 1320 ºC and 1410 ºC.[14,20,64-66] Exceptions to this involve relatively new techniques that have been developed to encapsulate and stabilize the isomorphic ε-Fe_2O_3 phase inside SiO_2 nanoparticles.[67,68] Using these techniques to substitute Al^{3+}, these studies were able to synthesize ε-$Fe_{2-x}Al_xO_3$ materials ($x \leq 0.75$) without impurity phases at temperatures between 1025 ºC and 1100 ºC.[15,69,70] During synthesis of the $Al_{1-x}Ga_xFeO_3$ materials in this thesis, it was noticed that substitution of Ga^{3+} for Al^{3+} lowered the annealing temperature required to crystallize the materials without impurity phases being present. This was partially expected given that $GaFeO_3$ has been successfully synthesized using temperatures as low as 500 ºC.[71]

In addition to substitution with Al^{3+}, there has been some success creating other isomorphic quaternary metal oxides via substituted $GaFeO_3$ materials. Examples of this include incorporation of N^{3-} or S^{2-} via a tartrate sol-gel method, substitution of Cr^{3+} or Mn^{3+} via a ceramic and/or citrate sol-gel method, and Mg^{2+} doping in vapor deposited thin films.[6,7,10,35,62,72-79] In comparison, there do not appear to be any reports of substituting additional ions into the $Al_{2-x}Fe_xO_3$ system (with the exception of Ga^{3+}).[6,7,54,72] This is likely a result of the stricter synthetic conditions required to obtain single phase $Al_{2-x}Fe_xO_3$ materials in comparison to $Ga_{2-x}Fe_xO_3$ materials.[64] This could change in the near future due to the recent advances in synthetic routes used to obtain the metastable ε-Fe_2O_3 phase, which to date has been used to

substitute Fe^{3+} for Al^{3+}, Ga^{3+}, Rh^{3+}, and In^{3+}.[15,16,69,70,80,81] These studies, as well as the studies presented in Chapters Two and Three of this thesis, help to examine the competing factors underlying how composition, synthetic method, or annealing temperature can affect cation site disorder in these metal oxide systems.

1.3. X-ray Absorption Spectroscopy

1.3.1. *Synchrotron Radiation and Spectroscopy*

X-ray absorption spectroscopy (XAS) is a broad term for techniques that use X-ray photons to excite electrons out of locally bound states.[82-86] In this thesis, X-ray absorption near-edge spectroscopy (XANES), a form of XAS, was used to probe the physical and electronic environments of the constituent elements in a material (e.g., coordination number, oxidation state).[82-86] Due to the difficulty of producing high energy X-rays in a normal laboratory setting, XAS techniques often require the use of a synchrotron facility, such as the Canadian Light Source (CLS) in Saskatoon, SK. Synchrotron facilities allow access to an extensive range of spectroscopic techniques because they can produce light across a large portion of the electromagnetic spectrum; from far-infrared light (λ < 15 μm; E < 80 meV) to hard X-rays (λ < 30 pm; E > 40 keV).[85,87] Unlike light in the visible and ultra-violet spectrum, X-rays are generally described using electron volts (eV) instead of wavelength, which is the energy gained or lost by an electron moving through a one volt potential.[87] Conversion between the two units can be performed using Equation 1.1., where E is the energy of the photon, *h* is the Planck constant, *c* is the speed of light in a vacuum, and λ is the wavelength of light in nanometers.

$$\mathrm{E\ (eV)} = \frac{hc}{\lambda} = \frac{1239.84\ \mathrm{eV \cdot nm}}{\lambda\ \mathrm{(nm)}} \qquad \textbf{(1.1.)}$$

Synchrotron light sources become particularly advantageous when considering the incredibly high intensity light they can produce relative to laboratory-based sources.[83,88,89] Modern synchrotrons can generate light that is 10^3 brighter than infrared sources, and up to 10^{12} brighter than conventional laboratory X-ray sources (brightness is measured in photons/s/mm^2/mrad^2/0.1% bandwidth).[83,88,89]

Synchrotron facilities create light using free electrons (i.e., electrons are not bound to an atom) travelling near the speed of light.[83,88] These electrons are generated in a multiple step process, which will be outlined briefly. First, an electron gun attached to a linear particle accelerator is used to generate the electrons under ultra-high vacuum, bunch them together, and accelerate them to a higher velocity.[90] Following this, the electrons are injected into a closed loop called a booster ring, which uses magnets to direct the beam around the corners of the ring while radiofrequency cavities are used to accelerate the electrons up to 99.999998% of the speed of light (for the CLS).[90] The electrons are then injected into a larger storage ring to generate light for experiments. The electrons generate light each time they are accelerated, such as when magnets are used to bend the electron beam around the storage ring.[83,87] An even greater amount of photon flux can be generated by insertion devices placed in straight sections between the bending magnets.[88] These devices generate light from bending the electron beam multiple times using an anti-parallel array of magnets.[87] The broad-band synchrotron radiation can be filtered by beamline optics to obtain a beam of photons with a bandwidth on the order of 0.01% of the desired photon energy (i.e., $\Delta E/E \sim 10^{-4}$; $\Delta E_{@10keV} = 1$ eV).[83,84] The monochromatic photon beam is then directed into a beamline end station where it can be utilized in experiments.[83,84]

While access to tunable, high intensity light sources allows for a large range of experimental techniques to be utilized, X-ray absorption techniques are highly desirable for their

ability to probe individual elements in a material.[82-86] This has been taken advantage of in numerous types of research conducted not only by chemists, but by a large multidisciplinary research community spanning much of the natural and applied sciences.[87] Examples of this include *in situ* monitoring of homogeneous catalysts, chemical speciation in complex soil matrices, and characterization of the atomic and electronic structure in amorphous materials.[91-93] The remainder of this section will discuss aspects of the physics underlying the XANES technique, while Section 1.4. will describe the two experimental setups used to collect the XANES data presented in this thesis.

1.3.2. *X-ray Absorption Near-edge Spectroscopy (XANES)*

While materials are generally quite transparent to X-rays, significant absorption can be observed when certain conditions are met.[83-86] In the absorption process, the incident photon is annihilated as it transfers energy to excite an electron out of an occupied state, leaving an unoccupied core-hole state.[86] This photo-excited electron can then move into a higher energy bound state on the absorbing atom (or on a neighboring atom); continuum states in the conduction band of the material; or the electron can be ejected from the material entirely.[84,85] When these processes occur, a sharp increase in the absorption of light by the material is often observed, which is referred to as an absorption edge (Figure 1.5.).[83-86] The features present just above and below the absorption edge comprise the near-edge or XANES region, while the oscillating features continuing to higher energies above the absorption edge define the extended X-ray absorption fine structure (EXAFS) region.[84,94]

Unlike the XANES region, which is primarily due to excitation of electrons into bound states or continuum states, the features in the higher energy EXAFS region are a result of the wave nature of ejected photoelectrons scattering from nearby atoms in the material.[84,94] When the

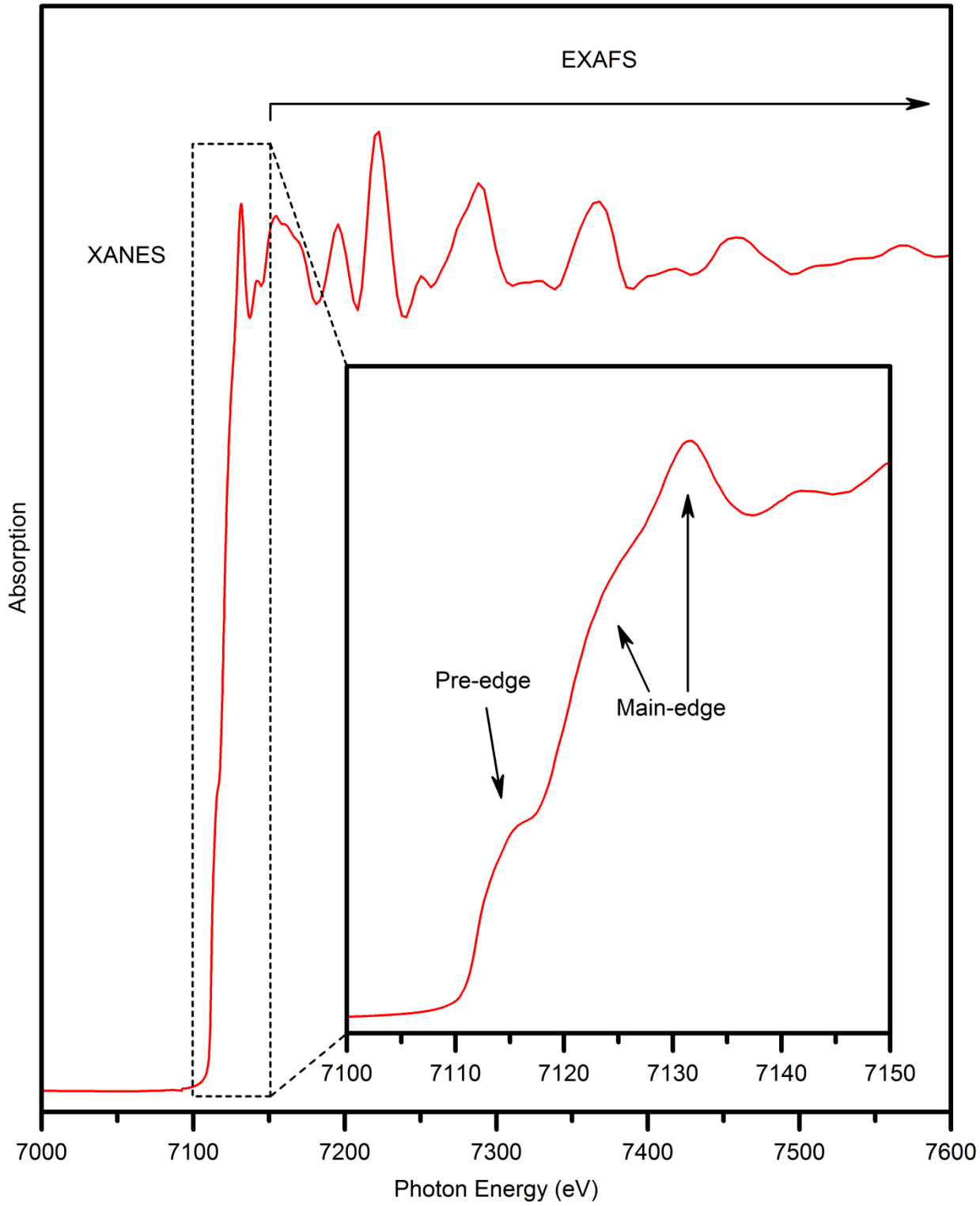

Figure 1.5. X-ray absorption spectrum from α-Fe metal showing the XANES and EXAFS regions. The inset shows an enhanced view of the pre-edge and main-edge regions in the XANES portion of the spectrum.

ejected photoelectron wave scatters back on itself, the backscattered photoelectron wave can be in-phase or out-of-phase with the outgoing photoelectron wave.[84,94] Thus, the positions of the oscillations are dependent on the path length of the scattered photoelectron, while the amplitude of the oscillations is dependent on the number of atoms in each coordination sphere and their respective atomic scattering factors.[84,94] Using appropriate software, the oscillations in the EXAFS region can be fit to a structure model. Refinement of this model can allow determination of interatomic distances, as well as the number and type of the atoms present in the coordination shells around the absorber.[82] While this can be a very powerful technique, only the XANES region of the spectra presented in this thesis is utilized, and further theory related to the EXAFS technique will not be discussed.

The notation used to label X-ray absorption edges depends on the shell that the electron is being excited from, with K-, L-, and M-edges referring to excitation of electrons from states with a principle quantum number of n = 1, n = 2, and n = 3, respectively.[82-86,94] From the law of momentum conservation, different electronic states can be probed separately because of the requirement to conserve the angular momentum that is imparted onto the electron when the photon is absorbed (Figure 1.6.).[82-86,94] As photons are particles with one unit of angular momenta, transitions are only formally dipole-allowed when the total difference in the angular momentum l between the initial state and the final state is equal to one (i.e., $\Delta l = \pm 1$).[82-86,94] Using electronic states from Al^{3+} as an example, the dipolar 2p → 3s transition (Al L-edge; $\Delta l = -1$) would be formally dipole-allowed, while the non-polar 1s → 3s transition (Al K-edge; $\Delta l = 0$) or the quadrupolar 1s → 3d (Al K-edge; $\Delta l = \pm 2$) transition would be formally dipole-forbidden. That said, quadrupolar-like transitions are weakly allowed in certain circumstances.[86,95-97]

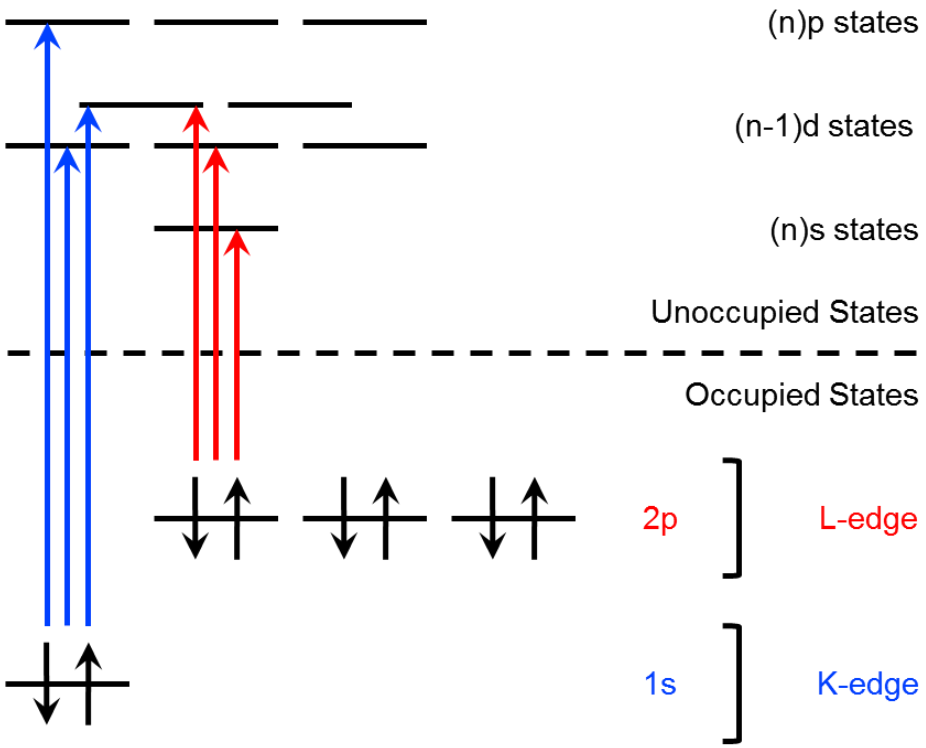

Figure 1.6. X-ray transitions commonly observed in the vicinity of metal K-edges include the formally forbidden 1s → (n-1)d transitions, and the dipole allowed 1s → (n)p transitions. The X-ray transitions commonly observed in the vicinity of metal L-edges include the dipole allowed 2p → (n)s and 2p → (n-1)d transitions.

The first case, in which a quadrupolar transition is allowed, can occur from mixing the p- and d-states of the absorbing atom, results in the presence of states with p-type symmetry in the d-band of the material.[86,95-97] For example, a first row transition metal occupying a tetrahedral cation site lacks inversion symmetry, which leads to strong mixing of the local 3d- and 4p-states.[86,96,97] In the second case, when the absorbing atom does possess an inversion centre, orthogonality of the local 3d- and 4p-orbitals prohibits mixing of local states.[86,96,97] That said, non-local excitations can occur from hybridization of local 4p-states with non-local 3d-states (via the O 2p-states), which introduces accessible states with p-symmetry into the d-band of the

next-nearest-neighbour atom.[86] In the third case, local quadrupolar 1s → 3d transitions can occur in centrosymmetric atoms (outside of dipolar selection rules), although these transitions are often orders of multiple orders of magnitude lower in intensity.[86]

Following photo-excitation, the spin angular momentum of remaining unpaired electron (not the excited electron) can align with or against its intrinsic orbital angular momentum, leading to different final state configurations.[86,96,97] For example, the p-states in the L-shell will split into a higher energy state ($2p_{1/2}$) and lower energy state ($2p_{3/2}$) in which the subscript represents the total angular momentum (i.e., $j = |l \pm s|$).[86,96,97] As the strength of the spin-orbit coupling increases with increasing atomic number, this can lead to discrete absorption edges, which are then labeled with a subscript denoting the relative order of the transitions from highest energy to lowest energy. For example, the L_1-edge (2s → (n)p) is always greater in energy than the L_2-edge ($2p_{1/2}$ → (n)s or (n-1)d), which is always greater in energy than the L_3-edge ($2p_{3/2}$ → (n)s or (n-1)d).[84,98] The spherical symmetry of s-states precludes them from spin-orbit coupling in the final state, and thus, no splitting is observed in the K-, L_1-, or M_1-edges.[86,96,97] Choosing the appropriate energy for the desired transition and element of interest, these selection rules can be used to selectively probe the unoccupied density of electronic states for the constituent elements in a material.[85,94] Assuming there is sufficient energy for excitation, the probability for the transition to occur is proportional to the number of unoccupied final states.[85,94] Thus, measuring the absorption of X-rays by a given element provides a measure of the partial density of unoccupied states in a material.[84]

While the origins of the XANES transitions have been presented, the energy dependence of the transitions has not been discussed. Electronic transitions probe the *difference in energy* between two electronic states, with the energy dependence of the transition being a combination

of ground and final state effects. Some factors influencing the energy of the electronic states before excitation occurs are intuitive due to their physical nature, such as the identity and oxidation state(s) of the constituent elements in the material.[83,86,99] This can be seen for a series of Fe-containing materials, where the increasing oxidation state shifts the features in the absorption spectrum to higher energy (Figure 1.7.). With increasing oxidation state, the increased attractive potential from the nucleus lowers the energy of the electronic states around the absorber atom.[82,83,85,99] Relative to the unoccupied conduction state, the binding energy of the core-electron is affected more by oxidation state because of its closer proximity to the nucleus.[82,83,85,99] Following excitation, the presence of the core-hole affects the energy of the final state through spin-orbit coupling and other effects.[83,94,95,99] These effects are still related to the effective nuclear charge, but they are dynamic in nature since they occur during the excitation of the electron.[83,94,95,99,100] In the time it takes for the electron to transition between the initial state to the final state (e.g, $< 5 \times 10^{-13}$ s for the 1s → 4p transition at the Fe K-edge), all of the electronic states around the absorber atom will begin to relax to lower energy from the increased nuclear potential experienced caused by the presence of the core-hole state.[101,102] Thus, any electronic or physical effects which alter the Coulombic screening of the core-hole state will affect the extent of final state relaxation.[83,94,95,99,100]

The binding energies of core level electrons are specific to the element being probed, which is in large part due to differences in the nuclear charge of each element.[84,85] For example, comparing two adjacent elements like Al and Si, an 80 eV photon can excite an electron occupying the 2p-state of Al, but lacks the energy required to excite an electron occupying the 2p-state of Si.[99] In addition, the binding energy is also modulated by the effective nuclear charge experienced by the electrons on the absorbing atom due to factors such as

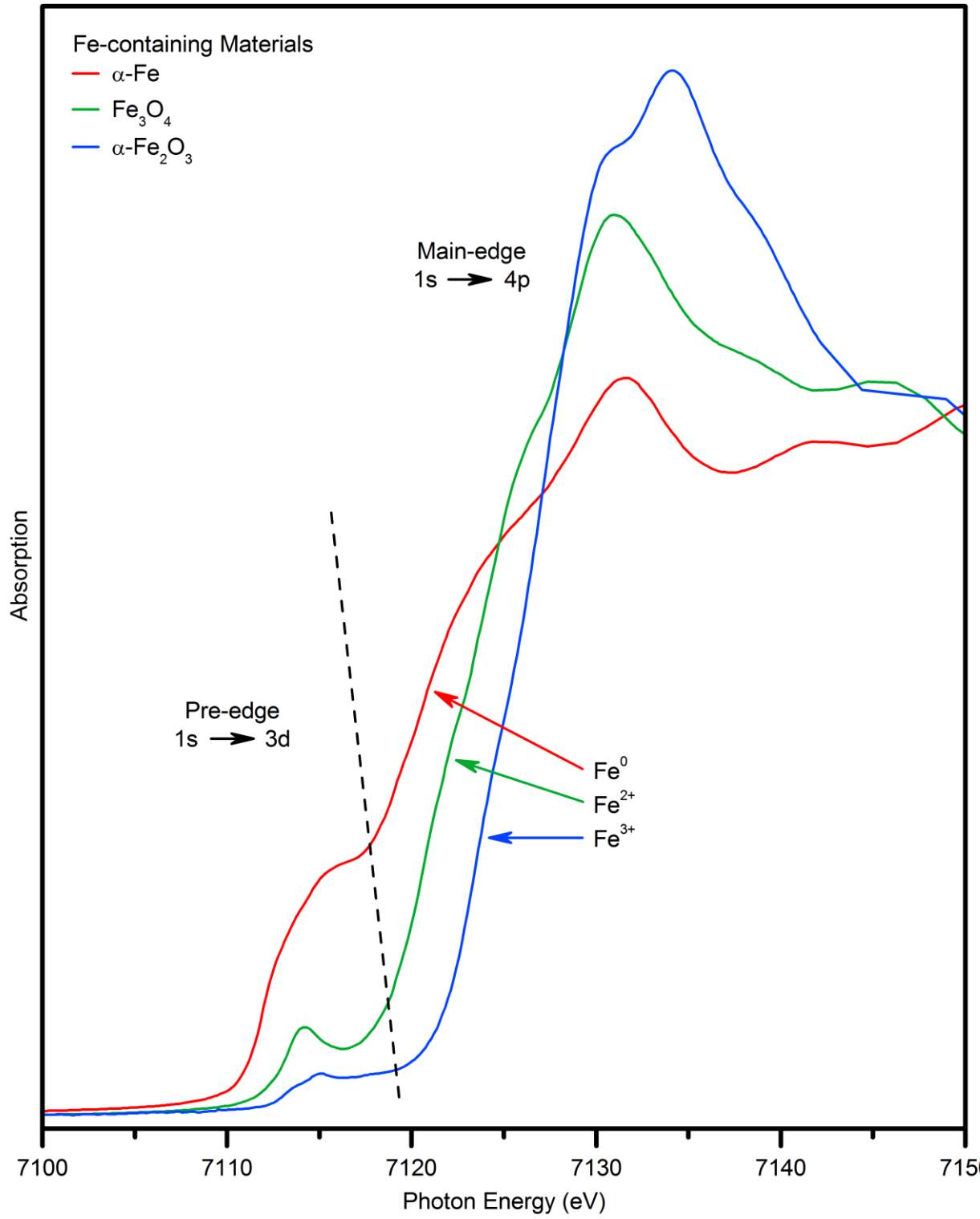

Figure 1.7. Fe K-edge XANES spectra from materials containing Fe in different oxidation states; the onset of the absorption edge increases in energy as the oxidation state of Fe increases. The dashed line separates the pre-edge and main-edge features.

oxidation state, number of atoms in surrounding coordination shells, and the electronegativities of those atoms.[83,94,95,99,100] Unfortunately, these effects are complex and computer modelling of the features present in a XANES spectrum is non-trivial.[84] As a result, this technique relies heavily on a qualitative 'finger-print' method, in which spectra from materials with well characterized structures are used to relate and assign features to the atomic structure of the chemical species present in the material.[82,83,85,103-106] Despite being a qualitative technique, XANES has distinct advantages over other potentially quantitative characterization techniques like X-ray or neutron diffraction, Mössbauer spectroscopy, or EXAFS. In particular, materials with multiple chemical species or complex elemental compositions can be analyzed because the interpretation of XANES spectra is not based on attempting to model the experimental data.

1.4. Experimental Setups for the Collection of XANES Spectra

In a XANES experiment, the absorption coefficient (μ) from a material is measured as a function of the incident photon energy.[82-85,94] The absorption coefficient is a measure of the total photoabsorption cross-section for the material; this can be thought of as how strongly the photons interact with the material. For a monochromatic beam of photons, the inverse of the absorption coefficient (μ^{-1}) is equal to the average distance a photon will travel before being absorbed by a given material.[82-85,94] This quantity is often referred to as the mean inelastic scattering path of the photon, or the absorption path length of the photon. Since the absorption path length changes significantly with photon energy, two experimental setups were required to collect the XANES spectra presented in this thesis. Section 1.4.1. describes a transmission setup for photon energies in the hard X-ray region (i.e., 4 keV < E_{photon} < 30 keV), while Section 1.4.2. describes an ultra-high vacuum setup for photon energies in the extreme ultraviolet and soft X-ray regions (i.e., 10 eV < E_{photon} < 4 keV).

1.4.1. *Hard X-ray Transmission Experiments*

Transmission of light through a material can be described via the Beer-Lambert law. When passing a monochromatic beam of light through a material with a uniform thickness (x), the number of photons incident on the material (I_o) will be reduced to the number of photons transmitted (I; Equation 1.2.).[82-85,94]

$$I = I_o e^{-\mu x} \quad \textbf{(1.2.)}$$

Photoabsorption (μx) by a material is negative and logarithmic with respect to transmittance $\left(\frac{I}{I_o}\right)$, and is linearly proportional to the absorption path length of the material (Equation 1.3.).[82-85,94]

$$\mu x = -\ln\left(\frac{I}{I_o}\right) \quad \textbf{(1.3.)}$$

The linear relationship between absorption and material thickness will be maintained so long as the material in the beam path is uniform, and thin enough to transmit sufficient photon flux through the material for measurement.[84,85] In addition, this linear nature allows the background absorption from different materials to be scaled with respect to each other, resulting in spectra that represent the portion of the absorption coefficient solely from the element of interest for a given material.[84,85] As well, materials with different elemental compositions or concentrations can be compared.[84,85] A typical experimental setup for collection of hard X-ray XANES data is shown in Figure 1.8.[107] The photon flux is measured indirectly as an electrical current inside detectors called gas ionization chambers.[82,84,85] When the photon beam passes through the gas in the detector, a small portion of the gas is ionized via the photoelectric effect.[82,84,85] The photoelectrons ejected from the ionized gas molecules are then collected on charged (capacitive) plates and measured as an electrical current proportional to the photon flux.[82,84,85] The first and

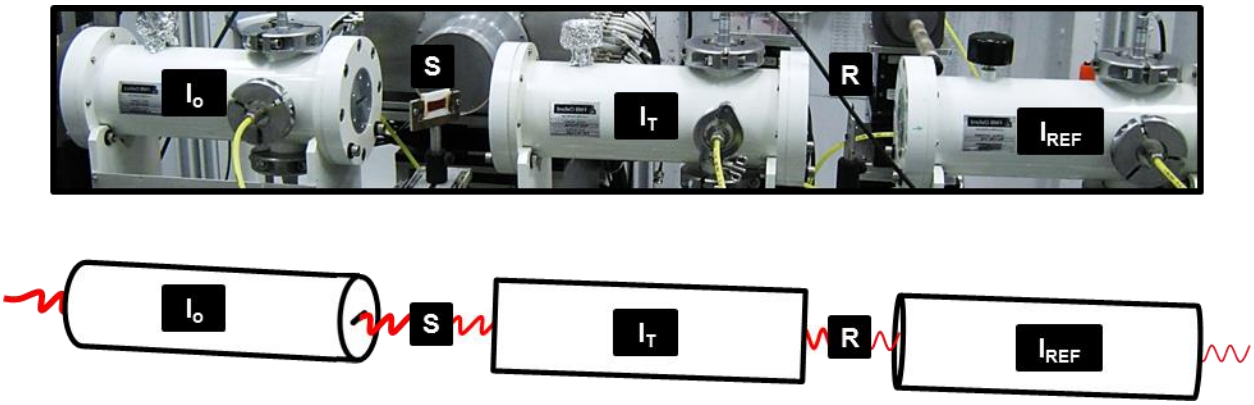

Figure 1.8. Hard X-ray transmission setup for the HXMA beamline (06ID-1), located at the Canadian Light Source in Saskatoon, SK. The gas-filled ionization chambers I_o and I_T measure the photon flux before and after the sample (S), while I_T and I_{REF} measure the photon flux before and after a reference material (R) for beamline energy calibration.

second detectors (I_o and I_T) measure the transmission through the material of interest (S), while the second and third detectors (I_T and I_{REF}) a well characterized standard (R). Often these standards are thin, high purity metal foils with known absorption edge energies that are used to calibrate the energy of the photon beam.[98,108] The open-air transmission setup is suitable for probing K-edges from elements with $Z \geq 20$, and $L_{2,3}$-edges from elements with $Z \geq 50$.[98,108] Molecules in the air are nearly transparent to hard X-rays and any photoabsorption that does occur will only contribute a small amount of intensity to the background photoabsorption in the spectrum.[83,84,94,99,108] Photoabsorption by air exponentially increases with decreasing photo energy, placing a practical limit on the photon energies that can be used in open-air transmission setups.[83,84,94,99,108] For example, the absorption path length of a 4 keV photon in air is approximately 10 cm, while for an 8 keV photon it is approximately 77 cm.[108] As a result, experiments using photon energies in the soft X-ray region requires an ultra-high vacuum setup, which is quite different from hard X-ray experiments.

1.4.2. *Soft X-ray Fluorescence Yield Experiments*

While *in vacuo* experiments avoid photoabsorption by air, the photon absorption path length in materials also decreases at lower photon energies. X-rays below 1 keV, like those used to probe the Al $L_{2,3}$-edge in this thesis, often have an absorption path length below 1 μm.[83,84,94,95,99] This requires incredibly thin, self-supported materials to allow sufficient transmittance for a measurement; often making transmission experiments physically impractical at low photon energies. That said, a measure of the absorption coefficient can be determined indirectly from fluorescence decay, which occurs when the photo-excited electron loses energy through photoemission and moves to a lower energy, unoccupied state (Figure 1.9.a).[83,84,94,95,99] In this setup, powdered material is mounted to a sample plate, transferred into an ultra-high

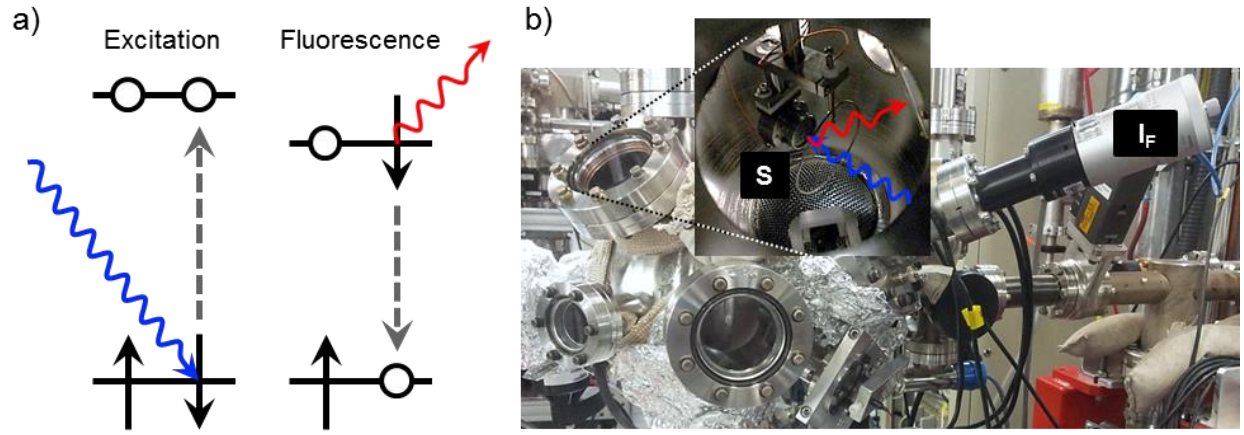

Figure 1.9. X-ray fluorescence process and fluorescence yield setup. **a)** A single photon is absorbed by an electron, exciting it into a higher energy state and leaving behind a core-hole (i.e., unoccupied state). The electron in the excited state non-radiatively relaxes to lower energy before emitting a photon and dropping to fill the core-hole. **b)** The ultra-high vacuum XAS chamber for the VLS-PGM Beamline (11ID-2) located at the Canadian Light Source in Saskatoon, SK. Entering via the beam pipe, the X-ray beam travels into the XAS chamber striking the sample (S), and the fluorescence (I_F) signal is collected at a detector attached to one of the chamber ports.

vacuum chamber, and irradiated with synchrotron light (Figure 1.9.b).[109] As long as the fluorescence intensity (I_F) from the material is linearly proportional to the number of excited states created by the incident photon flux (I_o), the fluorescence yield $\left(\frac{I_F}{I_o}\right)$ will be proportional to the absorption by the material (μx) as a function of the incident angle (θ) of I_o (Equation 1.4.).[83,84,94,95,99]

$$\frac{I_F}{I_o} \propto \frac{\mu x}{\sin(\theta)} \qquad \textbf{(1.4.)}$$

The incident angle is important for fluorescence yield measurements since it will affect the penetration depth and path length of the photons. [83,84,94,95,99]

The incident photon flux I_o is measured using a thin mesh of Au or Ni in the path of the photon beam. Due to the conducting nature of the mesh, photoelectrons that are lost from the mesh can be measured proportionally as an electric current. Thus, the amount of current drained into the mesh will be proportional to the photon flux in the beam. Following excitation, the fluorescent photon intensity is counted using a solid-state detector, such as a single crystal Si photodiode.[110] Like the XANES spectra collected using the hard X-ray transmission setup, the linear nature of the fluorescence yield allows the spectral features to be scaled to compare materials with different elemental concentrations.[89]

1.5. Thesis Overview

The work presented in this thesis has focused on understanding how composition, synthetic method, and annealing temperature affect cation site disorder in $Al_{1-x}Ga_xFeO_3$ materials. While $Ga_{2-x}Fe_xO_3$, and to a lesser extent $Al_{2-x}Fe_xO_3$, materials have received significant attention, the more complex quaternary compositions have remained largely

unexplored until now.[6,7,17] Studies on the ternary $Ga_{2-x}Fe_xO_3$ system have shown significant differences in material properties as a result of changes in composition, synthetic method, or annealing temperature; providing an impetus for systematically exploring the less studied, and more complex, quaternary $Al_{1-x}Ga_xFeO_3$ materials.[5,12,14-16]

Chapter Two addresses how substitution affects competing cation site preferences, and thus disorder, in the quaternary $Al_{1-x}Ga_xFeO_3$ system. In this study, materials from the $Al_{1-x}Ga_xFeO_3$ system were synthesized using the high temperature ceramic method and examined using XANES. The compositional complexity and resulting disorder in this quaternary system limits its study by model-based techniques, such as Mössbauer spectroscopy, neutron diffraction, or X-ray diffraction. XANES takes advantage of the element specific binding energies, and the differences in orbital symmetry of the tetrahedral and octahedral cation sites which allow changes in the average coordination number of Al^{3+}, Ga^{3+}, and Fe^{3+} to be examined.[84-86,93-95,97,99,100,103-106] In Chapter Three, $Al_{1-x}Ga_xFeO_3$ materials were synthesized via the citrate sol-gel and co-precipitation methods and used to compare the effect of synthetic method and annealing temperature on cation site disorder. These studies have contributed towards an understanding of the factors affecting cation site disorder in the $Al_{1-x}Ga_xFeO_3$ system. The disorder relationships elucidated in these studies, especially with regards to synthetic methods, may find broad applicability in the synthesis and optimization of properties in these, and other, metal oxide systems.

Chapter Two

2. An X-ray Absorption Spectroscopic Study of the Metal Site Preferences in $Al_{1-x}Ga_xFeO_3$ Materials[†]

2.1. Introduction

$GaFeO_3$, and to a lesser extent $AlFeO_3$, have been studied by a variety of methods such as X-ray and neutron diffraction, as well as Raman, Mössbauer and X-ray absorption spectroscopy.[4,6,14,31,33-36,55,58,61] As the crystal structure and mixed cation site occupancies are thought to be responsible for the properties of these materials, knowledge of these aspects is critical to understanding the electronic and magnetic ordering.[5,8,28] Unfortunately, X-ray and neutron diffraction have inherent problems when studying materials that are isomorphic with the non-centrosymmetric, orthorhombic $GaFeO_3$ crystal structure-type (see Figure 1.1., page 3). Rietveld refinement of X-ray and neutron diffraction data from the ternary $AlFeO_3$ and $GaFeO_3$ materials is non-trivial, as it suffers from having to refine the atomic positions of three elements across ten crystallographic sites (4 metal cation sites and 6 oxygen anion sites), with most not being special positions.[4,35] Significant cation site disorder is also a major issue in refining this system, as Fe^{3+} and Ga^{3+} have similar X-ray scattering factors which making them difficult to distinguish from each other, and Al^{3+} is a poor at scattering X-rays (relative to Fe^{3+} and Ga^{3+}).[36] These problems would present an even greater challenge if Rietveld refinement was attempted on powder diffraction data from the more complex quaternary $Al_{1-x}Ga_xFeO_3$ system.

A less common structural characterization technique, X-ray absorption near-edge

†A version of this chapter has been published. Reprinted with permission from J. D. S. Walker and A. P. Grosvenor, *Journal of Solid State Chemistry*, **2013**, *197*, 147-153. © 2012 Elsevier Inc. DOI: 10.1016/j.jssc.2012.09.015

spectroscopy (XANES), has been performed to better understand how the average coordination number of the cations changes with composition in the $Al_{1-x}Ga_xFeO_3$ system. XANES is a useful technique towards this end, as it can probe the coordination environment and charge of the cations in the material.[100,111] In this study, Al $L_{2,3}$-, Ga K-, and Fe K-edge XANES spectra were collected from $Al_{1-x}Ga_xFeO_3$ materials ($0 \leq x \leq 1$), synthesized using a high temperature ceramic method, to examine the effect of composition on the degree of cation site disorder present between the three octahedral cation sites (i.e., Fe_1, Fe_2, A_2; A = Al^{3+},Ga^{3+}) and the tetrahedral cation site.

2.2. Experimental Methods

2.2.1. *Synthesis of Materials*

$Al_{1-x}Ga_xFeO_3$ materials (x = 0.00, 0.15, 0.35, 0.50, 0.65, 0.85, 1.00) were synthesized by the ceramic method. Stoichiometric mixtures of α-Al_2O_3 (Sigma-Aldrich, 98%), Ga_2O_3 (Alfa Aesar, 99.99%) and α-Fe_2O_3 (Alfa Aesar, 99.945%) were ground, pressed into pellets at 6 MPa, and placed into alumina crucibles. The crucibles were put into a furnace at 600 °C and heated in air to 1350 °C over five hours, and then held at this temperature for three days before being quench cooled in air. The materials were then reground, pelleted as above, and annealed for another three days and then air quenched. In addition to purchased standards (α-Al_2O_3 [Sigma-Aldrich, 98%; 6-coordinate Al^{3+}]; Ga_2S_3 [Alfa Aesar, 99.99%; 4-coordinate Ga^{3+}], and GaF_3 [Alfa Aesar, 99.99%; 6-coordinate Ga^{3+}]), a series of β-$Ga_xAl_{2-x}O_3$ materials (x = 0.7, 1.0, 1.3, 1.7, 2.0; 4- and 6-coordinate Ga^{3+}/Al^{3+}) was also synthesized using the ceramic method described above to aid in the interpretation of the collected XANES spectra.[112,113]

The materials studied were determined to be phase pure by powder X-ray diffraction (XRD) using a PANalytical Empyrean system and Co $K\alpha_{1,2}$- or Cu $K\alpha_1$-radiation; select XRD

patterns from $Al_{1-x}Ga_xFeO_3$ and β-$Ga_xAl_{2-x}O_3$ materials are presented in Figure 2.1. The lattice parameters for $Al_{1-x}Ga_xFeO_3$ (Table 2.1.) and β-$Ga_xAl_{2-x}O_3$ (Table 2.2.) materials were determined from the XRD patterns using the X'Pert High Score Plus software from PANalytical.[114] The orthorhombic $GaFeO_3$ crystal structure-type (*Pna2₁*) was used for $Al_{1-x}Ga_xFeO_3$ materials, and the monoclinic β-Ga_2O_3 crystal structure-type (*C2/m*) was used for β-$Ga_xAl_{2-x}O_3$ materials.[112-113] The lattice constants were found to increase linearly in both systems with increasing Ga^{3+} content, in agreement with Vegard's law.[115,116] Additionally, the β-angle (°) determined for the β-$Ga_xAl_{2-x}O_3$ materials was found to decrease as the Ga^{3+} content was increased.

Table 2.1. Lattice constants for $Al_{1-x}Ga_xFeO_3$ materials synthesized via the ceramic method and adopting the orthorhombic $GaFeO_3$ crystal structure-type (*Pna2₁*).

x (Ga^{3+})	a (Å)	b (Å)	c (Å)	Volume (Å^3)
0.00	4.9832(3)	8.5544(6)	9.2390(6)	393.78(8)
0.15	4.9963(4)	8.5805(7)	9.2606(8)	397.0(1)
0.35	5.0154(3)	8.6170(7)	9.2893(7)	401.46(9)
0.50	5.0296(3)	8.6441(6)	9.3111(7)	404.82(8)
0.65	5.0438(4)	8.6708(8)	9.3339(8)	408.2(1)
0.85	5.0638(4)	8.7088(8)	9.3634(8)	412.9(1)
1.00	5.0789(4)	8.7400(8)	9.3857(9)	416.6(1)

Table 2.2. Lattice constants for β-$Ga_xAl_{2-x}O_3$ materials synthesized via the ceramic method and adopting the monoclinic β-Ga_2O_3 crystal structure-type (*C2/m*).

x (Ga^{3+})	a (Å)	b (Å)	c (Å)	β-angle (°)	Volume (Å^3)
0.7	11.9332(8)	2.9533(2)	5.6901(4)	104.065(3)	194.52(5)
1.0	12.0013(5)	2.9732(1)	5.7174(2)	104.039(2)	197.92(3)
1.3	12.0697(6)	2.9932(1)	5.7448(3)	103.992(2)	201.38(3)
1.7	12.1624(6)	3.0203(1)	5.7796(3)	103.903(2)	206.09(3)
2.0	12.2194(5)	3.0385(1)	5.8041(2)	103.846(2)	209.23(3)

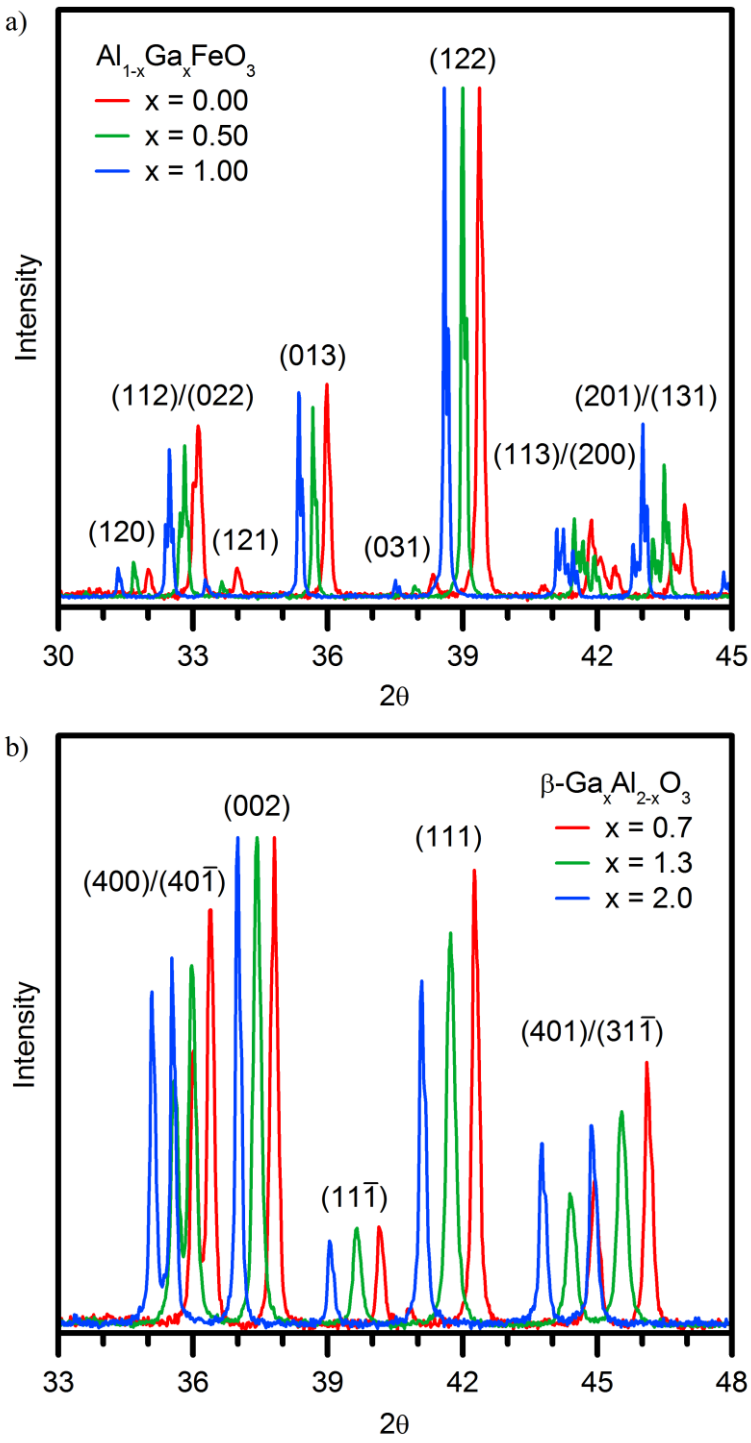

Figure 2.1. Powder X-ray diffraction patterns from: **a)** $Al_{1-x}Ga_xFeO_3$ materials, scaled to have equivalent (122) reflection intensities, and; **b)** β-$Ga_xAl_{2-x}O_3$ materials, scaled to have equivalent (002) reflection intensities. These materials were synthesized via the ceramic method, and the XRD patterns were collected using a Co X-ray source.

2.2.2. *Collection of Al $L_{2,3}$-edge XANES Spectra*

Al $L_{2,3}$-edge spectra from the $Al_{1-x}Ga_xFeO_3$ system were collected using the Variable Line Spacing Plane Grating Monochromator beamline (VLS-PGM, 11ID-2) located at the Canadian Light Source (CLS).[110] Materials were ground to a fine powder and mounted on carbon tape before being inserted into the ultra-high vacuum chamber. XANES spectra were collected in fluorescence yield mode using a 0.025 eV step through the absorption edge and an entrance slit of 50 x 50 μm^2. Additionally, Al $L_{2,3}$-edge XANES spectra were collected from α-Al_2O_3 and β-$Ga_xAl_{2-x}O_3$ materials. The Al $L_{2,3}$-edge spectra were calibrated by collecting a spectrum from Al metal foil (Alfa Aesar, 99.99%), and setting the peak maximum of the first derivative of the spectrum to 72.55 eV.[98]

2.2.3. *Collection of Ga and Fe K-edge XANES Spectra*

The Ga K- and Fe K-edge XANES spectra were collected in transmission mode using beamlines located at the CLS and at the Advanced Photon Source (APS; Argonne National Laboratory). XANES spectra from the CLS were collected using the Hard X-ray Microanalysis beamline (HXMA, 06ID-1) and a Si (111) double crystal monochromator. Spectra were collected at the APS using the Pacific Northwest Consortium/X-ray Science Division Collaborative Access Team (PNC/XSD-CAT, Sector 20) bending magnet beamline (20-BM), using Si (111) crystal monochromator.[117] Material preparation consisted of spreading a thin layer of finely powdered material between two pieces of Kapton tape. Multiple layers were stacked to ensure sufficient and uniform absorption of the X-rays by the material.

The Ga K-edge XANES spectra were collected using 0.20 eV steps through the absorption edge for Ga^{3+}-containing materials, and the Fe K-edge XANES spectra were collected using 0.15 eV steps through the absorption edge for the Fe^{3+}-containing materials. The spectra

were calibrated by concurrently collecting spectra from a reference material, and setting the peak maximum of the first derivative of the spectrum to a known value. The Ga K-edge XANES spectra collected at the CLS were calibrated using the synthesized β-Ga_2O_3 material, with the absorption edge energy set to 10371.2 eV. The absorption edge energy of β-Ga_2O_3 was determined by calibrating it to Zn metal foil, with the Zn K-edge absorption edge energy set to 9659 eV.[98] For spectra collected at the APS, Ga metal (sandwiched between two layers of Kapton tape) was used as a reference, with the absorption edge energy set to 10367 eV.[98] Fe metal foil was used as a reference, with the absorption edge energy set to 7112 eV for the Fe K-edge XANES spectra collected at both the CLS and APS.[98] All spectra collected were calibrated, normalized, and analyzed using the Athena software program.[108]

2.3. Results

2.3.1. *Al $L_{2,3}$-edge XANES*

The normalized Al $L_{2,3}$-edge XANES spectra from $AlPO_4$, α-Al_2O_3, and $Al_{1-x}Ga_xFeO_3$ materials are presented in Figure 2.2. These spectra result from the excitation of Al 2p electrons into unoccupied 3s- or 3d-states.[103,118] The lowest energy features in the absorption edge correspond to transitions into Al 3s-states, with the transitions into 3d-states observed higher in energy as broad, low intensity features.[118] In the final state, spin-orbit coupling of the Al 2p-states splits the absorption edge into the $2p_{3/2}$ and $2p_{1/2}$ peaks. In crystalline materials containing Al^{3+} with a single coordination number, the individual L_3- and L_2-edges can be resolved, with the energy of the absorption edge increasing by ~1.5 eV as the coordination number of Al^{3+} increases from four to six (Figure 2.2.a).[103] The increase in absorption energy as the coordination number of Al^{3+} increases can be explained as follows. As the number of electronegative atoms around the metal center increases, the core-hole potential is screened more

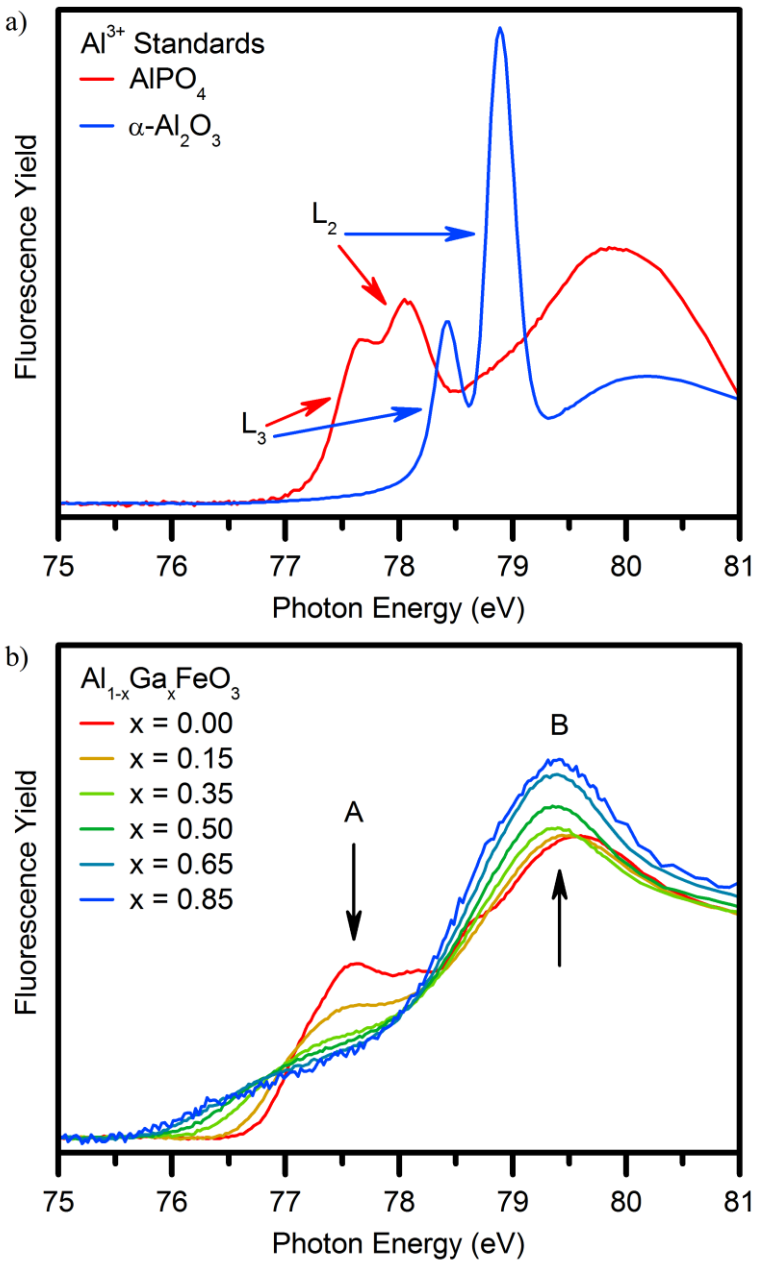

Figure 2.2. Normalized Al $L_{2,3}$-edge XANES spectra from **a)** $AlPO_4$ and α-Al_2O_3, and **b)** $Al_{1-x}Ga_xFeO_3$ materials. Due to the different Al^{3+} coordination environments, the features in the spectrum from $AlPO_4$ (4-coordinate Al^{3+}) are observed at lower energy relative to the features in the spectrum from α-Al_2O_3 (6-coordinate Al^{3+}). For $Al_{1-x}Ga_xFeO_3$ materials, the arrows indicate the change in intensity that occurs as the Ga^{3+} content in the material is increased. The average coordination number of Al^{3+} increases as the Ga^{3+} content in the material is increased. This is shown by the decrease in the intensity of feature A (4-coordinate Al^{3+}) and the increase in the intensity of feature B (6-coordinate Al^{3+}).

effectively, which increases the energy of the final state. This results in a greater difference in energy between the ground state and the final state, which is observed as an increase in the absorption energy.[103,119] These shifts in energy can pose problems when studying certain crystal systems, as the transitions can overlap when Al^{3+} is present in different coordination environments and cause significant broadening of the spectral features.[103] This can be observed in the Al $L_{2,3}$-edge spectra collected from $Al_{1-x}Ga_xFeO_3$ materials (Figure 2.2.b). Two features are present, which are assigned to Al 2p → 3s transitions originating from Al^{3+} in a 4-coordinate environment (feature A), and from Al^{3+} in a 6-coordiante environment (feature B).[103] While feature B is exclusively assigned to the 2p → 3s transition from 6-coordinate Al^{3+}, it is possible that this feature contains excitations from both 4- and 6-coordinate Al^{3+} given its asymmetric shape.[99] As Ga^{3+} is substituted for Al^{3+} in the $Al_{1-x}Ga_xFeO_3$ materials, feature A (4-coordinate Al^{3+}) broadens and decreases in intensity, and feature B (6-coordinate Al^{3+}) increases in intensity. That is, with increasing Ga^{3+} content in $Al_{1-x}Ga_xFeO_3$ materials, Al^{3+} increasingly occupies the three octahedral sites, and decreasingly occupies the tetrahedral A_1 site. The reason feature A broadens as the Ga^{3+} content is increased is not known, but could be due to the decreasing amount of Al^{3+} present in the tetrahedral A_1 site, in addition to the overall decrease in the Al^{3+} content.

2.3.2. *Ga K-edge XANES*

Normalized Ga K-edge XANES spectra, representing 1s → 4p transitions, are shown in Figure 2.3. Due to the decreased lifetime of the core-hole, the resolution in the Ga K-edge spectra is much lower than in the Al $L_{2,3}$-edge spectra which leads to broadening of the features in the spectra.[94] These spectra can be interpreted in a similar fashion as the Al $L_{2,3}$-edge spectra, as shown from the materials present in Figure 2.3.a. Ga^{3+} is 4-coordinate in Ga_2S_3, 6-coordinate

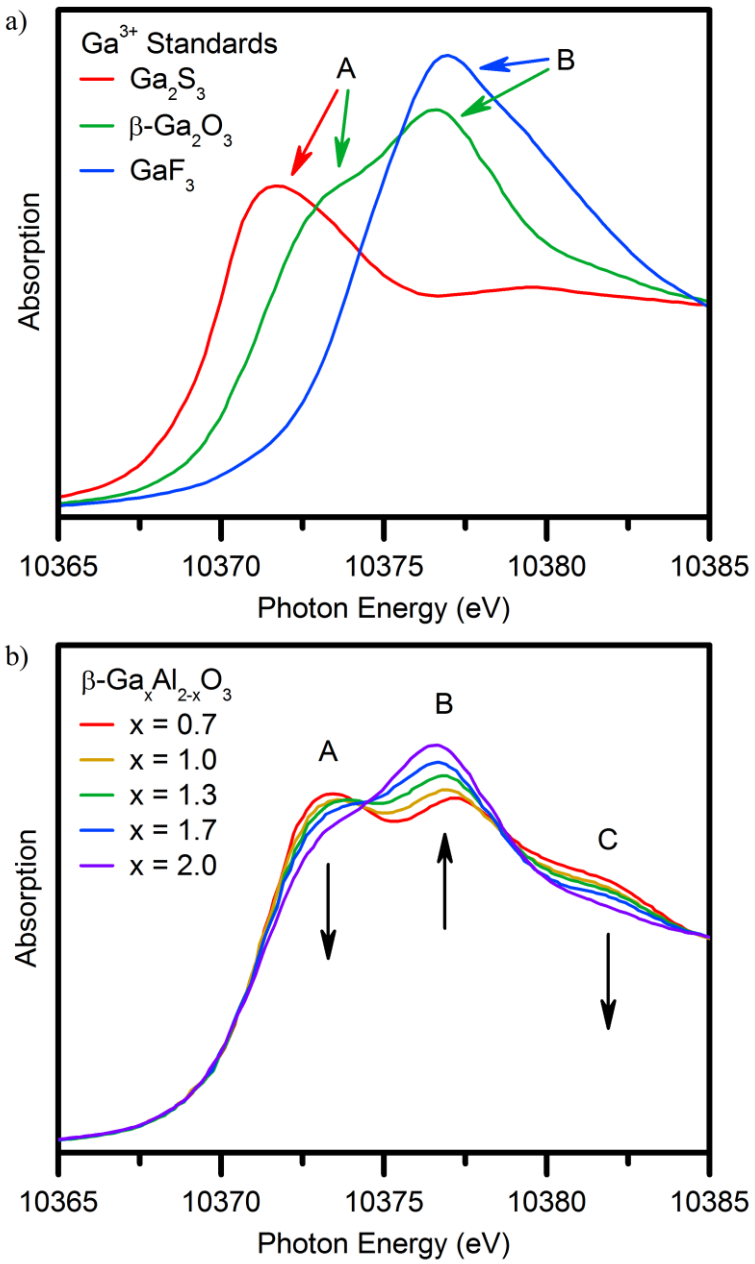

Figure 2.3. Normalized Ga K-edge XANES spectra from **a)** Ga_2S_3, β-Ga_2O_3, and GaF_3 materials, and **b)** β-$Ga_xAl_{2-x}O_3$ materials. The spectra from Ga_2S_3 (4-coordinate Ga^{3+}), β-Ga_2O_3 (4- and 6-coordinate Ga^{3+}), and GaF_3 (6-coordinate Ga^{3+}) materials show different absorption energies for 4-coordinate Ga^{3+} (feature A) and 6-coordinate Ga^{3+} (feature B). For β-$Ga_xAl_{2-x}O_3$ materials, the arrows indicate the change in intensity that occurs as the Ga^{3+} content in the material is increased. The average coordination number of Ga^{3+} was found to increase as the Ga^{3+} content in the material is increased. This is shown by the decrease in the intensity of feature A and the increase in the intensity of feature B.

in GaF_3, and there is a 1:1 ratio of 4- and 6-coordinate Ga^{3+} in β-Ga_2O_3. The Ga K-edge has two main features (labeled as A and B), which correspond to Ga^{3+} in different oxygen coordination environments. Through comparison of the XANES spectra collected from the Ga^{3+} standards, the lower energy feature (A) corresponds to Ga^{3+} in a 4-coordinate environment while the higher energy feature (B) corresponds to Ga^{3+} in a 6-coordinate environment.[104] To further support interpretation, Ga K-edge spectra were collected from a series of β-$Ga_xAl_{2-x}O_3$ materials (Figure 2.3.b). These phase pure materials adopt the monoclinic β-Ga_2O_3 structure (*C2/m*), which contains alternating layers of octahedral cation sites and tetrahedral cation sites.[112,113] As Ga^{3+} is substituted for Al^{3+} in the β-Ga_2O_3 crystal structure, the intensity of feature A decreases and the intensity of feature B increases. This observation indicates that Ga^{3+} has a preference to reside in the tetrahedral site when the Ga^{3+} content in β-$Ga_xAl_{2-x}O_3$ materials is low. Feature C, which was not present in the XANES spectra shown in Figure 2.3.a, is attributed to multi-scattering resonances and will not be discussed further.[104] The Al $L_{2,3}$-edge XANES spectra collected from β-$Ga_xAl_{2-x}O_3$ materials appear to confirm that Al^{3+} preferentially occupies the octahedral site with increasing Ga^{3+} content (Figure A1.1., page 76).

The Ga K-edge spectra from the $Al_{1-x}Ga_xFeO_3$ system (Figure 2.4.) show that as Ga^{3+} is exchanged for Al^{3+}, feature A decreases in intensity and feature B increases in intensity. It is important to note that while feature A decreases in intensity, this does not mean that Ga^{3+} occupies the tetrahedral site less. The intensity of the features results from a weighted average of the amount of Ga^{3+} present in each coordination environment. Thus, these results indicate that Ga^{3+} has a strong preference for occupying the tetrahedral A_1 site over the three octahedral sites when the Ga^{3+} content in the $Al_{1-x}Ga_xFeO_3$ materials is low. When the stoichiometric amount of Ga^{3+} in the crystal structure is greater than the stoichiometry of the tetrahedral sites, the average

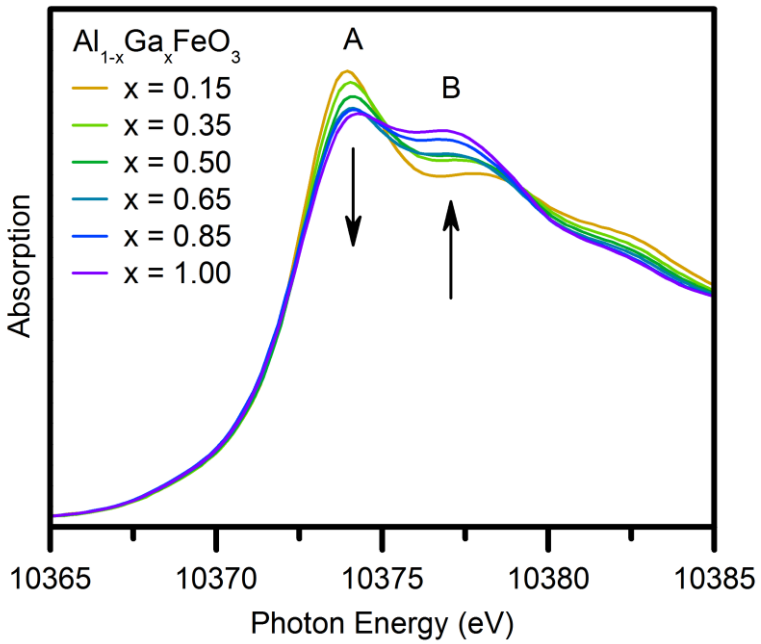

Figure 2.4. Normalized Ga K-edge XANES spectra from $Al_{1-x}Ga_xFeO_3$ materials, with arrows indicating the change in intensity that occurs as the Ga^{3+} content in the material is increased. The average coordination number of Ga^{3+} was found to increase as the Ga^{3+} content in the material is increased. This is shown by the decrease in the intensity of feature A (4-coordinate Ga^{3+}) and the increase in the intensity of feature B (6-coordinate Ga^{3+}).

coordination number of Ga^{3+} will increase as it is forced to occupy octahedral sites as well.

2.3.3. *Fe K-edge XANES*

The normalized Fe K-edge spectra from $Al_{1-x}Ga_xFeO_3$ display three features: feature A in the pre-edge region representing 1s → 3d transitions, and features B and C in the main-edge region representing 1s → 4p transitions (Figure 2.5.). The pre-edge region in the Fe K-edge spectra is sensitive to changes in oxidation state, site distortion, and coordination number.[105,106] The quadrupolar 1s → 3d transition is forbidden when Fe^{3+} is in a centrosymmetric environment (e.g., octahedral).[105] As the coordination number of Fe^{3+} decreases, inversion symmetry is lost and this leads to the mixing of the Fe 4p- and 3d-states, which results in an increase in the

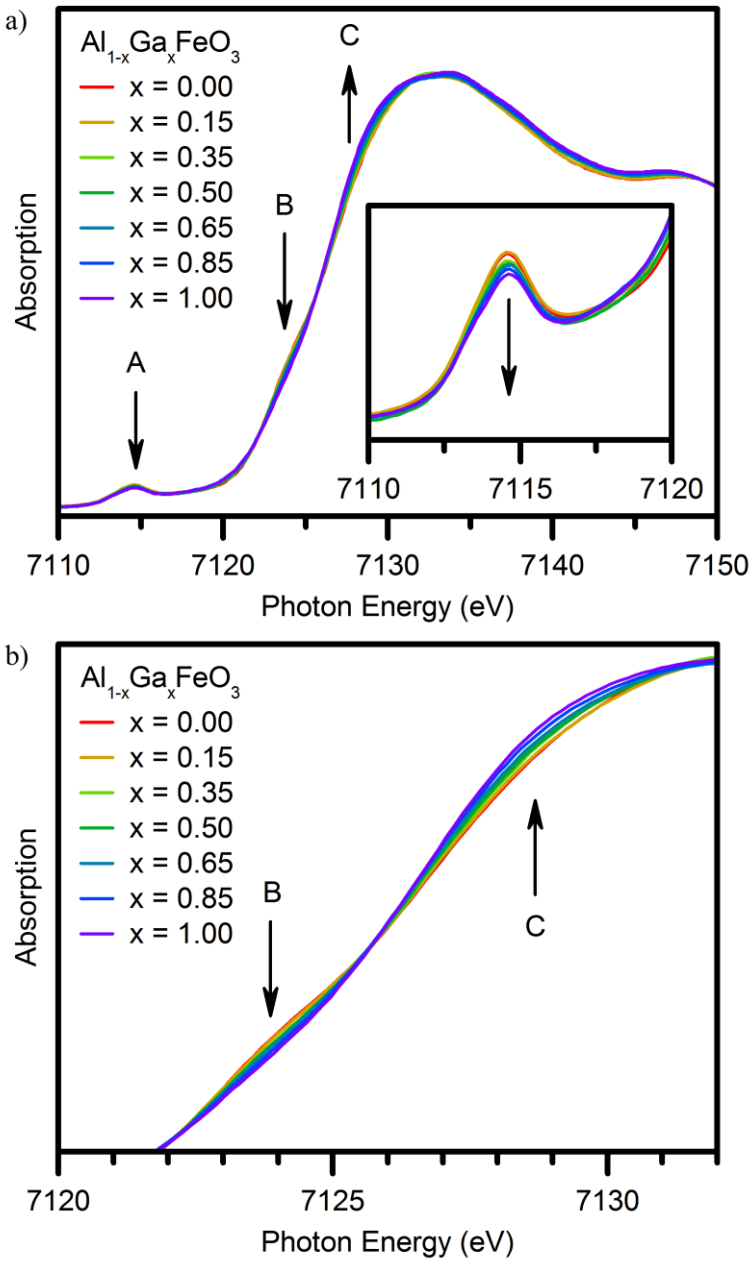

Figure 2.5. Normalized Fe K-edge XANES spectra from **a)** $Al_{1-x}Ga_xFeO_3$ materials, with an enhanced view of the pre-edge region (feature A) in inset, and **b)** an enhanced view of the main-edge region (features B and C). Arrows indicate the change in intensity that occurs as the Ga^{3+} content in the material is increased. The average coordination number of Fe^{3+} increases slightly as the Ga^{3+} content in the material is increased. This is shown by the decrease in the intensity of features A and B (4-coordinate Fe^{3+}), and the increase in the intensity of feature C (6-coordinate Fe^{3+}).

intensity of feature A. In $Al_{1-x}Ga_xFeO_3$ materials, the average coordination number of Fe^{3+}increases with greater Ga^{3+} content, as shown by the decrease in the intensity of the feature A in the Fe K-edge spectra. That is, a greater amount of Fe^{3+} is present at the tetrahedral A_1 site in $AlFeO_3$ materials than in $GaFeO_3$ materials.

The main-edge region of transition metal K-edge spectra can also be sensitive to changes in coordination number, with changes in the intensity of the features comprising the absorption edge as the average coordination number of the metal increases.[100,111] Using this rationale to interpret the features in the main-edge region of the Fe K-edge spectra from $Al_{1-x}Ga_xFeO_3$ materials, the lower energy feature (B) corresponds to Fe^{3+} in a 4-coordinate environment, while the higher energy feature (C) corresponds to Fe^{3+} in a 6-coordinate environment (Figure 2.5.b). Thus, as the Ga^{3+} content is increased, the relative amount of 4-coordinate Fe^{3+} (feature B) decreases and the relative amount of 6-coordinate Fe^{3+} (feature C) increases.

2.4. Discussion

2.4.1. *Compositional Effects on the Coordination Number of Al^{3+} and Ga^{3+}*

The XANES experiments show that Ga^{3+} prefers to reside in tetrahedral cation sites, while Al^{3+} prefers to reside in the octahedral cation sites. A d^{10} element like Ga^{3+} should have no preference for residing in tetrahedral or octahedral sites because of crystal field stabilization effects.[120] In comparison, Al^{3+} has no occupied d-states, which means that the crystal field stabilization energy cannot be used to argue for any particular site preference. Initially, the expectation would be for Al^{3+} to reside in the tetrahedral site more than Ga^{3+}, as Al^{3+} is smaller (4-coordinate ionic radii: $r_{Al^{3+}}$ = 0.39 Å; $r_{Ga^{3+}}$ = 0.47 Å).[116] Despite this, Ga^{3+} has been shown to prefer occupying tetrahedral cation sites in other crystalline oxide systems such as spinels, garnets, brownmillerites, and now this system.[112,119,121] The site preference of Al^{3+} is less

obvious, as there are examples of Al^{3+} preferring to reside in tetrahedral or octahedral cation sites depending on the oxide system under investigation.[112,119,122] This indicates that other factors are responsible for the Al^{3+}, Ga^{3+}, and Fe^{3+} cation site preferences in these materials.

It may be that in the $Al_{1-x}Ga_xFeO_3$ system, as has been shown in spinel-type oxides (and other systems), that the metal site preference is largely determined by ligand-metal s- and p-orbital interactions.[119,123] The tetrahedral site preference of Ga^{3+} can be explained by the d-block contraction, in which the poor screening of the nuclear charge by the fully occupied d-orbitals results in a greater effective nuclear charge acting on the Ga 4s- and 4p-states, pulling them closer to the nucleus.[119,121,124] This contraction allows better for overlap between the O 2p-states and the Ga 4s- and 4p-states, resulting in more covalent bonding interactions which allow Ga^{3+} to fit in to the smaller tetrahedral site.[119,121] Conversely, the higher energy s- and p-orbitals of Al^{3+} result in more ionic bonding interactions, as has been shown in other metal oxide systems.[119,121]

2.4.2. *Compositional Effects on the Coordination Number of Fe^{3+}*

The Fe K-edge spectra from $Al_{1-x}Ga_xFeO_3$ materials indicate that the average coordination number of Fe^{3+} increases as the Ga^{3+} content is increased. This indicates that Fe^{3+} occupies the tetrahedral A_1 site more in $AlFeO_3$ than in $GaFeO_3$, implying that the former has a greater amount of cation site disorder than the latter with respect to the distribution of Fe^{3+} between the three octahedral sites or the tetrahedral site. In comparison, multiple diffraction studies suggest that the Fe^{3+} occupation of the tetrahedral A_1 site is 0.10-0.15 for $AlFeO_3$ and 0.15-0.20 for $GaFeO_3$; indicating the presence of slightly more cation site disorder in $GaFeO_3$ which is in general disagreement with the results reported here.[4-6,31,33,35,55]

Magnetic studies can also be used to probe the amount of cation site disorder present

between the (A_1,Fe_1) cation sites and the (A_2,Fe_2) cation sites. This provides an indirect comparison to this current study, which has focused on cation site disorder between the three octahedral cation sites and the tetrahedral A_1 site. As mentioned previously, the ferrimagnetic moment in $Al_{1-x}Ga_xFeO_3$ materials arises from the uneven distribution of Fe^{3+} present in the A_1 and A_2 sites coupling with Fe^{3+} present in the Fe_1 and Fe_2 sites.[8] As such, more Fe^{3+} present at the tetrahedral A_1 site may help to stabilize the long-range magnetic ordering, and result in a higher magnetic transition temperature. Interestingly, when synthesized using the ceramic or citrate sol-gel methods, $AlFeO_3$ materials have a magnetic transition temperature between -23 ºC and 7 ºC (250 K and 280 K) while $GaFeO_3$ materials have a magnetic transition temperature between -83 ºC and -53 ºC (190 K and 220 K).[4,6,14,31,34,35,58,72] This implies that the cation disorder between the three octahedral cation sites and the tetrahedral A_1 site is greater in $AlFeO_3$ than in $GaFeO_3$, when these materials are synthesized at high temperature.[4,6,14,31,34,35,58,72]

These magnetic studies help substantiate the results of this present study, in which more Fe^{3+} was found in the three octahedral cation sites than the tetrahedral A_1 site as Ga^{3+} was substituted for Al^{3+}. This also supports the suggestion of more cation site disorder being present in $AlFeO_3$ than in $GaFeO_3$, in which there is a greater distribution of Fe^{3+} in the A_1 and A_2 sites in the former compared to the latter. However, $GaFeO_3$ materials synthesized at lower temperatures by citrate sol-gel or flux-based methods have been observed with magnetic transition temperatures as high as 27 ºC (300 K), indicating that the synthetic method may also play a role in determining cation site disorder within the $Al_{1-x}Ga_xFeO_3$ system.[35,36,54,63] Unfortunately, while phase pure $GaFeO_3$ has been prepared at temperatures ranging from 500 °C to 1400 ºC, obtaining phase pure $AlFeO_3$ outside of the narrow temperature range between 1320 °C and 1410 °C has been found to be exceptionally difficult despite multiple attempts using

low temperature methods.[35,64,71] Thus, while this study has unambiguously shown the effect of composition on cation site disorder in the $Al_{1-x}Ga_xFeO_3$ materials produced the ceramic method, the influence of other synthetic methods will require further investigation.

2.5. Conclusion

A series of phase pure $Al_{1-x}Ga_xFeO_3$ materials were synthesized and characterized by XANES to determine the change in the average coordination number of Al^{3+}, Ga^{3+}, and Fe^{3+}. From comparison with known and synthesized standards, it was found that Ga^{3+} prefers to reside in the tetrahedral A_1 site, while Al^{3+} and Fe^{3+} prefer to reside in the three octahedral sites. Ga^{3+} preferentially resides in the smaller tetrahedral site due to the greater overlap of the bonding orbitals between Ga^{3+} and O^{2-}, caused by the effect of the d-block contraction on the Ga s- and p-states.[121] The tetrahedral site preference of Ga^{3+} results in less cation site disorder being present in $Al_{1-x}Ga_xFeO_3$ materials is increased. This observation is supported by the magnetic property measurements reported for these materials, which have shown that $AlFeO_3$ has a higher magnetic transition temperature than $GaFeO_3$, and therefore a greater amount of cation site disorder. [4,6,14,31,34,35,58,72] The results from this study demonstrate the straightforward nature in which XANES can be used to examine changes in the average coordination number of main group and transition metals.

Chapter Three

3. The Effect of Synthetic Method and Annealing Temperature on Cation Site Disorder in $Al_{1-x}Ga_xFeO_3$ Materials‡

3.1. Introduction

In the $Al_{1-x}Ga_xFeO_3$ system examined in Chapter Two, it was shown that Fe^{3+} occupies the tetrahedral A_1 site less with increasing Ga^{3+} content, implying there is less cation site disorder in $GaFeO_3$ than in $AlFeO_3$. That said, there are still unanswered questions regarding the effect of synthetic conditions on $Al_{1-x}Ga_xFeO_3$ materials. The synthetic method has been shown to significantly affect the magnetic transition temperature observed in $Al_{2-x}Fe_xO_3$ and $Ga_{2-x}Fe_xO_3$ materials (Figure 1.4., page 9).[33,78] In particular, the magnetic transition temperature observed in $GaFeO_3$ materials synthesized using citrate sol-gel or flux techniques is between −15 °C and 10 °C (258 K and 283 K), while $GaFeO_3$ materials synthesized using the high temperature ceramic method have a magnetic transition temperature of −70 °C (203 K).[18,58,78] While these differences have been noted in the literature, there have been few attempts to directly compare and understand how different synthetic methods affect cation site disorder and the properties observed in these materials.[36,58,78] Additionally, use of more common characterization techniques such as X-ray or neutron diffraction to determine cation site occupancies has proven non-trivial for these materials. In contrast, X-ray absorption near-edge spectroscopy (XANES) is a tool well suited to examine the $Al_{1-x}Ga_xFeO_3$ materials, as it can probe the different coordination

‡A version of this chapter has been published. Reprinted with permission from J. D. S. Walker and A. P. Grosvenor, *Inorganic Chemistry*, **2013**, *52*, 8612-8620. © 2013 American Chemical Society DOI: 10.1021/ic4007636

environments of the constituent cations and does not rely on model fitting.[111,119] In this study, Al $L_{2,3}$-, Ga K-, and Fe K-edge XANES spectra were collected from five stoichiometries of the $Al_{1-x}Ga_xFeO_3$ system prepared by either the citrate sol-gel or by the co-precipitation method. These spectra were also compared to XANES spectra collected from $Al_{1-x}Ga_xFeO_3$ materials synthesized via the ceramic method that were initially presented in Chapter Two. In addition, annealing studies were performed on the materials synthesized via citrate sol-gel and co-precipitation methods to better understand how temperature affects metal site preference in this system.

3.2. Experimental Methods

3.2.1. *Synthesis of Materials*

$Al_{1-x}Ga_xFeO_3$ was synthesized using citrate sol-gel and co-precipitation methods. In the citrate sol-gel method, a 0.2 mol/L solution of the metal cations is made through addition of stoichiometric amounts of $Al(NO_3)_3 \cdot 9H_2O$ (Alfa Aesar, 98%), $Ga(NO_3)_3 \cdot xH_2O$ (Alfa Aesar, 99.9%), and $FeCl_3 \cdot 6H_2O$ (Alfa Aesar, 97.0%) to distilled water. The value of x was assumed to be 9 when calculating the mass of $Ga(NO_3)_3 \cdot xH_2O$ used, as it is relatively close to an experimentally determined value.[125] This assumption will cause small deviations in the reported stoichiometry, but this was not found to significantly affect the interpretation of the results. Ethylene glycol (Alfa Aesar, 99%) and citric acid monohydrate (EMD, 99%) were then added in equimolar amounts to the metal cation solution, to a concentration of 0.1 mol/L each. The solutions were heated to ~80 °C to drive off the solvent, and were subsequently decomposed by heating to 600 °C in air. The resulting solid material was then ground, pelleted at 6 MPa, placed into an alumina crucible, and annealed for approximately 40 hours at temperatures ranging from 900 °C to 1350 °C, before being quench cooled in air.

In the co-precipitation method, $Al_{1-x}Ga_xFeO_3$ materials ($0 \leq x \leq 1$) were made by weighing stoichiometric amounts of Al metal powder (Alfa Aesar, 99%), Ga_2O_3 (Alfa Aesar, 99.99%), and α-Fe_2O_3 (Alfa Aesar, 99.945%) into a beaker. Following this, 5-10 mL of 12.1 M HCl (Fischer Scientific, 37%) was added *very slowly* with heating and stirring to dissolve all of the reagents, resulting in a clear yellow solution. After the solution had cooled to room temperature, the metal ions were precipitated out of solution by titrating with 14.8 M NH_4OH (EMD Chemicals, 28.0-30.0%). The precipitate was filtered, dried overnight, and decomposed by heating to 800 ºC in air. The resulting material was ground, pelleted at 6 MPa, placed into an alumina crucible, and annealed for approximately 40 hours at temperatures ranging from 1000 °C to 1350 °C, before being quench cooled in air. It should be noted that higher annealing temperatures were required to form phase pure materials for Al^{3+}-rich compositions.[64,66] All materials studied were determined to be phase pure by powder X-ray diffraction using a PANalytical Empyrean diffractometer and either Cu or Co $K\alpha_{1,2}$ radiation. The lattice constants for the $Al_{1-x}Ga_xFeO_3$ materials were determined by the X'Pert HighScore Plus software from PANalytical using an orthorhombic $GaFeO_3$ crystal structure-type (*Pna2₁*).[4,5,114] When synthesized using the same annealing temperature, the lattice constants determined from $Al_{1-x}Ga_xFeO_3$ materials were found to increase linearly with greater Ga^{3+} content, in agreement with Vegard's law (Tables A2.1. and A2.2., page 77).[115,116] Figure 3.1. shows a diffraction pattern from materials produced via the citrate sol-gel method, with the peak widths decreasing as the annealing temperature increased (materials synthesized via the co-precipitation method show a similar trend). This decrease in peak width indicates that the diffraction planes in the crystallites become more periodic resulting in more discretely defined atomic planes. That is, the materials become more crystalline with increasing annealing temperature.

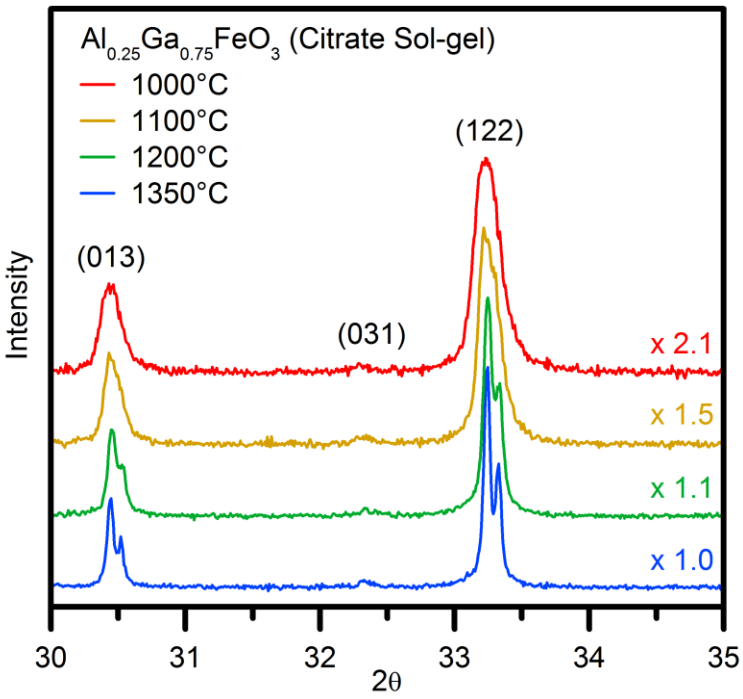

Figure 3.1. Powder X-ray diffraction patterns from $Al_{0.25}Ga_{0.75}FeO_3$ materials synthesized via the citrate sol-gel method and annealed at different temperatures. The XRD patterns were collected using a Cu X-ray source, and were scaled to have equivalent (122) reflection intensities (scaling factors are shown on the right). The peak widths decrease with increasing annealing temperature, indicating an increase in the crystallinity of the materials.

3.2.2. *Collection of Al $L_{2,3}$-, Ga K-, and Fe K-edge XANES Spectra*

For experimental details on the collection of the Al $L_{2,3}$-edge spectra presented in this chapter, see Section 2.2.2. (page 30). For details on the collection of the Ga K- and Fe K-edge spectra presented in this chapter, see Section 2.2.3. (page 30). To allow for direct comparison of the spectra presented for each absorption edge, all of the Al $L_{2,3}$-, Ga K-, and Fe K-edge XANES spectra from the $Al_{1-x}Ga_xFeO_3$ materials presented in this chapter are plotted using equivalent scales for the x-axis and the y-axis.

3.3. Results

3.3.1. *Al $L_{2,3}$-edge XANES*

The Al $L_{2,3}$-edge spectra from $Al_{1-x}Ga_xFeO_3$ synthesized by citrate sol-gel and co-precipitation methods and annealed at 1350 °C are shown in Figure 3.2. Two features are present in each spectrum, and are assigned to Al^{3+} present in 4-coordinate (feature A) and 6-coordinate environments (feature B). A detailed explanation of these assignments is provided in Section 2.3.1. (page 31). In both sets of Al $L_{2,3}$-edge XANES spectra presented, as the Ga^{3+} content increases, the intensity of feature A (4-coordinate A^{3+}) decreases and the intensity of feature B (6-coordinate Al^{3+}) increases. This indicates that when the Ga^{3+} content is low in $Al_{1-x}Ga_xFeO_3$ materials, Al^{3+} significantly occupies the octahedral sites and the tetrahedral A_1 site. With increasing Ga^{3+} content in these materials, Al^{3+} increasingly occupies the octahedral sites and decreasingly occupies the tetrahedral A_1 site, consistent the with results presented in Chapter Two.

Al $L_{2,3}$-edge spectra from $Al_{0.25}Ga_{0.75}FeO_3$ synthesized by the citrate sol-gel and co-precipitation methods, and annealed at different temperatures, are presented in Figure 3.3. (for additional compositions see Figures A2.1. and A2.2., page 80-81). As the changes with temperature are small, it is easier to see how the spectra change by comparing the ratio of the octahedral peak intensity to the tetrahedral peak intensity (feature B : feature A), which is shown for all compositions and annealing temperatures in Figure 3.4. (this data is summarized in Tables A2.3 to A2.5., page 78). In this plot, changes in composition result in larger changes in the peak intensity ratio than changes in annealing temperature. This indicates that in $Al_{1-x}Ga_xFeO_3$, composition has a larger effect on the site preference of Al^{3+} than annealing temperature. That said, the octahedral to tetrahedral peak intensity ratio does increase slightly

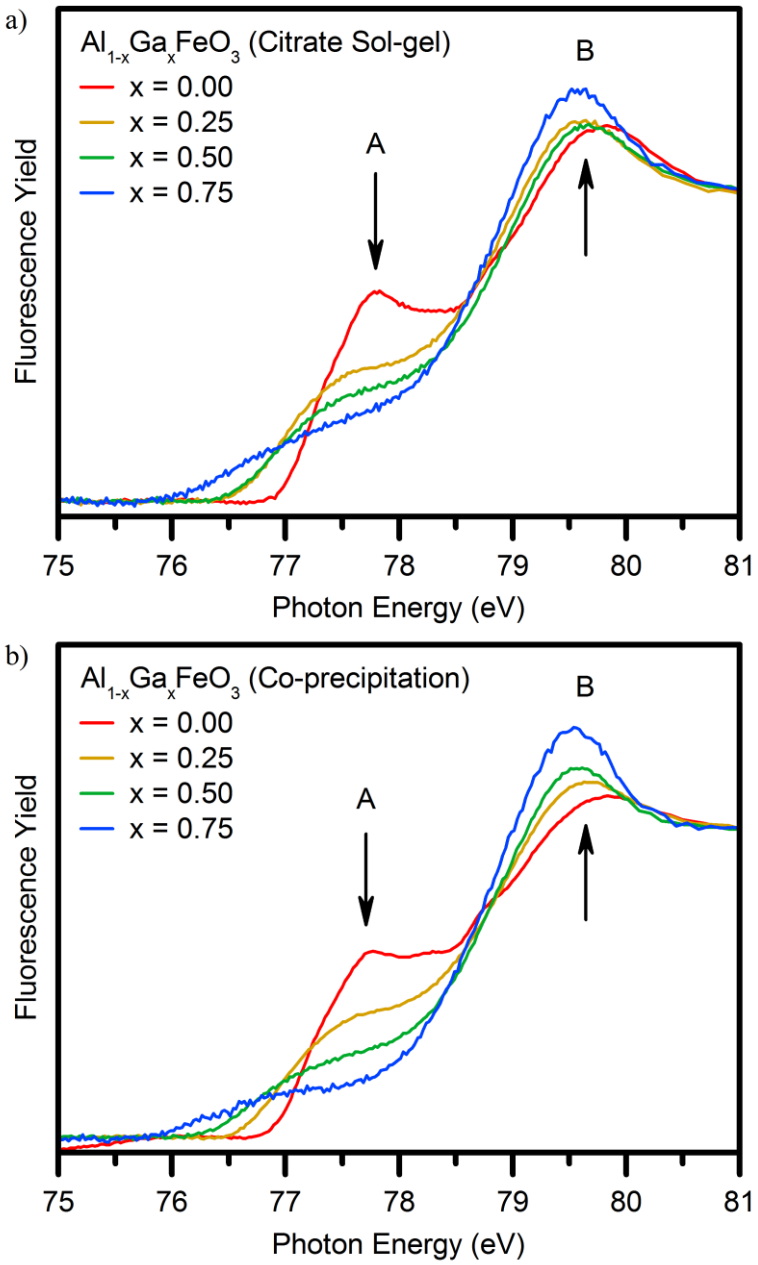

Figure 3.2. Normalized Al $L_{2,3}$-edge XANES spectra from $Al_{1-x}Ga_xFeO_3$ materials synthesized at 1350 °C via **a)** the citrate sol-gel method, and **b)** the co-precipitation method. Arrows indicate the change in intensity that occurs as the Ga^{3+} content in the material is increased. For both synthetic methods, the average coordination number of Al^{3+} increases as the Ga^{3+} content is increased. This is shown by the decrease in the intensity of feature A (4-coordinate Al^{3+}) and the increase in the intensity of feature B (6-coordinate Al^{3+}).

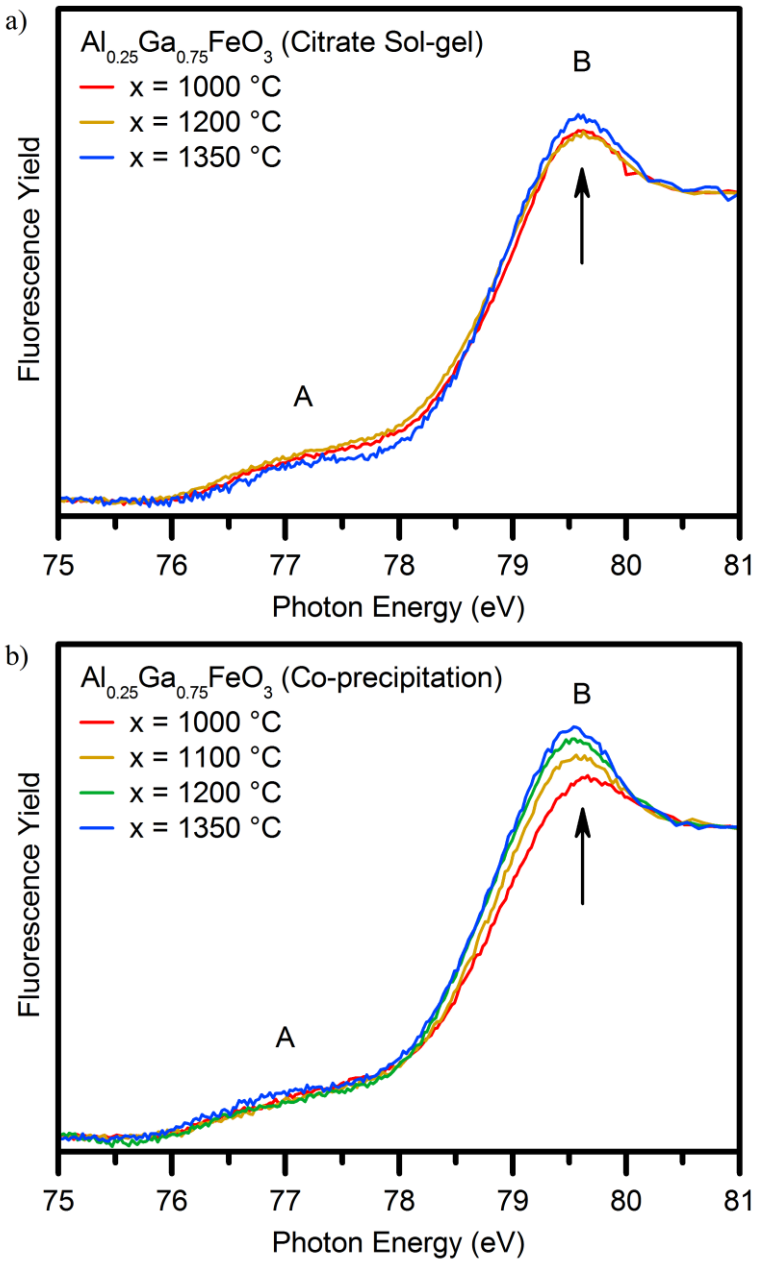

Figure 3.3. Normalized Al $L_{2,3}$-edge XANES spectra from $Al_{0.25}Ga_{0.75}FeO_3$ materials synthesized at different annealing temperatures via **a)** the citrate sol-gel method, and **b)** the co-precipitation method. Arrows indicate the change in intensity that occurs with increasing annealing temperature. For both synthetic methods, the average coordination number of Al^{3+} increases as the annealing temperature is increased. This is shown by the increase in the intensity of feature B intensity (6-coordinate Al^{3+}). Changes in the intensity of feature A (4-coordinate Al^{3+}) were not observed, which may be due to the low Al^{3+} content in these materials.

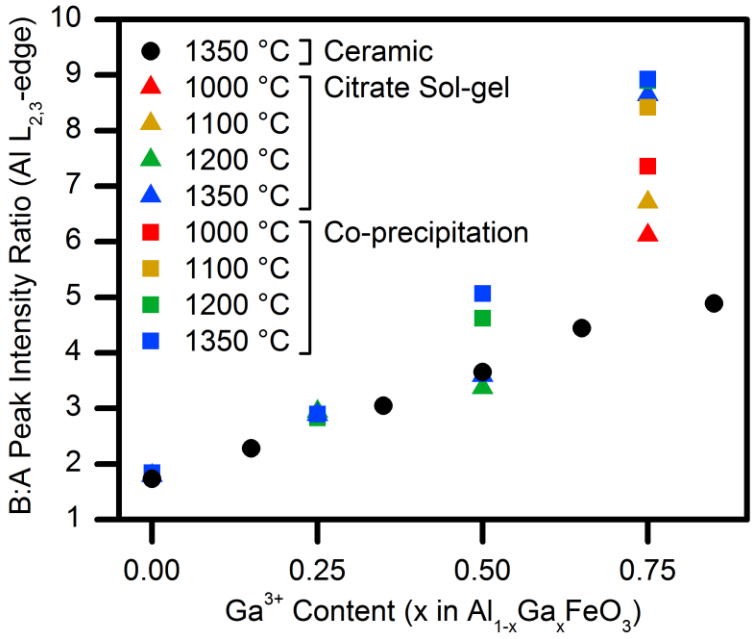

Figure 3.4. Octahedral peak intensity to tetrahedral peak intensity ratios (feature B : feature A) observed in the Al $L_{2,3}$-edge XANES spectra from $Al_{1-x}Ga_xFeO_3$ materials presented in this thesis. The average coordination number of Al^{3+} was found to increase as the Ga^{3+} content in the material was increased and as the annealing temperature was increased.

with increasing annealing temperature when the Ga^{3+} content is high ($x \geq 0.50$), which indicates that the amount of 6-coordinate Al^{3+} increases relative to the amount of 4-coordinate Al^{3+}. These ratios are not quantitative, but do allow for a comparison of the different materials studied. The $Al_{1-x}Ga_xFeO_3$ materials prepared using the co-precipitation method show a greater amount of Al^{3+} present in the octahedral sites than the materials prepared via the citrate sol-gel or ceramic methods (when $x \geq 0.50$). As well, materials synthesized via the co-precipitation method with low Al^{3+} content (high Ga^{3+} content) show a greater variance in the peak intensity ratios with changes in annealing temperature than materials produced using the citrate sol-gel method. This suggests that there is greater ion mobility when materials are synthesized by the co-precipitation method, while the citrate sol-gel and ceramic methods appear to suppress changes in the average

coordination number of Al^{3+} as the annealing temperature is varied.

3.3.2. *Ga K-edge XANES*

The Ga K-edge XANES spectra from $Al_{1-x}Ga_xFeO_3$ materials synthesized by citrate sol-gel and co-precipitation methods, and annealed at 1350 °C, are presented in Figure 3.5. These spectra result from 1s → 4p transitions and shift to higher energy with increasing coordination number.[104] In these materials, feature A is assigned to Ga^{3+} present at the tetrahedral A_1 site, while feature B is assigned to Ga^{3+} present at the octahedral sites.[104] A detailed explanation of these assignments is provided in Section 2.3.2 (page 33). Ga K-edge spectra from $Al_{1-x}Ga_xFeO_3$ materials synthesized via the citrate sol-gel method show negligible spectral changes when x = 0.25 and 0.50 (Figure 3.5.a). As x increases above 0.50, the intensity of feature A decreases and the intensity of feature B increases. In comparison, spectra from materials formed via the co-precipitation method show changes between all four compositions studied, although the changes are less obvious between x = 0.75 and 1.00 due to issues with normalizing these spectra. Overall, these observations imply that Ga^{3+} preferentially occupies the tetrahedral A_1 site when the Ga^{3+} content is low, and increasingly occupies the octahedral sites as the Ga^{3+} content is increased in $Al_{1-x}Ga_xFeO_3$ materials. This observation is in agreement with analysis of Ga K-edge XANES data from $Al_{1-x}Ga_xFeO_3$ materials synthesized via the ceramic method presented in Chapter Two.

The Ga K-edge spectra from $Al_{0.25}Ga_{0.75}FeO_3$ synthesized at different annealing temperatures by the citrate sol-gel and co-precipitation methods are presented in Figure 3.6. (for additional stoichiometries see Figures A2.3. and A2.4., page 82-85). The octahedral to tetrahedral peak intensity ratios (feature B : feature A) determined from the Ga K-edge spectra

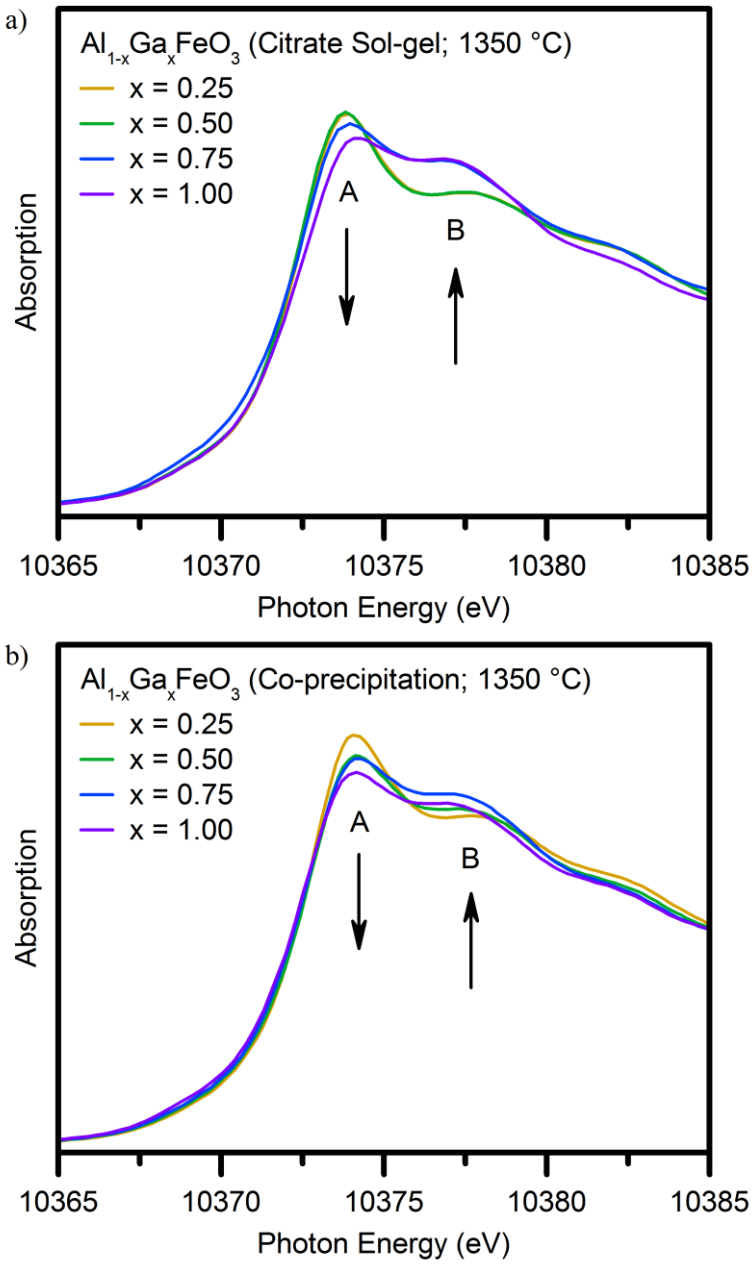

Figure 3.5. Normalized Ga K-edge XANES spectra from $Al_{1-x}Ga_xFeO_3$ materials synthesized at 1350 °C via **a)** the citrate sol-gel method, and **b)** the co-precipitation method. Arrows indicate the relative change in intensity that occurs as the Ga^{3+} content in the material is increased. For both synthetic methods, the average coordination number of Ga^{3+} increases as the Ga^{3+} content in the material is increased. This is shown by the decrease in the intensity of feature A (4-coordinate Ga^{3+}) and the increase in the intensity of feature B (6-coordinate Ga^{3+}).

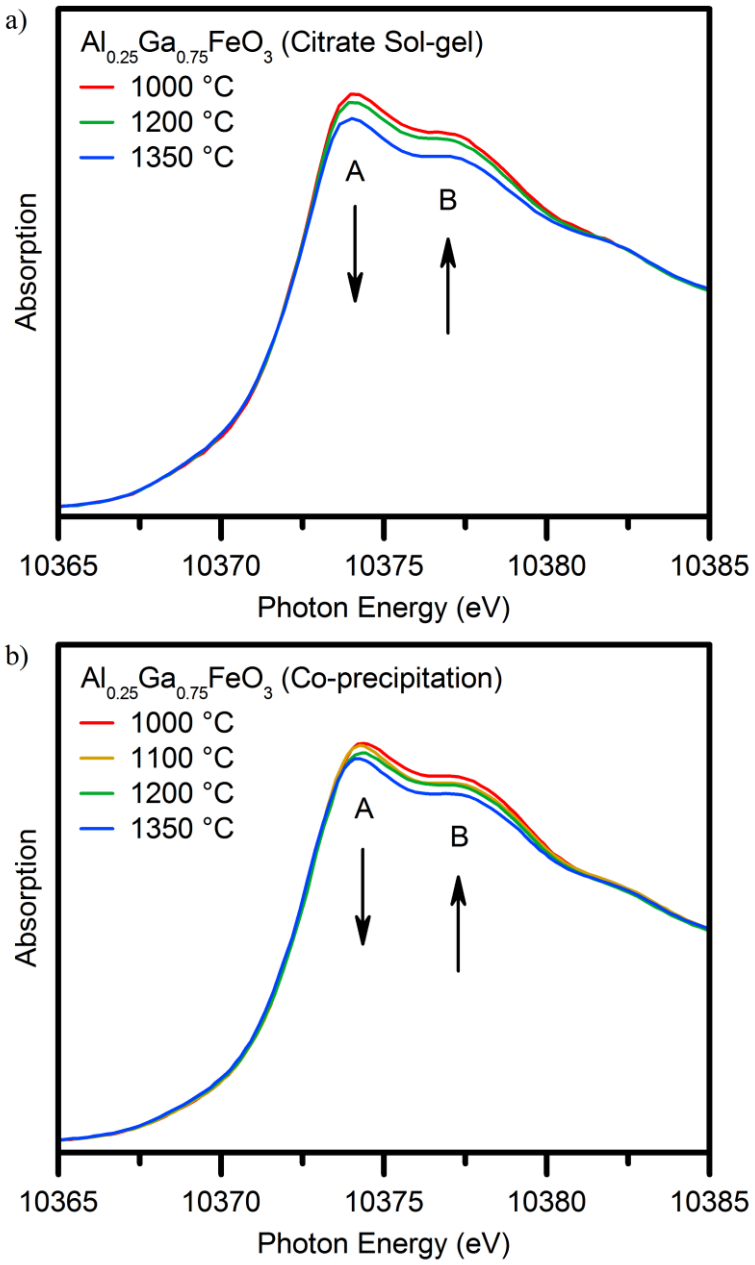

Figure 3.6. Normalized Ga K-edge XANES spectra from $Al_{0.25}Ga_{0.75}FeO_3$ materials synthesized at multiple annealing temperatures via **a)** the citrate sol-gel method, and **b)** the co-precipitation method. Arrows indicate the change in intensity that occurs as the annealing temperature is increased. For both synthetic methods, the average coordination number of Ga^{3+} increases as the annealing temperature is increased. This is shown by the decrease in the intensity of feature A (4-coordinate Ga^{3+}) and the increase in the intensity of feature B (6-coordinate Ga^{3+}).

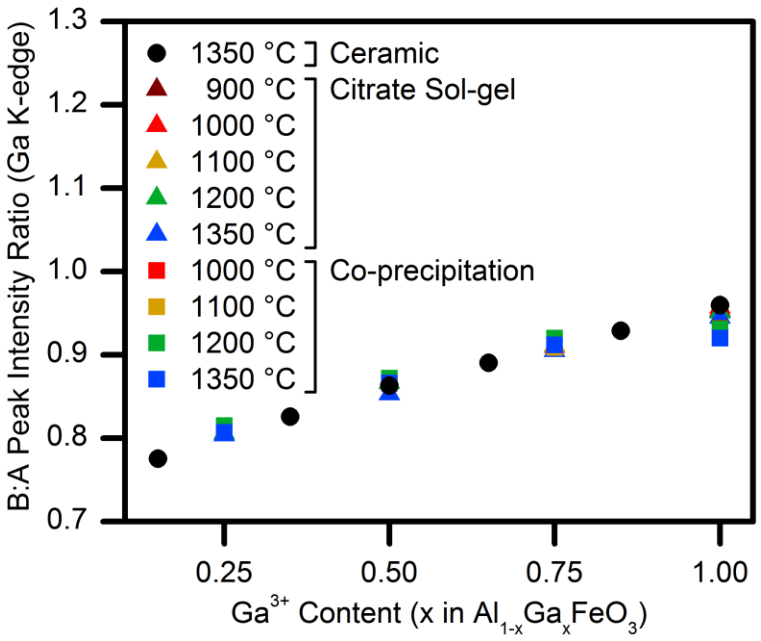

Figure 3.7. Octahedral peak intensity to tetrahedral peak intensity ratios (feature B : feature A) observed in the Ga K-edge XANES spectra from $Al_{1-x}Ga_xFeO_3$ materials presented in this thesis. The average coordination number of Ga^{3+} is observed to increase when the Ga^{3+} content in the material is increased. Annealing temperature appears to have much less impact on the average coordination number of Ga^{3+} than was shown for the average coordination number of Al^{3+}.

collected are shown in Figure 3.7. (this data is summarized in Tables A2.6. to A2.8., page 78-79). In comparison with the Al $L_{2,3}$-edge results, the Ga K-edge spectra show significantly smaller changes in the octahedral to tetrahedral peak intensity ratio with changes in annealing temperature. The peak intensity ratio changes very little with increasing annealing temperature; however, the overall intensity of tetrahedral and octahedral features decreased with increasing annealing temperature. The overall decrease in intensity is thought to be due to changes in the density of unoccupied states as the materials become more crystalline, but is beyond the scope of this study and will not be discussed further. The small variation in octahedral to tetrahedral peak intensity ratio indicates that the coordination environment of Ga^{3+} changes very little with

annealing temperature or synthetic method. That said, changes may be difficult to observe due differences in the core-hole lifetime, leading to a larger intrinsic line width for the Ga K-edge transition (1.82 eV) relative to the Al $L_{2,3}$-edge transition (0.004 eV).[101]

3.3.3. *Fe K-edge XANES*

Normalized Fe K-edge XANES spectra from $Al_{1-x}Ga_xFeO_3$ materials synthesized by both the citrate sol-gel and co-precipitation methods, and annealed at 1350 °C, are presented in Figure 3.8. The pre-edge feature is due to quadrupolar 1s → 3d transitions (feature A) while the main-edge represents dipolar 1s → 4p transitions (features B and C).[105] A detailed explanation of these assignments is provided in Section 2.3.3. (page 36). In short, as the average coordination number of Fe^{3+} decreases, features A and B (4-coordinate Fe^{3+}) will increase in intensity and feature C (6-coordinate Fe^{3+}) will decrease in intensity.[95,105]

An expanded view of the pre-edge region of the Fe K-edge spectra collected from $Al_{1-x}Ga_xFeO_3$ is presented in the inset of Figure 3.8. Regardless of synthetic method, features A and B decrease in intensity while feature C increases in intensity with increasing Ga^{3+} content for all materials studied. Thus, the average coordination number of Fe^{3+} was found to increase as the Ga^{3+} content was increased in these materials. Changes in the main-edge region of Fe K-edge XANES spectra, because of a change in the average Fe^{3+} coordination number, has also been observed in other oxide systems such as materials adopting the Brownmillerite crystal structure-type (e.g., $Ca_2M_xFe_{2-x}O_5$; M = Mn^{3+}, Fe^{3+}, Co^{3+}, Al^{3+}, Ga^{3+}).[100,111]

Unlike the Al $L_{2,3}$-edge and Ga K-edge XANES spectra, the Fe K-edge spectra only indicate minor differences between synthetic methods. Figure 3.9. shows a comparison between $AlFeO_3$ and $GaFeO_3$ materials synthesized via the citrate sol-gel, co-precipitation, and ceramic methods. For both compositions, the highest average Fe^{3+} coordination number (lowest pre-edge

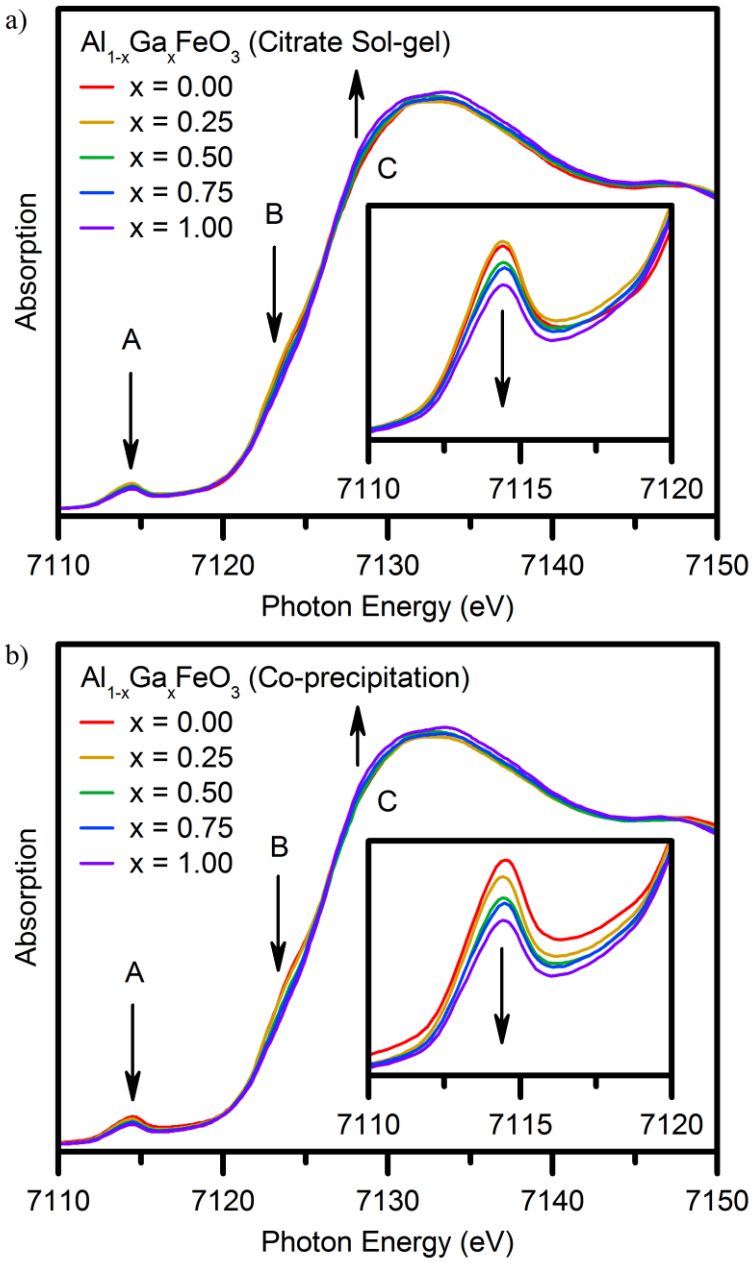

Figure 3.8. Normalized Fe K-edge XANES spectra from $Al_{1-x}Ga_xFeO_3$ materials synthesized at 1350 °C via **a)** the citrate sol-gel method, and **b)** the co-precipitation method. Arrows indicate the change in intensity that occurs as the Ga^{3+} content in the material is increased, and the insets show an enlarged view of the pre-edge region (feature A). For both synthetic methods, the average coordination number of Fe^{3+} increases slightly as the Ga^{3+} content in the material is increased. This is shown by the decrease in the intensity of features A and B (4-coordinate Fe^{3+}), and the increase in the intensity of feature C (6-coordinate Fe^{3+}).

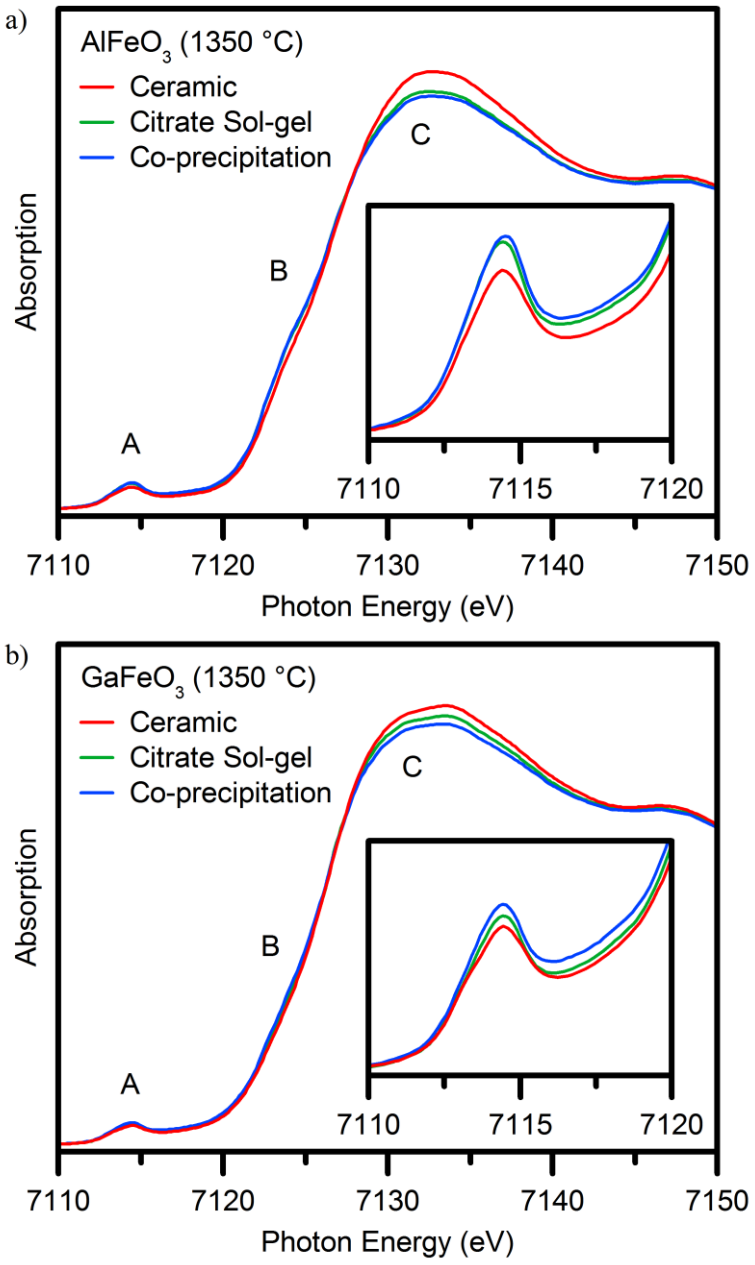

Figure 3.9. Normalized Fe K-edge XANES spectra from **a)** $AlFeO_3$, and **b)** $GaFeO_3$ materials synthesized at 1350 °C via the co-precipitation, citrate sol-gel, or ceramic methods. The insets show an enlarged view of the pre-edge region (feature A). $AlFeO_3$ and $GaFeO_3$ materials synthesized using the co-precipitation method show the lowest average Fe^{3+} coordination number, followed by the citrate sol-gel and ceramic methods, respectively. This is shown the decrease in the intensity of features A and B (4-coordinate Fe^{3+}), and the increase in the intensity of feature C (6-coordinate Fe^{3+}), for the materials synthesized by different methods.

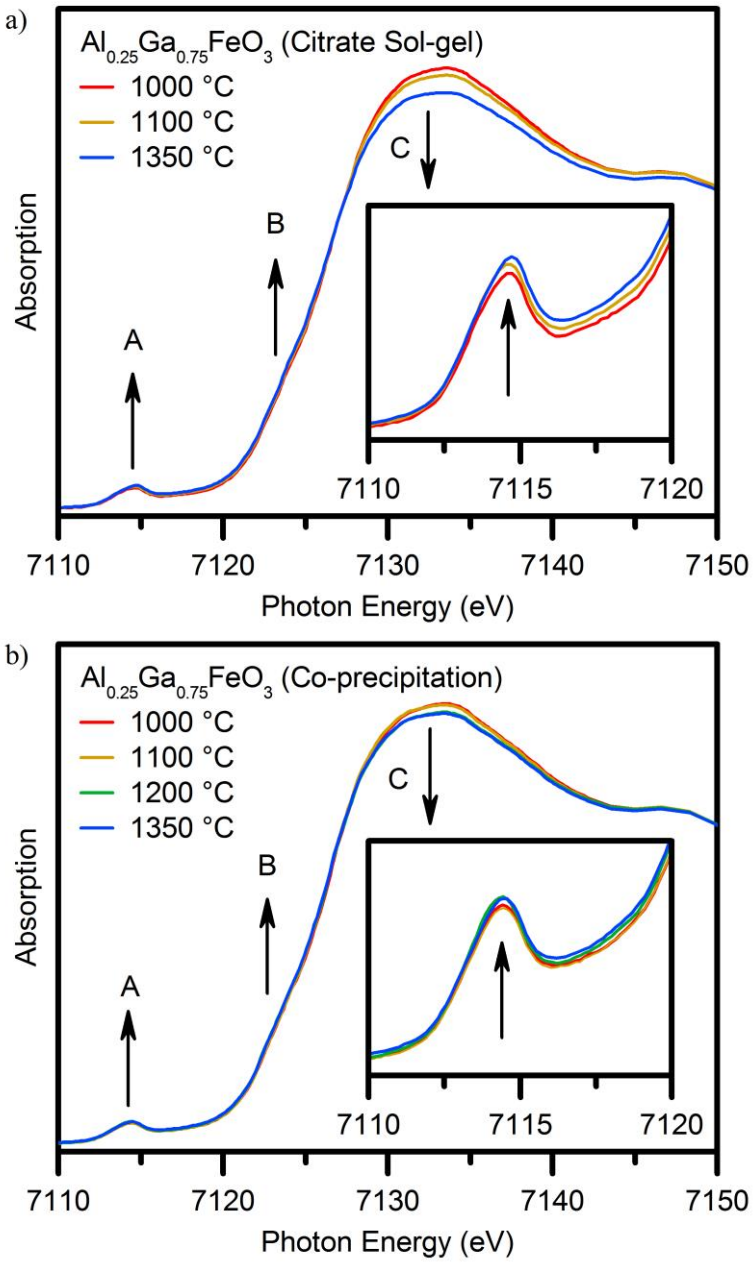

Figure 3.10. Normalized Fe K-edge XANES spectra from $Al_{0.25}Ga_{0.75}FeO_3$ materials synthesized at multiple annealing temperatures via **a)** the citrate sol-gel method, and **b)** the co-precipitation method. Arrows indicate the change in intensity that occurs as the annealing temperature is increased, and the insets show an enlarged view of the pre-edge region (feature A). For both synthetic methods, the average coordination number of Fe^{3+} decreases as the annealing temperature is increased. This is shown by the increase in the intensity of features A and B (4-coordinate Fe^{3+}) and the decrease in the intensity of feature C (6-coordinate Fe^{3+}).

intensity) is observed for materials synthesized via the ceramic method, followed by the citrate sol-gel method and the co-precipitation method, respectively. This is attributed to differences in how the material forms during synthesis, and will be discussed below. Like the Al $L_{2,3}$-edge spectra, the Fe K-edge spectra from $Al_{0.25}Ga_{0.75}FeO_3$ materials synthesized by citrate sol-gel and co-precipitation methods show changes in the average coordination number of Fe^{3+} with annealing temperature (Figure 3.10.; for additional compositions see Figures A2.5. and A2.6., page 86-89). With increasing annealing temperature, and regardless of composition or synthetic method, features A and B increase in intensity, and feature C decreases in intensity. This indicates that the average coordination number of Fe^{3+} decreases with increasing annealing temperature. As shown earlier, the average coordination number of Al^{3+} was found to increase with increasing annealing temperature, while the average coordination number of Ga^{3+} was not found to change significantly. Taken together, these observations suggest that Al^{3+} and Fe^{3+} exchange sites with each other, and not with Ga^{3+}, with increasing annealing temperature.

3.4. Discussion

3.4.1. *Changes in Metal Coordination Number with Composition*

The Al $L_{2,3}$-, Ga K-, and Fe K-edge XANES experiments have shown that in $Al_{1-x}Ga_xFeO_3$ materials, Al^{3+} and Fe^{3+} prefer to reside in octahedral sites while Ga^{3+} prefers to reside in the tetrahedral site, regardless of the synthetic method used. This is consistent with experimental observations and theoretical predictions of octahedral site preference energies for these three cations.[29,126,127] It has been proposed that ionic radii, as well as the valence s- and p-states interacting with the anion, are the major factors determining site preference, with crystal field stabilization energy having a smaller contribution in the solid state.[121,122,127] In the case of Ga^{3+}, the complete electron d-shell poorly shields the nuclear charge, resulting in the 4s- and

4p-states experiencing a greater effective nuclear charge.[119,121] Thus, the Ga 4s- and 4p-states are found at lower energies relative to the Al 3s- and 3p-states.[119,121] The lower energy of the Ga 4s- and 4p-states leads to greater overlap with the O 2p-states, favoring a covalent Ga-O bond.[119] As the Al^{3+} valence states are higher in energy than the Ga valence states, the Al 3s- and 3p-states do not overlap as effectively with the O 2p-states, favoring a more ionic bond.[121,122] As greater orbital overlap is favored in the smaller tetrahedral site, Ga^{3+} preferentially occupies the tetrahedral A_1 site over Al^{3+} or Fe^{3+}.[126]

The site preference of Fe^{3+} can be difficult to predict without computation due to confounding factors such as magnetic interactions between sites, as well as the effect of the d-orbitals.[99] The Fe K-edge XANES spectra from in $Al_{1-x}Ga_xFeO_3$ materials studied here indicate that Fe^{3+} predominantly resides in octahedral sites, and that the average coordination number of Fe^{3+} increases as Ga^{3+} replaces Al^{3+} in the crystal structure. This is due to the tetrahedral site preference of Ga^{3+}, which inhibits Fe^{3+} from occupying the tetrahedral site. In comparison, Al^{3+} prefers to reside in octahedral sites and competes with Fe^{3+} for those sites, resulting in an increase in the amount of Fe^{3+} present in the tetrahedral site when the Al^{3+} concentration is high. As the amount of 4-coordinate Fe^{3+} decreases as the Ga^{3+} content increases, this indicates that there is greater cation site disorder in $AlFeO_3$ than in $GaFeO_3$, consistent with the results from Chapter Two.

3.4.2. *Changes in Metal Coordination Number with Synthetic Method*

In the citrate sol-gel method, the citrate anion not only chelates the metals, but also undergoes a condensation reaction with the ethylene glycol to produce a long-range polymeric network.[53] Thus, the more subtle changes in the average coordination number of Al^{3+} observed in $Al_{1-x}Ga_xFeO_3$ materials produced by the citrate sol-gel method, as compared to the

co-precipitation method, are attributed to the organic network that is formed. This network could inhibit cation mobility during formation of the oxide crystal structure. Conversely, in materials synthesized via the co-precipitation method, the metals are not bound in any sort of long-range network and should instead be a mix of metal cations and counter-anions. Since there is no long-range network, cation diffusion should be faster, which explains the greater variation in the average coordination number of the metals when $Al_{1-x}Ga_xFeO_3$ materials are produced using the co-precipitation method. In contrast, materials synthesized by the ceramic method have low ion mobility, which is due to the significant energy required to break the metal-oxygen bonds and for the metal cations to diffuse through the crystal lattice. Thus, $Al_{1-x}Ga_xFeO_3$ materials prepared via the co-precipitation method show greater change in the average coordination number of the cations than those produced via the citrate sol-gel or ceramic methods.

3.4.3. *Changes in Metal Coordination Number with Annealing Temperature*

During the synthesis of $Al_{1-x}Ga_xFeO_3$ materials, it was observed that the average coordination number of Al^{3+} increased as the annealing temperature was increased, while the average coordination of Fe^{3+} decreased. The average coordination number of Ga^{3+} was not found to change significantly based on analysis of the Ga K-edge XANES spectra. However, analysis of the Fe K-edge XANES spectra indicates that slightly more Fe^{3+} is present at the tetrahedral A_1 site in $GaFeO_3$ materials as the annealing temperature was increased, which suggests that the average coordination number of Ga^{3+} does increase slightly with higher annealing temperatures. Overall, these observations indicate that Al^{3+} and Fe^{3+} exchange preferentially with each other and not with Ga^{3+}. The strong 4-coordinate site preference of Ga^{3+} inhibits the ability of Fe^{3+} or Al^{3+} to occupy the tetrahedral A_1 site, explaining the negligible changes in the average coordination number of Ga^{3+} were observed with increasing annealing temperature.

3.5. Conclusion

A series of phase pure $Al_{1-x}Ga_xFeO_3$ materials have been successfully synthesized by the citrate sol-gel and co-precipitation methods. These materials have been studied using XANES to determine changes in the average coordination number of Al^{3+}, Ga^{3+}, and Fe^{3+}. It has been shown in this study that the synthetic method can play an important role in determining cation site occupancies, and that changes in composition have a greater effect than annealing temperature. Overall, it was found that in $Al_{1-x}Ga_xFeO_3$ materials, Al^{3+} and Fe^{3+} prefer to reside in octahedral sites, while Ga^{3+} has a strong preference for the tetrahedral A_1 site. That said, it was also shown that the average coordination number of Al^{3+} (and to a much lesser extent Ga^{3+}) increases as the annealing temperature is increased, while the average coordination number of Fe^{3+} decreases. This indicates that Al^{3+} and Fe^{3+} preferentially exchange sites with each other rather than with Ga^{3+}, which is due to the strong tetrahedral site preference of Ga^{3+}. Furthermore, it was found that materials synthesized via the co-precipitation method showed the greatest variability in the average coordination number of the cations. Materials synthesized via the citrate sol-gel or ceramic methods also showed changes, but to a much smaller degree. The polymeric network formed during the citrate sol-gel method, and the pre-existing oxide network present when materials are synthesized by the ceramic method, is thought to inhibit the mobility of the cations during formation of the material. In comparison, there is no long-range network restricting cation mobility for materials produced via the co-precipitation method, resulting in greater variations in the average coordination number of the metals. This study has demonstrated how changes in composition, annealing temperature, and synthetic method can affect metal site preference during synthesis.

Chapter Four

4. Conclusions and Directions for Future Research

4.1. Summary of Factors Affecting Cation Site Disorder

The work presented in this thesis has examined different factors affecting cation site disorder in a large series of $Al_{1-x}Ga_xFeO_3$ materials. Common structural characterization techniques have often provided inconsistent reports as a result of the complexity of the non-centrosymmetric orthorhombic $GaFeO_3$ crystal structure-type adopted by these materials, as well as the significant cation site disorder observed between the three metal ions. Using the elemental specificity of X-ray absorption near-edge spectroscopy (XANES), changes in the average coordination number of each metal was used to investigate how cation site disorder can be affected as a function of composition, synthetic method, and annealing temperature in $Al_{1-x}Ga_xFeO_3$ materials. Through the use of XANES, these studies are among the first to extensively examine quaternary compositions from $Al_{1-x}Ga_xFeO_3$ materials adopting the $GaFeO_3$ crystal structure-type.

4.1.1. *The Effect of Composition on Cation Site Disorder*

In Chapters Two and Three, changes in the average coordination number of each cation were examined by XANES as Ga^{3+} was substituted for Al^{3+} in a series of ternary and quaternary $Al_{1-x}Ga_xFeO_3$ materials ($0 \leq x \leq 1$), which are isomorphic with the non-centrosymmetric, orthorhombic $GaFeO_3$ crystal structure (*Pna2₁*).[4-6] Contrary to the large variation in site occupancies reported from studies on ternary $Al_{2-x}Fe_xO_3$ and $Ga_{2-x}Fe_xO_3$ compounds

(Figure 1.3., page 5), the quaternary $Al_{1-x}Ga_xFeO_3$ materials presented in this thesis were found to show a number of consistent and systematic changes with composition.

The lattice parameters determined using powder XRD patterns from $Al_{1-x}Ga_xFeO_3$ materials were found to increase linearly as the larger Ga^{3+} cation was substituted for the smaller Al^{3+} cation, in accord with Vegard's law.[115] The Al $L_{2,3}$-, Ga K-, and Fe K-edge XANES spectra collected from more than thirty $Al_{1-x}Ga_xFeO_3$ compounds were found to show consistent changes in cation site disorder between the tetrahedral A_1 site and the three octahedral sites as a function of composition. In the ternary $AlFeO_3$ and $GaFeO_3$ materials, it was found that Al^{3+} and Ga^{3+} occupy both 4- and 6-coordinate environments, consistent with studies showing preferential occupation of the tetrahedral A_1 and octahedral A_2 sites by these cations.[4,5] With increasing Ga^{3+} content in the $Al_{1-x}Ga_xFeO_3$ materials, the average coordination number of Al^{3+} was found to increase as Ga^{3+} preferentially substituted at the tetrahedral A_1 site. In $Al_{1-x}Ga_xFeO_3$ materials where $x \approx 0.50$, the tetrahedral site is effectively saturated with Ga^{3+}, resulting in further substitution of Ga^{3+} for Al^{3+} occurring primarily at the octahedral A_2 site in the structure.

Analysis of the Fe K-edge XANES spectra presented in this thesis have shown that Fe^{3+} preferentially occupies the octahedral sites in $Al_{1-x}Ga_xFeO_3$ system over Al^{3+} or Ga^{3+}. Contrary to reports suggesting Fe^{3+} is not present at the tetrahedral A_1 site, a small amount of 4-coordinate Fe^{3+} was observed in all compositions studied. Additionally, with increasing Ga^{3+} content the amount of 4-coordinate Fe^{3+} was found to decrease slightly. The composition driven changes in cation site disorder observed in the $Al_{1-x}Ga_xFeO_3$ materials were found to be consistent with studies examining the substitution of Al^{3+}, Ga^{3+}, and Fe^{3+} in other metal oxide crystal structures, including among others: rare-earth garnets, brownmillerites, or inverse lithium spinels.[111,119,128,129]

4.1.2. *The Effect of Synthetic Method on Cation Site Disorder*

In Chapter Two, $Al_{1-x}Ga_xFeO_3$ materials were synthesized using a high temperature ceramic method, while in Chapter Three these materials were synthesized using a citrate sol-gel method and a co-precipitation method. Through analysis of XANES spectra from these materials, the synthetic method was found to affect cation site disorder via the nature of the chemical matrix binding the different metal cation precursors. While lattice parameters showed linear trends with composition, this specifically occurred when the materials were synthesized using the same method and annealing temperature. $Al_{1-x}Ga_xFeO_3$ materials synthesized via the ceramic method in Chapter Two were found to have the greatest density (i.e., lowest unit cell volume) and lowest amount of cation site disorder, followed by materials synthesized via the citrate sol-gel technique and co-precipitation technique, respectively.

In $Al_{1-x}Ga_xFeO_3$ materials synthesized via the ceramic method, the anion lattice in the binary metal oxide precursors severely inhibits diffusion of the cations as a result of the high energy input required to break the metal-oxygen bonds.[50] The precursors used to synthesize materials using the citrate sol-gel method were amorphous metal citrates, where the cation is chelated by the citrate anion and bound in an organic polymer network.[53] The weaker metal-citrate interactions and decomposition of the polymer network favour greater ion mobility during synthesis of the final product, and therefore more cation site disorder is observed. In the co-precipitation method, the precursor is an amorphous mixture of cations and counter-anions with no long-range network of chemical bonds.[50,51] As a result, materials made via the co-precipitation method were found to show the greatest amount of cation site disorder between the tetrahedral site and the octahedral sites.

4.1.3. *The Effect of Annealing Temperature on Cation Site Disorder*

Examined in Chapter Three, the effect of annealing temperature during the synthesis of $Al_{1-x}Ga_xFeO_3$ materials was found to be partially dependent on the synthetic method as well as the composition. The ion mobility increases with greater annealing temperatures, leading to a more random distribution of Al^{3+}, Ga^{3+}, and Fe^{3+} across the four cation sites in these materials. This temperature dependent cation site disorder was subsequently trapped when the material is quenched in air from high temperature, resulting in small, but observable differences at the Al $L_{2,3}$-, Ga K-, and Fe K-edge XANES spectra from these materials. With increasing annealing temperature, the average coordination number of Al^{3+} was found to increase while the average coordination number of Fe^{3+} was found to decrease. In contrast, the average coordination number of Ga^{3+} was found to remain relatively unchanged with annealing temperature, further exemplifying how strongly Ga^{3+} prefers to be tetrahedrally coordinated. Together, these observations indicated that with increasing annealing temperature, Al^{3+} and Fe^{3+} preferentially exchange between cation sites with each other in quaternary compositions of $Al_{1-x}Ga_xFeO_3$, rather than with Ga^{3+}. In the ternary $GaFeO_3$ compounds, it was found that increasing annealing temperature resulted in greater tetrahedral Fe^{3+} content.

4.2. Significance and Implications

The studies presented in this thesis on the $Al_{1-x}Ga_xFeO_3$ system have provided new insights into metal oxide chemistry, materials science, and XANES spectroscopy. The difficulty in resolving more than two cations occupying an equivalent crystallographic site in a material often prohibits the study of more compositionally complex materials. Through the collection of XANES spectra at the Al $L_{2,3}$-, Ga K-, and Fe K-edges from these materials, these issues were overcome, showing the sensitivity and utility this technique can offer. The studies on

compositional effects in Chapter Two and Chapter Three are important not only for understanding differences between $AlFeO_3$ and $GaFeO_3$ materials, but may be applicable for a number of other Al^{3+}, Ga^{3+}, and Fe^{3+} substituted metal oxide materials.[111,119,128,129] The examination of synthetic methods and annealing temperature on cation site disorder in $Al_{1-x}Ga_xFeO_3$ materials has helped inform differences in the atomic structure, which are relevant to understanding the varied reports of material properties observed in related ternary compositions. That said, these studies could not determine changes in the cation distribution between the octahedral sites, and further study elucidating these differences would prove invaluable towards developing these materials for future applications.

4.3. Directions for Future Research

A greater understanding of Al^{3+}, Ga^{3+}, and Fe^{3+} site preferences in metal oxides has been gained through the studies in this thesis. That said, there are very few reports of the material properties in quaternary compositions of $Al_{2-x-y}Ga_xFe_yO_3$ materials. While multiple studies have suggested that the magnetic transition temperature in these materials is a function of the Fe^{3+} content in the material (y), this interpretation may be simplistic given that the magnetic transition temperatures reported for $Al_{2-x}Fe_xO_3$ materials are often greater than equivalently substituted $Ga_{2-x}Fe_xO_3$ materials (see Figure 1.4., page 9). The studies in this thesis have shown that cation site disorder can be affected in these materials in multiple ways, and it is reasonable to assume that the magnetic transition temperature is not merely a function of the total Fe^{3+} content in these materials, but also the relative amount of Fe^{3+} present at each of the four cation sites. Thus, one avenue for future studies would be to further elucidate synthetic differences for quaternary compositions of $Al_{2-x-y}Ga_xFe_yO_3$ materials by relating how the magnetic moment and transition temperature are affected by changes in the distribution of Al^{3+}, Ga^{3+}, and Fe^{3+} present at the

different cation sites in the material.

Materials adopting the $GaFeO_3$ crystal structure have been synthesized by at least ten methods, and therefore offers a useful chemical system for self-consistently characterizing how different synthetic methods can affect crystalline metal oxide materials.[3,5,6,15-18,20,39,41-43,45,48,64,73,130-136] This could potentially be achieved through coupling of metal $L_{2,3}$-edge XANES with magnetic circular dichroism.[58,137] In this technique, a magnetic field is applied to the material and separate XANES spectra are collected using left- and right-circularly polarized light.[83,94] XMCD spectra are generated through taking the difference between the normalized left- and right-circularly polarized XANES spectra.[83,94] Since Fe^{3+} present at the (A_1,Fe_1) sites couples antiferromagnetically with Fe^{3+} at the (A_2,Fe_2) sites, the external magnetic field will have a different effect on the X-ray absorption cross-section at these sites.[4-6,56,83,94] Further, the external magnetic field should also affect the X-ray absorption cross-section of the non-magnetic Al^{3+} and Ga^{3+} cations in these materials as a result of the magnetostructural coupling inherent to the $GaFeO_3$ crystal structure.[11,30,63] While there are few reports of XMCD spectra from non-magnetic cations, it is not entirely without precedent and could prove highly informative for understanding how synthetic methods affect material properties through changes in the cation distribution of $Al_{2-x-y}Ga_xFe_yO_3$ materials.[138,139]

Throughout this work, efforts have been made to understand how Al^{3+}, Ga^{3+}, and Fe^{3+} disorder between the octahedral and tetrahedral sites in the relatively unexplored $Al_{1-x}Ga_xFeO_3$ system. This was accomplished by systematically studying the average coordination of the metal cations using XANES, resulting in a better understanding of how cation site disorder can be affected in these materials as a function of composition, synthetic method, and annealing temperature. The areas outlined for further study would provide highly valuable information on

how Fe^{3+} cation site occupancies can be tuned through changes in the composition or method used to synthesize the $Al_{1-x}Ga_xFeO_3$ materials. In addition to potentially defining limits on the variability observed in solid state materials and their properties when synthesized by a given method, these investigations could provide a means for producing superior solid state materials through the rational optimization of synthetic methods.

References

1. West, R.A. Solid State Chemistry and its Applications; John Wiley & Sons; New York, NY, 1990.

2. Atkins, P.; de Paula, J. Materials 2: solids. In Physical Chemistry; 9th Ed. W. H. Freeman and Company: New York, NY, 2010; Ch. 19, pp 695-742.

3. Abrahams, S.C.; Reddy, J.M.; Bernstein, J.L. *J. Chem. Phys.* **1965**, *42*, 3957.

4. Bouree, F.; Baudour, J.L.; Elbadraoui, E.; Musso, J.; Laurent, C.; Rousset, A. *Acta Crystallogr., Sect. B: Struct. Sci* **1996**, *B52*, 217.

5. Arima, T.; Higashiyama, D.; Kaneko, Y.; He, J P.; Goto, T.; Miyasaka, S.; Kimura, T.; Oikawa, K.; Kamiyama, T.; Kumai, R.; Tokura, Y. *Phys. Rev. B: Condens. Matter* **2004**, *70*, 064426.

6. Saha, R.; Shireen, A.; Bera, A.K.; Shirodkar, S.N.; Sundarayya, Y.; Kalarikkal, N.; Yusuf, S.M.; Waghmare, U.V.; Sundaresan, A.; Rao, C.N.R. *J. Solid State Chem.* **2011**, *184*, 494.

7. Saha, R.; Shireen, A.; Shirodkar, S.N.; Waghmare, U.V.; Sundaresan, A.; Rao, C.N.R. *Solid State Commun.* **2012**, *152*, 1964.

8. Roy, A.; Prasad, R.; Auluck, S.; Garg, A. *J. Appl. Phys.* **2012**, *111*, 043915.

9. Stoeffler, D. *J. Phys.: Condens. Matter* **2012**, *24*, 185502.

10. Thomasson, A.; Cherifi, S.; Lefevre, C.; Roulland, F.; Gautier, B.; Albertini, D.; Meny, C.; Viart, N. *J. Appl. Phys.* **2013**, *113*, 214101.

11. Mukherjee, S.; Roy, A.; Auluck, S.; Prasad, R.; Gupta, R.; Garg, A. *Phys. Rev. Lett.* **2013**, *111*, 087601.

12. Bahoosh, S.G.; Wesselinowa, J.M. *J. Appl. Phys.* **2013**, *113*, 063905.

13. Popov, Y.F.; Kadomtseva, A.M.; Vorob'ev, G.P.; Timofeeva, V.A.; Ustinin, D.M.; Zvezdin, A.K.; Tegeranchi, M.M. *J. Exp. Theor. Phys.* **1998**, *87*, 146.

14. Pissas, M.; Stamopoulos, D.; Sanakis, Y.; Simopoulos, A. *J. Phys.: Condens. Matter* **2008**, *20*, 415222.

15. Namai, A.; Sakurai, S.; Nakajima, M.; Suemoto, T.; Matsumoto, K.; Goto, M.; Sasaki, S.; Ohkoshi, S.-I. *J. Am. Chem. Soc.* **2009**, *131*, 1170.

16. Namai, A.; Sakurai, S.; Ohkoshi, S.-I. *J. Appl. Phys.* **2009**, *105*, 07B516.

17. Levine, B.F.; Nowlin, C.H.; Jones, R.V. *Phys. Rev.* **1968**, *174*, 571.

18. Remeika, J.P. *J. Appl. Phys.* **1960**, *106*, 123910.

19. Momma, K.; Izumi, F. *J. Appl. Crystallogr.* **2011**, *44*, 1272.

20. Muan, A. *J. Am. Sci* **1958**, *256*, 413.

21. Hill, N.A. *J. Phys. Chem. B* **2000**, 104, 6694.

22. Kimura, T.; Goto, T.; Shintani, H.; Ishizaka, K.; Arima, T.; Tokura, Y. *Nature* **2003**, *426*, 55.

23. Eerenstein, W.; Mathur, N.D.; Scott, J.F. *Nature* **2006**, *442*, 759.

24. Cheong, S.-W.; Mostovoy, M. *Nat. Mater.* **2007**, *6*, 13.

25. Fiebig, M. *J. Phys. D: Appl. Phys.* **2005**, *38*, R123.

26. Scott, J.F. *Nat. Mater.* **2007**, *6*, 256.

27. Ramesh, R.; Spaldin, N.A. *Nat. Mater.* **2007**, *6*, 21.

28. Roy, A.; Mukherjee, S.; Gupta, R.; Auluck, S.; Prasad, R.; Garg, A. *J. Phys.: Condens. Matter* **2011**, *23*, 325902.

29. Han, M.J.; Ozaki, T.; Yu, J. *Phys. Rev. B: Condens. Matter* **2007**, *75*, 060404.

30. Yoshikiyo, M.; Yamada, K.; Namai, A.; Ohkoshi, S.-I. *J. Phys. Chem. C* **2012**, *116*, 8688.

31. Kim, W.; We, J.H.; Kim, S.J.; Kim, C.S. *J. Appl. Phys.* **2007**, *101*, 09M515.

32. Mukherjee, S.; Ranjan, V.; Gupta, R; Garg, A. *Solid State Commun.* **2012**, *52*, 1181.

33. Kang, K.U.; Kim, S.B.; An, S.Y.; Cheong, S.-W.; Kim, C.S. *J. Magn. Magn. Mater.* **2006**, *272-276*, 555.

34. Sharma, K.; Reddy, V.R.; Kothari, D.; Gupta, A.; Banerjee, A.; Sathe, V.G. *J. Phys.: Condens. Matter* **2010**, *22*, 146005.

35. Mohamed, M.B.; Senyshyn, A.; Ehrenberg, H.; Fuess, H. *J. Alloys Compd.* **2010**, *492*, L20.

36. Szymański, K.; Dobrzyński, L.; Bakr, M.; Satuła, D.; Olszewski, W.; Parzych, G.; Fuess, H. *Phase Transitions* **2010**, *83*, 824.

37. Hatnean, M.; Robert, J.; Diaz, M.T.F.; Ressouche, E.; Cousson, A.; Pinsard-Gaudart, L.; Petit, S. *Eur. Phys. J. Spec. Top.* **2013**, *213*, 69.

38. Sharma, K.; Reddy, V.R.; Gupta, A.; Kaushik, S.D.; Siruguri, V. *J. Phys.: Condens. Matter* **2012**, *24*, 376001.

39. Lefevre, C.; Roulland, F.; Thomasson, A.; Meny, C.; Porcher, F.; André, G.; Viart, N. *J. Phys. Chem. C* **2013**, *117*, 14832.

40. Mishra, S.K.; Mittal, R.; Singh, R.; Zbiri, M.; Hansen, T.; Schober, H. *J. Appl. Phys.* **2013**, *113*, 174102.

41. Sharma, K.; Reddy, V.R.; Gupta, A.; Banerjee, A.; Awasthi, A.M. *J. Phys.: Condens. Matter* **2013**, *25*, 076002.

42. Trassin, M.; Viart, N.; Barre, S.; Pourror, G.; Lee, J.; Jo, W.; Dumesnil, K.; Dufour, C.; Robert, S. *J. Mater. Chem.* **2009**, *19*, 8876.

43. Olliver, B.; Retoux, R.; Lacorre, P.; Massiot, D.; Férey, G. *J. Mater. Chem.* **1997**, *7*, 1049.

44. Ge, S.; Zheng, Z. *Solid State Sci.* **2009**, *11*, 1592.

45. Playford, H.Y.; Hannon, A.C.; Barney, E.R.; Walton, R.I. *Chem. Eur. J.* **2013**, *19*, 2803.

46. Tronc, E.; Chanéac, C.; Jolivet, J.P. *J. Solid State Sci.* **1998**, *139*, 93.

47. Tronc, E.; Chanéac, C.; Jolivet, J.P.; Grenèche, J.M. *J. Appl. Phys.* **2005**, *98*, 053901.

48. Sakurai, S.; Namai, A.; Hashimoto, K.; Ohkoshi, S.-I. *J. Am. Chem. Soc.* **2009**, *131*, 18299.

49. Zayat, M.; Levy, D. *Chem. Mater.* **2000**, *12*, 2763.

50. Gosavi, P.V.; Biniwale, R.B. Mater. *Chem. Phys.* **2010**, *119*, 324.

51. McFarland, E.W.; Metiu, H. *Chem. Rev.* **2013**, *113*, 4391.

52. McCammon, C.A.; Liu, L.-G. *Phys. Chem. Miner.* **1984**, *10*, 106.

53. Cushing, B.L.; Kolesnichenko, V.L.; O'Connor C.J. *Chem. Rev.* **2004**, *104*, 3893.

54. Nowlin, C.H.; Jones, R.V. *J. Appl. Phys.* **1963**, *34*, 1262.

55. Kaneko, Y.; Arima, T.; He, J.P.; Kumai, R.; Tokura, Y. *J. Magn. Magn. Mater.* **2004**, *304*, e769.

56. Kubota, M.; Arima, T.; Kaneko, Y.; He, J.P.; Yu, X.Z.; Tokura, Y. *Phys. Rev. Lett.* **2004**, *92*, 137401.

57. Ogawa, Y.; Kaneko, Y.; He, J.P.; Yu, X.Z.; Arima, T.; Tokura, Y. *Phys. Rev. Lett.* **2004**, *92*, 047401.

58. Kim, J.-Y.; Koo, T.Y.; Park, J.-H. *Phys. Rev. Lett.* **2006**, *96*, 047205.

59. Sun, Z.H.; Cheng, B.L.; Dai, S.; Cao, L.Z.; Zhou, Y.L.; Jin, K.J.; Chen, Z.H.; Yang, G.Z. *J. Phys. D: Appl. Phys.* **2006**, *39*, 2481.

60. We, J.H.; Kim, S.J.; Kim, C.S. *IEEE Trans. Magn.* **2006**, *42*, 2876.

61. Naik, V.B.; Mahendiran, R. *J. Appl. Phys.* **2009**, *106*, 123910.

62. Mohamed, M.B.; Fuess, H. *J. Magn. Magn. Mater.* **2011**, *323*, 2090.

63. Mukherjee, S.; Garg, A.; Gupta, R. *J. Phys.: Condens. Matter* **2011**, *23*, 455403.

64. Bhushan, B.; Mukherjee, S.; Basumallick, A.; Bandopadhyay, S.K.; Das, D. *Hyperfine Interact.* **2008**, *187*, 101.

65. Dayal, R.R.; Gard, J.A.; Glasser, F.P. *Acta. Cryst.* **1965**, *18*, 574.

66. Majzlan, J.; Navrotsky, A.; Evans, B.J. *Phys. Chem. Miner.* **2002**, *29*, 515.

67. Jin, J.; Ohkoshi, S.-I.; Hashimoto, K. *Adv. Mater.* **2004**, *16*, 48.

68. Brázda, P.; Nižňanský, D.; Rehspringer, J.-L.; Vejpravová, J.P. *J. Sol-Gel Sci. Technol.* **2009**, *51*, 78.

69. Vejpravová, J.P.; Prokleska, J.; Vales, V.; Danis, S.; Mantlikova, S.; Holy, V.; Brázda, P.; Doyle, S.; Ritter, C.; Kitazawa, D.; Nižňanský, D. *IOP Conf. Ser.: Mater. Sci. Eng.* **2011**, *18*, 022010.

70. Yamada, K.; Yoshikiyo, M.; Namai, A.; Ohkoshi, S.-I. *Hyperfine Interact.* **2012**, *205*, 117.

71. Mukhopadhyay, K.; Sutradhar, S.; Modak, S.; Roy, S.K.; Chakrabarti, P.K. *J. Phys. Chem. C* **2012**, *116*, 4948.

72. Shireen, A.; Saha, R.; Mandal, P.; Sundaresan, A.; Rao, C.N.R. *J. Mater. Chem.* **2011**, *21*, 57.

73. Dhanasekaran, P.; Gupta, N.M. *Int. J. Hydrogen Energy* **2012**, *37*, 4897.

74. Heiba, Z.K.; Abo-Shama, A.; Bakr, M.; El-Sayed, K. *Powder Diffr.* **2007**, *22*, 256.

75. Mohamed, M.B.; Wang, H.; Fuess, H. *J. Phys. D: Appl. Phys.* **2010**, *43*, 455409.

76. Mohamed, M.B.; Senyshyn, A.; Fuess, H. *Z. Kristallogr. Proc.* **2011**, *1*, 417.

77. Saha, R.; Shireen, A.; Shirodkar, S.N.; Waghmare, U.V.; Sundaresan, A.; Rao, C.N.R. *J. Solid State Chem.* **2011**, *184*, 2353.

78. Mohamed, M.B.; Hinterstein, M.; Fuess, H. *Mater. Lett.* **2012**, *85*, 102.

79. Lefevre, C.; Shin, R.H.; Lee, J.H.; Oh, S.H.; Roulland, F.; Thomasson, A.; Autissier, E.; Meny, C.; Jo, W.; Viart, N. *Appl. Phys. Lett.* **2012**, *100*, 262904.

80. Namai, A.; Yoshikiyo, M.; Yamada, K.; Sakurai, S.; Goto, T.; Yoshida, T.; Miyazaki, T.; Nakajima, M.; Suemoto, T.; Tokoro, H.; Ohkoshi, S.-I. *Nat. Comm.* **2012**, *3*, 1035.

81. Yamada, K.; Tokoro, H.; Yoshikiyo, M.; Yorinaga, T.; Namai, A.; Ohkoshi, S.-I. *J. Appl. Phys.* **2012**, *111*, 07B506.

82. Grunes, L.A.; Leapman, R.D.; Wilker, C.N.; Hoffman, R.; Kunz, A.B. *Phys. Rev. B: Condens. Matter Mater. Phys.* **1982**, *25*, 7157.

83. de Groot, F.M.F. *J. Electron Spectrosc. Relat. Phenom.* **1994**, *67*, 529.

84. Jiang, D.-T. X-Ray Absorption Fine Structure Spectroscopy. In *Synchrotron Radiation: Earth, Environmental and Materials Sciences Applications*; Henderson, G.; Baker, D.R., Eds.; Mineralogical Association of Canada: Ottawa, ON, 2002; pp 65-98.

85. Newville, M., *Fundamentals of XAFS*, Revision 1.7.; University of Chicago: Chicago, IL, 2004.

86. de Groot, F.; Vankó, G.; Glatzel, P. *J. Phys: Condens. Matter* **2009**, *21*, 104207.

87. Sham, T.K. Synchrotron Radiation: An Overview. In *Synchrotron Radiation: Earth, Environmental and Materials Sciences Applications*; Henderson, G.; Baker, D.R., Eds.; Mineralogical Association of Canada: Ottawa, ON, 2002; pp 1-24.

88. Winick, H. *J. Synchrotron Radiat.* **1998**, *5*, 168.

89. Rosendahl, S.M.; Borondics, F.; May, T.E.; Pedersen, T.M.; Burgess, I.J. *Anal. Chem.* **2011**, *83*, 3632.

90. Canadian Light Source. What is a Synchrotron? http://www.lightsource.ca/education/whatis.php (accessed Aug, 2013)

91. MacLennan, A.; Banerjee, A.; Hu, Y.; Miller, J.T.; Scott, R.W.J. *ACS Catal.* **2013**, *3*, 1411.

92. Gillespie, A.W. *Characterizing soil organic nitrogen using advanced molecular analytical techniques*. Ph.D. Thesis, University of Saskatchewan, Saskatoon, SK, August 2010.

93. Gaultois, M.W.; Grosvenor, A.P. *J. Phys. Chem. C* **2010**, *114*, 19822.

94. de Groot, F.; Vogel, J. Fundamentals of X-ray Absorption and Dichroism: The Multiplet Approach. In *Neutron and X-ray Spectroscopy*; Hippert, F.; Geissler, E.; Hodeau, J.L.; Lelièvre-Berna, E.; Regnard, J.-R., Eds.; Springer: Netherlands, 2006; pp 3-66.

95. de Groot, F. *Chem. Rev.* **2001**, *101*, 1779.

96. de Groot, F.M.F. *AIP Conf. Proc.* **2007**, *882*, 37.

97. Yamamoto, T. *X-Ray Spectrom.* **2008**, *37*, 572.

98. Thompson, A., Attwood, D., Gullikson, E., Howells, M., Kim, K.-J., Kirz, J., Kortright, J., Lindau, I., Pianetta, P., Robinson, A., Scofield, J., Underwood, J., Vaughan, D., Williams, G., Winick, H., *X-ray Data Booklet*, 3rd ed.; Lawrence Berkeley National Laboratory: Berkeley, 2009.

99. de Groot, F. *Coord. Chem. Rev.* **2005**, *249*, 31.

100. Gaultois, M.W.; Greedan, J.E.; Grosvenor, A.P. *J. Electron Spectrosc. Relat. Phenom.* **2011**, *184*, 192.

101. Krause, M.O.; Oliver, J.H. *J. Phys. Chem. Ref. Data* **1979**, *8*, 329.

102. Calculated using the Heisenberg Uncertainty Principle and Fe K-edge Core Line Width from reference 101

103. Weigel, C.; Calas, G.; Cormier, L.; Galoisy, L.; Henderson, G.S. *J. Phys.: Condens. Matter* **2008**, *20*, 135219.

104. Nishi, K.; Shimizu, K.-I.; Takamatsu, M.; Yoshida, H.; Satsuma, A.; Tanaka, T.; Yoshida, S.; Hattori, T. *J. Phys. Chem. B* **1998**, *102*, 10190.

105. Westre, T.E.; Kennepohl, P.; DeWitt, J.G.; Hedman, B.; Hodgson, K.O.; Solomon, E.I. *J. Am. Chem. Soc.* **1997**, *119*, 6297.

106. Wilke, M.; Farges, F.; Petit, P.-E.; Brown, G.E.; Martin, F. *Am. Mineral.* **2001**, *86*, 714.

107. Walker, J.D.S. Hard X-ray transmission setup for the HXMA beamline (6ID-1) at the Canadian Light Source. Photo taken November 30, 2011.

108. Ravel, B.; Newville, M. *J. Synchrotron Radiat.* **2005**, *12*, 537.

109. Walker, J.D.S. Ultra-high vacuum X-ray absorption spectroscopy chamber on the VLS-PGM beamline (11ID-2) at the Canadian Light Source. Photo taken July 31, 2013.

110. Hu, Y.F.; Zuin, L.; Reininger, R.; Sham, T.K. *AIP Conf. Proc.* **2007**, *879*, 535.

111. Grosvenor, A.P.; Greedan, J.E. *J. Phys. Chem. C* **2009**, *113*, 11366.

112. Geller, S. *J. Chem. Phys.* **1960**, *33*, 676.

113. Hill, V.G.; Roy, R.; Osborn, E.F. *J. Am. Ceram. Soc.* **1952**, *35*, 135.

114. *X'Pert Highscore Plus Program, Version 3.0e*; PANalytical B.V.: Amelo, The Netherlands, 2012.

115. Denton, A.R.; Ashcroft, N.W. *Phys. Rev. A: At., Mol., Opt. Phys.* **1991**, *43*, 3161.

116. Shannon, R.D. *Acta Crystallogr., Sect. A: Found. Crystallogr.* **1976**, *32*, 751.

117. Heald, S.M.; Brewe, D.L.; Stern, E.A.; Kim, K.H.; Brown, F.C.; Jiang, D.T.; Crozier, E.D.; Gordon, R.A. *J. Synchrotron Radiat.* **1999**, *6*, 347.

118. van Bokhoven, J.A.; Nabi, T.; Sambe, H.; Ramaker, D.E.; Koningsberger, D.C. *J. Phys.: Condens. Matter* **2001**, *13*, 10247.

119. Grosvenor, A.P.; Ramezanipour, F.; Derakhshan, S.; Maunders, C.; Botton, G.A.; Greedan, J.E. *J. Mater. Chem.* **2009**, *19*, 9213.

120. Dunitz, J.D.; Orgel, L.E. *J. Phys. Chem. Solids* **1957**, *3*, 318.

121. Goodenough, J.B.; Loeb, A.L. *Phys. Rev.* **1955**, *98*, 391.

122. Burdett, J.K.; Price, G.D.; Price, S.L. *J. Am. Chem. Soc.* **1982**, *104*, 92.

123. Burdett, J.K. *J. Chem. Soc., Dalton Trans* **1976**, 1725.

124. Pyykkö, P. *Phys. Rev.* **1988**, *88*, 563.

125. Berbenni, V.; Milanese, C.; Bruni, G.; Marini, A. *J. Therm. Anal. Cal.* **2005**, *82*, 401.

126. Miller, A. *J. Appl. Phys.* **1959**, *30*, 24S.

127. Price, G.D.; Price, S.L.; Burdett, J.K. *Phys. Chem. Miner.* **1982**, *8*, 69.

128. Neto, J.M.; Domingues, P.H.; Barthem, V.M.T.S.; de Souza Barros, F. *J. Appl. Phys.* **1984**, *55*, 2338.

129. Stanek, C.R.; Jiang, C.; Yadav, S.K.; McClellan, K.J.; Uberauga, B.P.; Andersson, D.A.; Nikl, M. *Phys. Status Solidi B* **2013**, *250*, 244.

130. Roy, R.; Hill, V.G.; Osborn, E.F. *J. Am. Chem. Soc.* **1952**, *74*, 719.

131. van Hook, H.J. *J. Am. Ceram. Soc.* **1965**, *48*, 470.

132. Ferretti, A.; Shannon, R.D. *Mater. Res. Bull.* **1973**, *8*, 379.

133. Levin, I.; Brandon, D. *J. Am. Ceram. Soc.* **1998**, *81*, 1995.

134. Cótica, L.F.; De Medeiros, S.N.; Santos, I.A.; Paesano Jr., A.; Kinast, E.J.; Da Cunha, J.M.B.; Venet, M.; Garcia, D.; Eiras, J.A. *Ferroelectrics* **2006**, *338*, 241.

135. Saha, R.; Shireen, A.; Shirodkar, S.N.; Singh, M.S.; Waghmare, U.V.; Sundaresan, A.; Rao, C.N.R. *Inorg. Chem.* **2011**, *50*, 9527.

136. Sharma, K.; Reddy, V.R.; Gupta, A.; Choudhary, R.J.; Phase, D.M.; Ganesan, V. *Appl. Phys. Lett.* **2013**, *102*, 212401.

137. Tseng, Y.-C.; Souza-Neto, N.M.; Haskel, D.; Gich, M.; Frontera, C.; Roig, A.; van Veenendaal, M.; Nogués, J. *Phys. Rev. B* **2009**, *79*, 094404.

138. Keavney, D.J.; Cheung, S.H.; King, S.T.; Weinert, M.; Li, L. *Phys. Rev. Lett.* **2005**, *95*, 257201.

139. Okane, T.; Ohkochi, T.; Inami, T.;Takeda, Y.; Fujimori, S.-I.; Kawamura, N.; Suzuki, M.; Tsutsui, S.; Yamagami, H.; Fujimori, A.; Tanaka, A.; Aoki, D.; Homma, Y.; Shiokawa, Y.; Yamamoto, E.; Haga, Y.; Nakamura, A.; Ōnuki, Y. *Phys. Rev. B* **2009**, *80*, 104419.

Appendix 1

A1. Supporting Information for Chapter Two

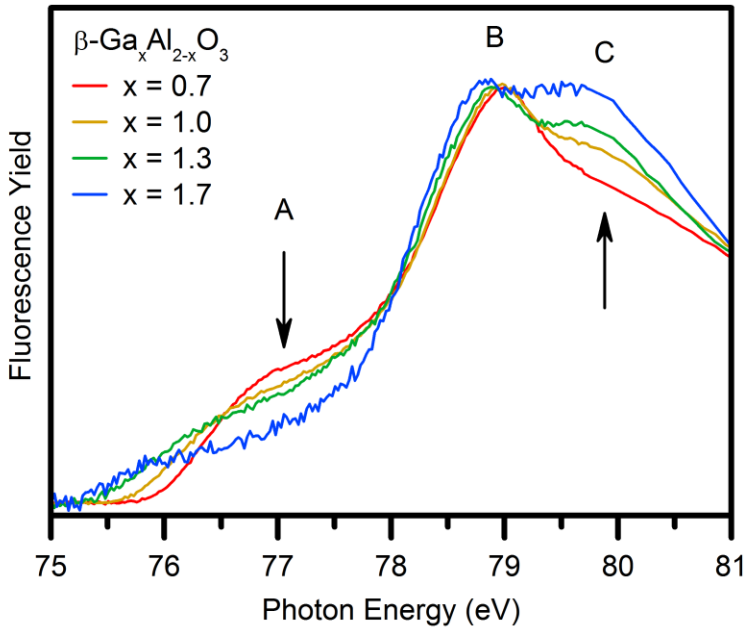

Figure A1.1. Normalized Al $L_{2,3}$-edge XANES spectra from β-$Ga_xAl_{2-x}O_3$ materials, with arrows indicating the change in intensity that occurs as the Ga^{3+} content in the material is increased. The decrease in intensity of feature A (4-coordinate Al^{3+}) indicates that the amount of Al^{3+} present at the tetrahedral site decreases as the Ga^{3+} content in the β-$Ga_xAl_{2-x}O_3$ materials is increased. Unfortunately, the nature of the transitions comprising features B and C is unclear. When taken with the Ga K-edge spectra collected from these materials (Figure 2.3.b, page 34), the Al $L_{2,3}$-edge spectra presented here tentatively support that Al^{3+} prefers occupying octahedral cation sites, while Ga^{3+} prefers occupying tetrahedral cation sites.

Appendix 2

A2. Supporting Information for Chapter Three

Table A2.1. Lattice constants for the $Al_{1-x}Ga_xFeO_3$ materials synthesized at different annealing temperatures via the citrate sol-gel method.

x (Ga^{3+})	Temperature	a (Å)	b (Å)	c (Å)	Volume ($Å^3$)
0.00	1350 °C	4.9845(2)	8.5548(4)	9.2369(4)	393.87(5)
0.25	1200 °C	5.0068(4)	8.6024(7)	9.2742(7)	399.44(9)
0.25	1350 °C	5.0058(1)	8.5982(2)	9.2760(3)	399.25(3)
0.50	1200 °C	5.0216(3)	8.6320(6)	9.3018(6)	403.20(8)
0.50	1350 °C	5.0244(3)	8.6332(7)	9.3095(8)	403.81(9)
0.75	1000 °C	5.0586(3)	8.7041(7)	9.3598(7)	412.12(9)
0.75	1100 °C	5.0564(2)	8.6965(5)	9.3535(5)	411.30(6)
0.75	1200 °C	5.0544(1)	8.6915(3)	9.3504(3)	410.77(4)
0.75	1350 °C	5.0538(1)	8.6908(2)	9.3526(2)	410.78(2)
1.00	1900 °C	5.0831(7)	8.764(1)	9.408(1)	419.1(2)
1.00	1000 °C	5.0765(2)	8.7375(4)	9.3824(4)	416.16(5)
1.00	1350 °C	5.0806(2)	8.7434(5)	9.3907(6)	417.15(7)

Table A2.2. Lattice constants for the $Al_{1-x}Ga_xFeO_3$ materials synthesized at different annealing temperatures via the co-precipitation method.

x (Ga^{3+})	Temperature	a (Å)	b (Å)	c (Å)	Volume ($Å^3$)
0.00	1350 °C	4.9849(2)	8.5540(4)	9.2346(4)	393.77(5)
0.25	1200 °C	5.007(1)	8.607(2)	9.273(2)	399.6(3)
0.25	1350 °C	5.0056(2)	8.5974(5)	9.2746(5)	399.13(6)
0.50	1200 °C	5.0263(6)	8.649(1)	9.312(1)	404.8(1)
0.50	1350 °C	5.0273(2)	8.6395(4)	9.3090(4)	404.32(5)
0.75	1000 °C	5.0531(8)	8.692(2)	9.348(2)	410.6(2)
0.75	1100 °C	5.0523(6)	8.694(1)	9.351(1)	410.7(1)
0.75	1350 °C	5.0533(2)	8.6908(4)	9.3505(4)	410.65(5)
1.00	1000 °C	5.0825(2)	8.7503(3)	9.4008(3)	418.09(4)
1.00	1200 °C	5.0828(1)	8.7510(1)	9.4010(2)	418.15(2)
1.00	1350 °C	5.0833(1)	8.7521(1)	9.4031(1)	418.34(1)

Table A2.3. Octahedral to tetrahedral peak intensity ratios (B:A) found in the Al $L_{2,3}$-edge for the $Al_{1-x}Ga_xFeO_3$ materials synthesized via the citrate sol-gel method.

Temperature	x = 0.00	x = 0.25	x = 0.50	x = 0.75
1000 °C	-	-	-	6.11
1100 °C	-	-	-	6.71
1200 °C	-	2.88	3.37	-
1350 °C	1.79	2.95	3.59	8.64

Table A2.4. Octahedral to tetrahedral peak intensity ratios (B:A) found in the Al $L_{2,3}$-edge for the $Al_{1-x}Ga_xFeO_3$ materials synthesized via the co-precipitation method.

Temperature	x = 0.00	x = 0.25	x = 0.50	x = 0.75
1000 °C	-	-	-	7.36
1100 °C	-	-	-	8.42
1200 °C	-	2.83	4.62	8.90
1350 °C	1.84	2.90	5.07	8.92

Table A2.5. Octahedral to tetrahedral peak intensity ratios (B:A) found in the Al $L_{2,3}$-edge for the $Al_{1-x}Ga_xFeO_3$ materials synthesized via the ceramic method.

Temperature	x = 0.00	x = 0.15	x = 0.35	x = 0.50	x = 0.65	x = 0.85
1350 °C	1.73	2.28	3.05	3.65	4.44	4.89

Table A2.6. Octahedral to tetrahedral peak intensity ratios (B:A) found in the Ga K-edge for the $Al_{1-x}Ga_xFeO_3$ materials synthesized via the citrate sol-gel method.

Temperature	x = 0.25	x = 0.50	x = 0.75	x = 1.00
900 °C	-	-	-	0.95
1000 °C	-	-	0.91	0.96
1100 °C	-	-	0.91	-
1200 °C	0.81	0.87	-	0.95
1350 °C	0.80	0.85	0.91	0.95

Table A2.7. Octahedral to tetrahedral peak intensity ratios (B:A) found in the Ga K-edge for the $Al_{1-x}Ga_xFeO_3$ materials synthesized via the co-precipitation method.

Temperature	x = 0.25	x = 0.50	x = 0.75	x = 1.00
1000 °C	-	-	0.92	0.93
1100 °C	-	-	0.91	-
1200 °C	0.82	0.87	0.92	0.93
1350 °C	0.81	0.87	0.91	0.92

Table A2.8. Octahedral to tetrahedral peak intensity ratios (B:A) found in the Ga K-edge for the $Al_{1-x}Ga_xFeO_3$ materials synthesized via the ceramic method.

Temperature	x = 0.15	x = 0.35	x = 0.50	x = 0.65	x = 0.85	x = 1.00
1350 °C	0.78	0.83	0.86	0.89	0.93	0.96

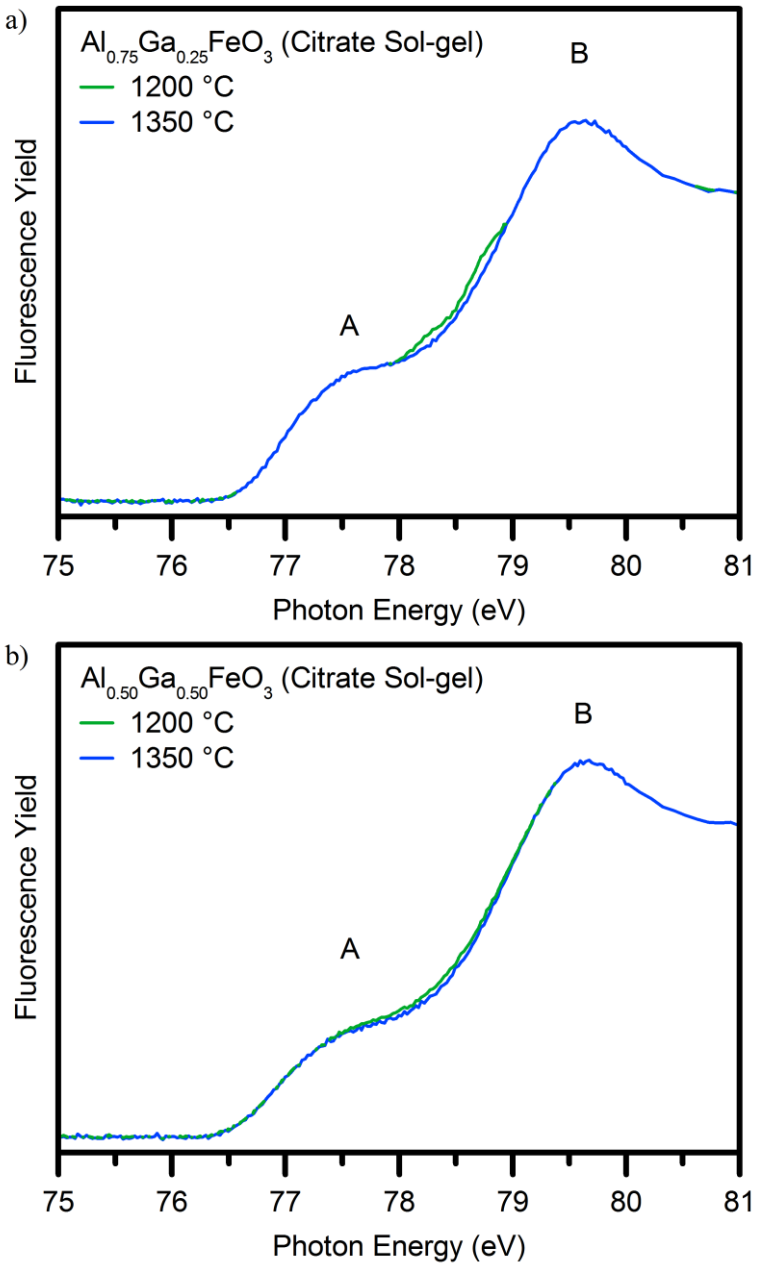

Figure A2.1. Normalized Al $L_{2,3}$-edge spectra from $Al_{1-x}Ga_xFeO_3$ materials, synthesized via the citrate sol-gel method and annealed at different temperatures, are presented for **a)** $Al_{0.75}Ga_{0.25}FeO_3$, and **b)** $Al_{0.50}Ga_{0.50}FeO_3$ materials. Feature A is related to the amount of 4-coordinate Al^{3+}, while feature B is related to the amount of 6-coordinate Al^{3+}.

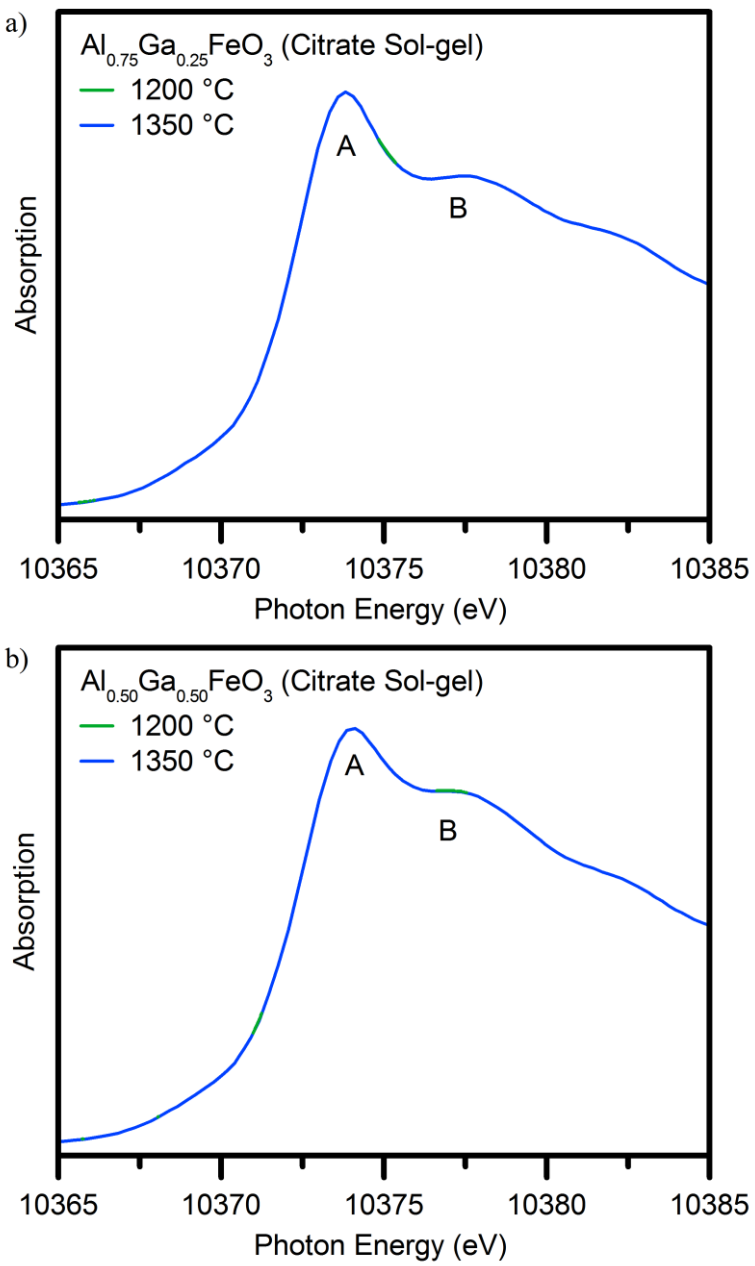

Figure A2.2. Normalized Al $L_{2,3}$-edge spectra from $Al_{1-x}Ga_xFeO_3$ materials, synthesized via the co-precipitation method and annealed at different temperatures, are presented for **a)** $Al_{0.75}Ga_{0.25}FeO_3$ materials, and **b)** $Al_{0.50}Ga_{0.50}FeO_3$ materials. Feature A is related to the amount of 4-coordinate Al^{3+}, while feature B is related to the amount of 6-coordinate Al^{3+}.

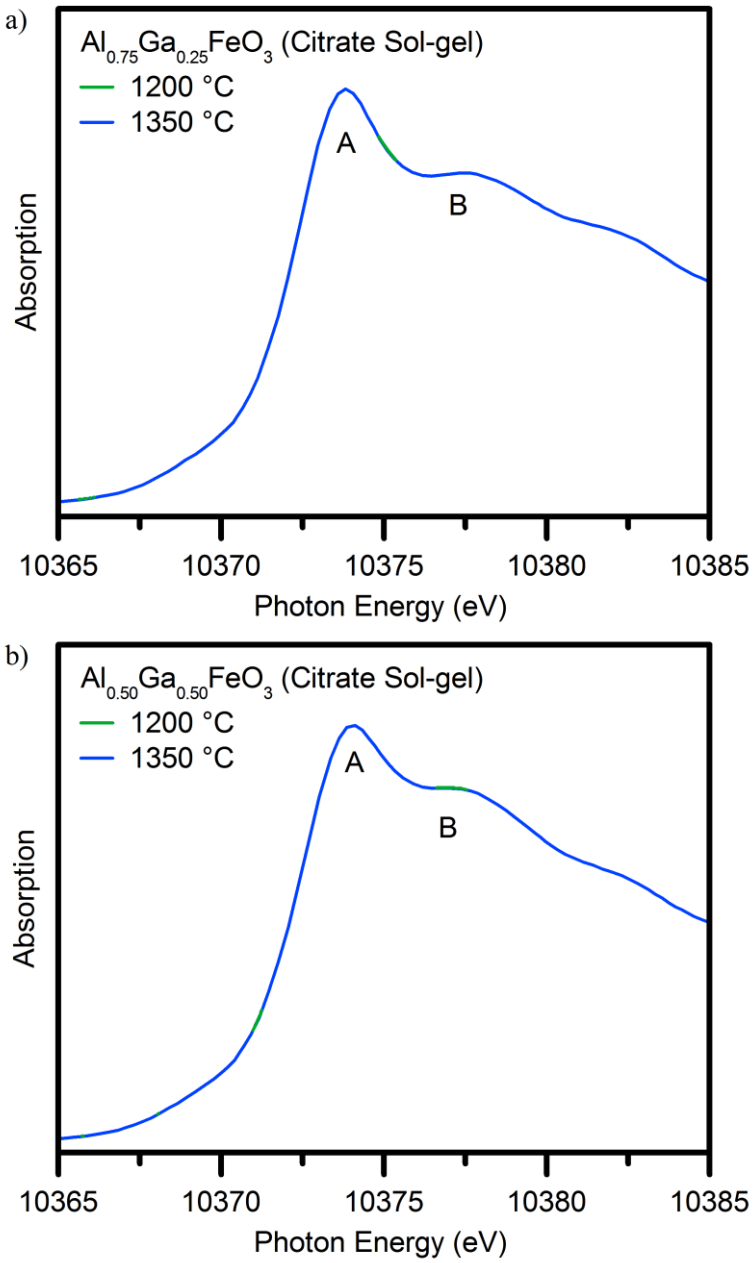

Figure A2.3. Normalized Ga K-edge spectra from $Al_{1-x}Ga_xFeO_3$ materials, synthesized via the citrate sol-gel method and annealed at different temperatures, are presented for **a)** $Al_{0.75}Ga_{0.25}FeO_3$, **b)** $Al_{0.50}Ga_{0.50}FeO_3$, and **c)** $GaFeO_3$ materials (next page). Feature A is related to the amount of 4-coordinate Ga^{3+}, while feature B is related to the amount of 6-coordinate Ga^{3+}.

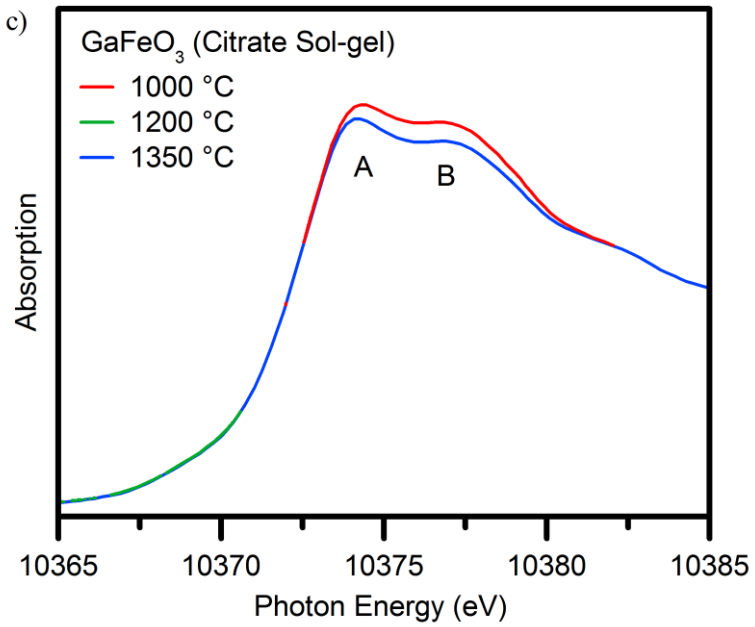

Figure A2.3. Normalized Ga K-edge spectra from $Al_{1-x}Ga_xFeO_3$ materials, synthesized via the citrate sol-gel method and annealed at different temperatures, are presented for **c)** $GaFeO_3$ materials. Feature A is related to the amount of 4-coordinate Ga^{3+}, while feature B is related to the amount of 6-coordinate Ga^{3+}.

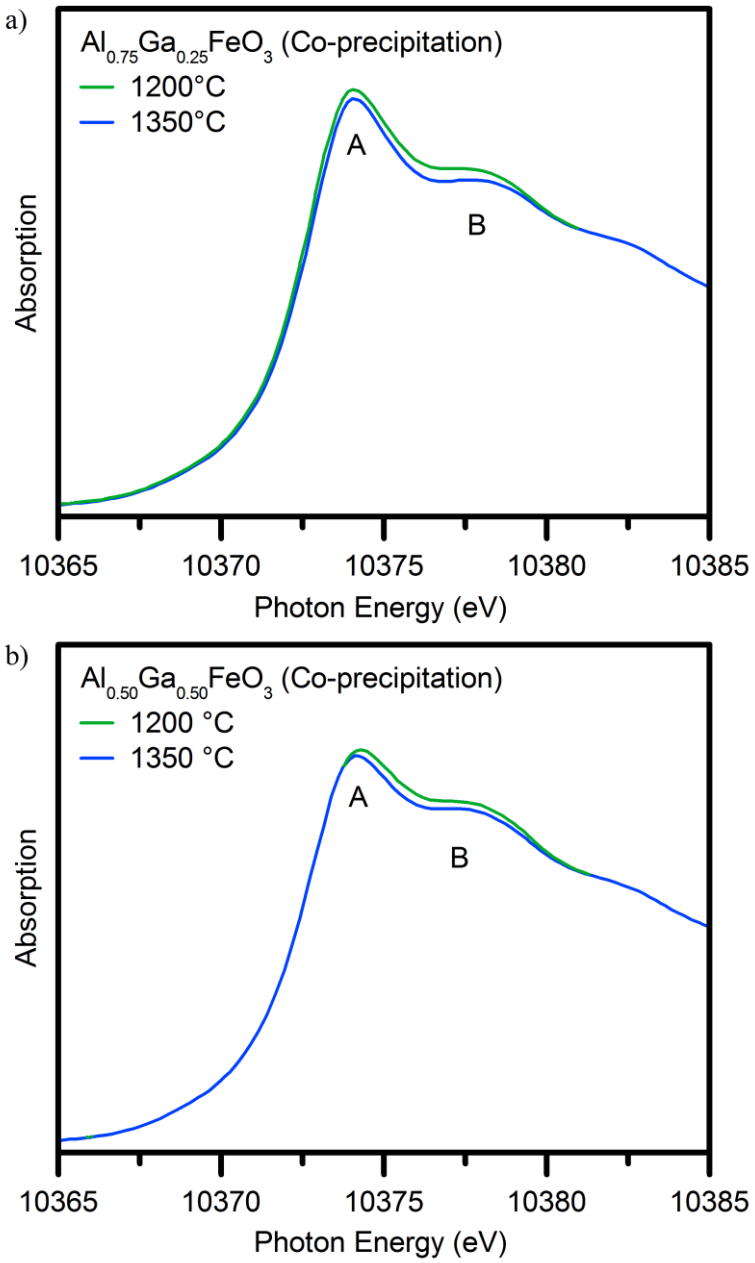

Figure A2.4. Normalized Ga K-edge spectra from $Al_{1-x}Ga_xFeO_3$ materials, synthesized via the co-precipitation method and annealed at different temperatures, are presented for **a)** $Al_{0.75}Ga_{0.25}FeO_3$, **b)** $Al_{0.50}Ga_{0.50}FeO_3$, and **c)** $GaFeO_3$ materials (next page). Feature A is related to the amount of 4-coordinate Ga^{3+}, while feature B is related to the amount of 6-coordinate Ga^{3+}.

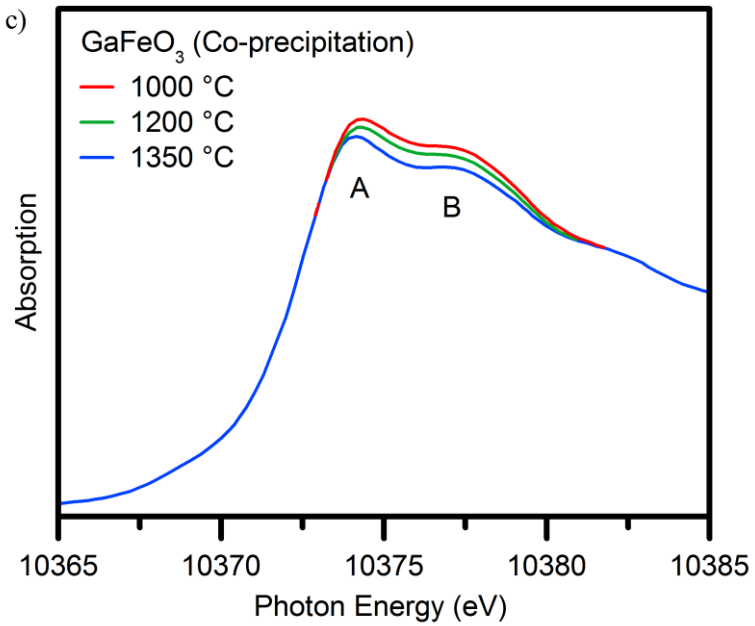

Figure A2.4. Normalized Ga K-edge spectra from $Al_{1-x}Ga_xFeO_3$ materials, synthesized via the co-precipitation method and annealed at different temperatures, are presented for **c)** $GaFeO_3$ materials. Feature A is related to the amount of 4-coordinate Ga^{3+}, while feature B is related to the amount of 6-coordinate Ga^{3+}.

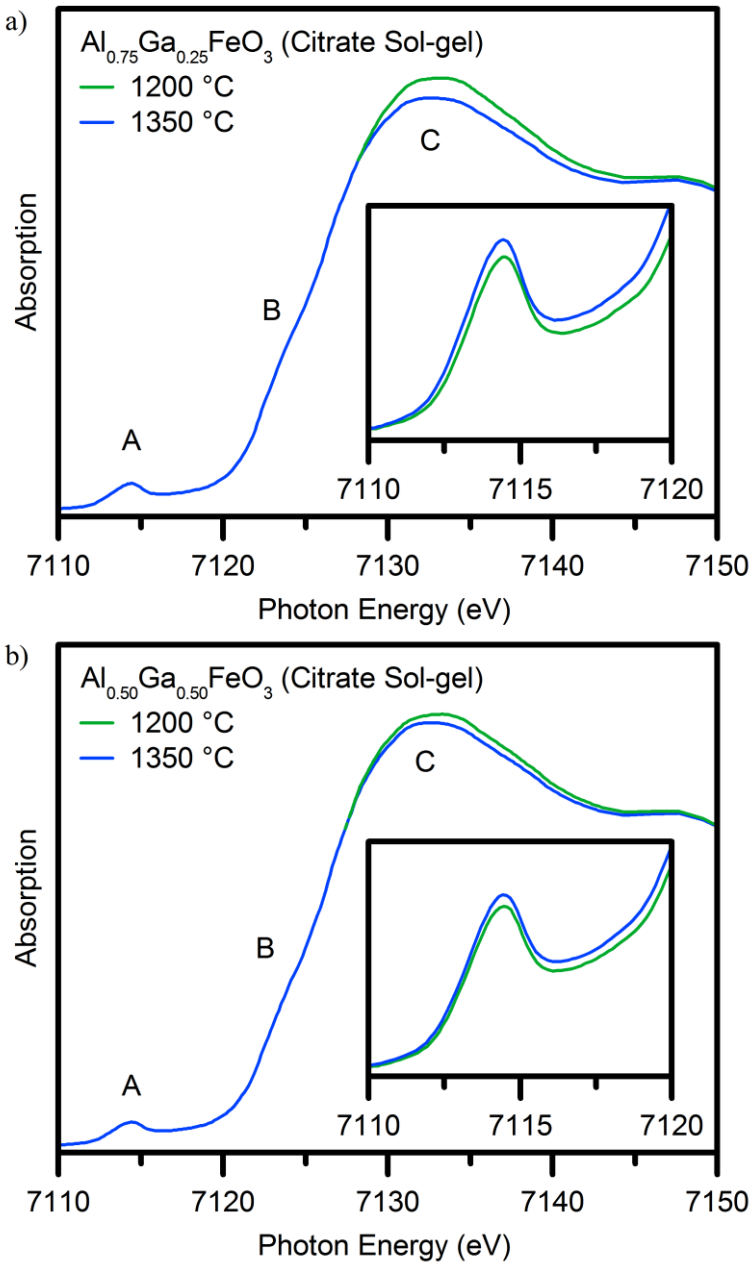

Figure A2.5. Normalized Fe K-edge spectra from $Al_{1-x}Ga_xFeO_3$ materials, synthesized via the citrate sol-gel method and annealed at different temperatures, are presented for **a)** $Al_{0.75}Ga_{0.25}FeO_3$, **b)** $Al_{0.50}Ga_{0.50}FeO_3$, and **c)** $GaFeO_3$ materials (next page). Features A and B are related to the amount of 4-coordinate Fe^{3+}, while feature C is related to the amount of 6-coordinate Fe^{3+}.

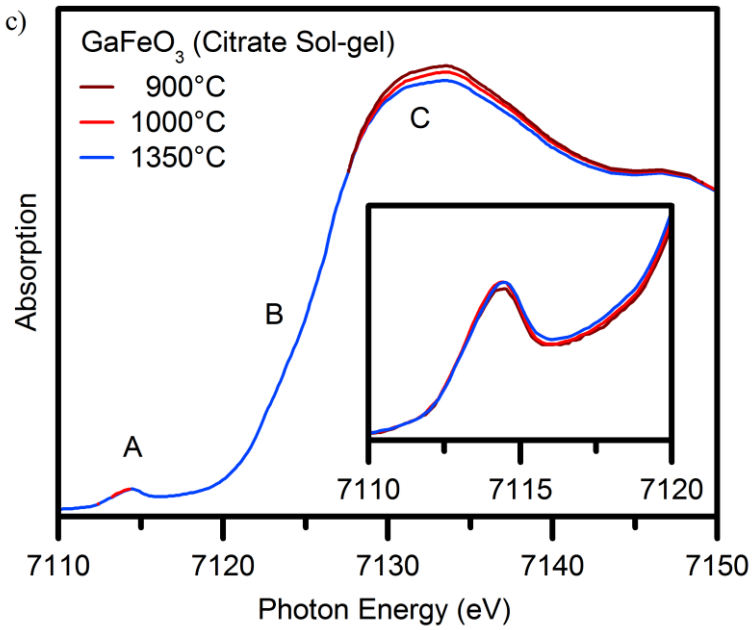

Figure A2.5. Normalized Fe K-edge spectra from $Al_{1-x}Ga_xFeO_3$ materials, synthesized via the citrate sol-gel method and annealed at different temperatures, are presented for **c)** $GaFeO_3$ materials. Features A and B are related to the amount of 4-coordinate Fe^{3+}, while feature C is related to the amount of 6-coordinate Fe^{3+}.

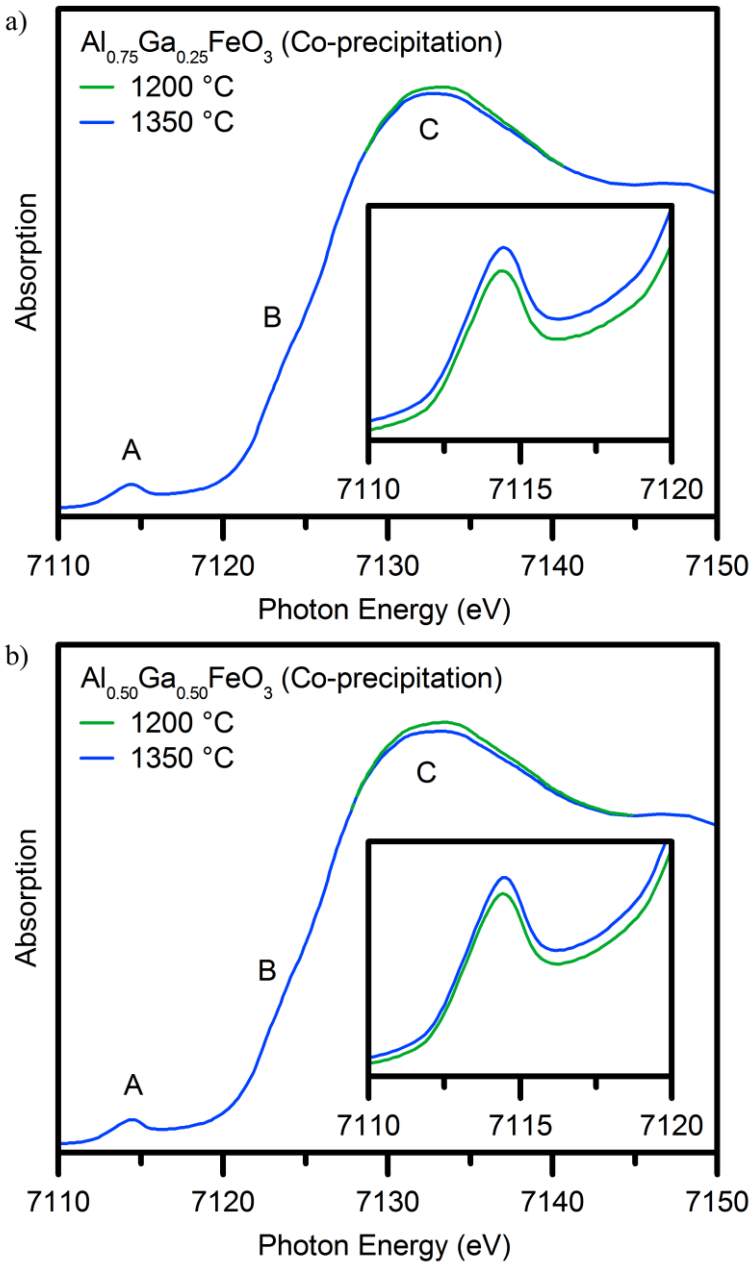

Figure A2.6. Normalized Fe K-edge spectra from $Al_{1-x}Ga_xFeO_3$ materials, synthesized via the co-precipitation method and annealed at different temperatures, are presented for **a)** $Al_{0.75}Ga_{0.25}FeO_3$, **b)** $Al_{0.50}Ga_{0.50}FeO_3$, and **c)** $GaFeO_3$ materials (next page). Features A and B are related to the amount of 4-coordinate Fe^{3+}, while feature C is related to the amount of 6-coordinate Fe^{3+}.

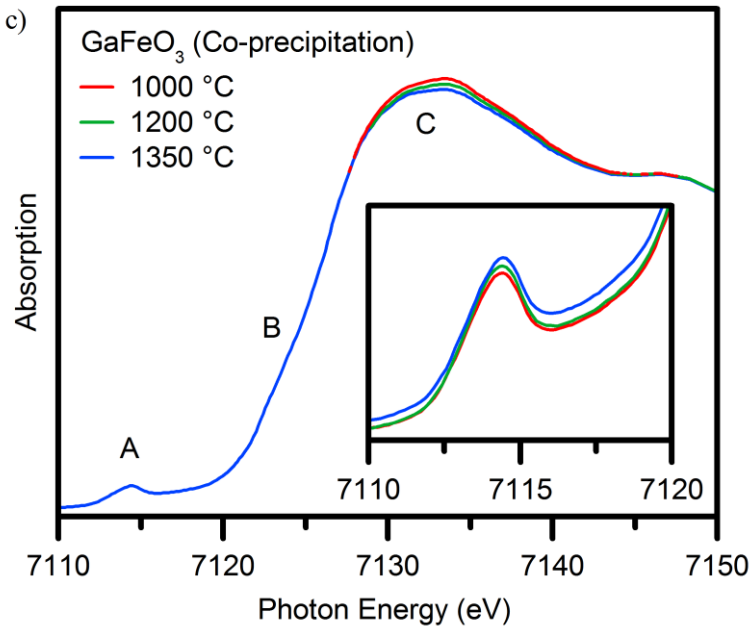

Figure A2.6. Normalized Fe K-edge spectra from $Al_{1-x}Ga_xFeO_3$ materials, synthesized via the co-precipitation method and annealed at different temperatures, are presented for **c)** $GaFeO_3$ materials. Features A and B are related to the amount of 4-coordinate Fe^{3+}, while feature C is related to the amount of 6-coordinate Fe^{3+}.